ABSTRACT

MIGRATION OF AN INTRUDER PARTICLE IN A BOUNDARY DRIVEN SHEAR FLOW

by Jian Liu

This study reports on three-dimensional, discrete element simulations of a single large spherical intruder in a Couette shear flow composed of uniform sized particles. The simulation results are useful in providing a numerical reproduction of the experiments for size segregation and mixing. This in turn has a major importance in many industries which are concerned with handling of particles and powders, such as pharmaceutical manufacturing, agriculture, chemical and mineral processing.

Discrete element simulations are carried out using the "soft sphere" model of Walton, et. al., which provides a method for obtaining the information at a macroscopic level from multi-body collisions within each computational step. A granular shearing flow is induced by allowing the upper and lower bumpy walls to move with the same constant speed in opposite directions. The wall particles are in square arrangements and have the same size as the regular flow particles. The typical transport properties of this flow are characterized by the depth profile of granular temperature, mean velocity and granular pressure which are related to the wall roughness, shear gap height and particle inelasticity measured by a constant normal restitution coefficient. By means of auto-correlation and spectral analysis, the vortex-like structure of velocity field has been revealed, which coincides with the results from the wavelet analysis.

In the micro-gravity study case, an "intruder" with different size ratio has been added in the uniform shear flow described above. It has been observed to migrate away

from the walls and finally become trapped in the central area with a small fluctuation around the equilibrium location. The amplitude of the fluctuation has a relation with the intruder size ratio. Computations indicated that the intruder's motion is induced by the depth distribution of granular pressure which is higher near the moving boundary and lower in the center of the gap. The differences of the normal pressure on the depth profile could be represented by the fluctuation of net force on both sides of the intruder. Also, the circulation pattern in the velocity field may enhance this trend.

Simulations of the annular shear cell device shows us that the motion of the "intruder" is very sensitive to gravity. Similar to the experimental studies, the "intruder" will eventually migrate to the top of the shear flow with a velocity proportional to the size ratio. A further investigation also revealed that the migration of the "intruder" may have a relation with the pattern of the velocity field in the cross-section of the shear direction.

MIGRATION OF AN INTRUDER PARTICLE IN A BOUNDARY DRIVEN SHEAR FLOW

by

Jian Liu

A Dissertation
Submitted to the Faculty of
New Jersey Institute of Technology
in Partial Fulfillment of the Requirements for the Degree of
Doctor of Philosophy in Mechanical Engineering

Department of Mechanical Engineering

January 2004

APPROVAL PAGE

MIGRATION OF AN INTRUDER PARTICLE IN A BOUNDARY DRIVEN SHEAR FLOW

Jian Liu

Dr. Anthony Rosato, Dissertation Advisor — Date
Professor of Mechanical Engineering, NJIT

Dr. Nadine Aubry, Committee Member — Date
Chairman and Professor of Mechanical Engineering, NJIT

Dr. Rong-Yaw Chen, Committee Member — Date
Professor of Mechanical Engineering, NJIT

Dr. Denis Blackmore, Committee Member — Date
Professor of Mathematics, NJIT

Dr. Pushpendra Singh, Committee Member — Date
Associate Professor of Mechanical Engineering, NJIT

BIOGRAPHICAL SKETCH

Author: Jian Liu

Degree: Doctor of Philosophy

Date: August 2003

Undergraduate and Graduate Education:

- Doctor of Philosophy in Mechanical Engineering,
  New Jersey Institute of Technology, Newark, NJ, 2003

- Bachelor of Engineering in Mechanical Engineering,
  Beijing Polytechnic University, Beijing, P. R. China,
  1993

Major: Mechanical Engineering

Presentations and Publications

A. Rosato, J. Liu, " Numerical simulation of size segregation in granular shear flow", 14th US National Congress of Theoretical and Applied Mechanics, Blacksburg, VA, 2002.

A. Rosato, J. Liu, "Migration of an Intruder Particle in a Boundary Driven Shear Flow" 39th Annual Technical Meeting of the Society of Engineering Science, State College, PA, 2002.

A. Rosato, J. Liu, "The Dynamic Behavior of An Intruder Particle in Granular Couette Flow", Proceedings of 2002 Material Research Society Fall Meeting, Boston, MA, pp. 217-223, October 2002.

This dissertation is dedicated to my wife, Wenqi and my parents.

ACKNOWLEDGMENT

I wish to express my sincere appreciation to my advisor, Dr. Anthony Rosato, for his remarkable guidance, constant supervision, friendship and moral support throughout this research. Without his guidance, it would have been impossible for me to finish this program so smoothly. Special thanks are given to Dr. Nadine Aubry, Dr. Rong-Yaw Chen, Dr. Denis Blackmore, Dr. Pushpendra Singh for their active participation in my dissertation committee. I'm also thankful to Dr. Stuart Savage at McGill University and Dr. Michel Louge at Cornell University for their valuable suggestions and kind assistance during these years.

I acknowledge the financial support from the Department of Mechanical Engineering, New Jersey Institute of Technology. I appreciate the friendship and cooperation of Dr. Ninghua Zhang, Chris Ashman, and all of my research group colleagues during this study.

I would like to express my endless gratitude to my parents, Youhui Liu and Jinghua Ni, who have always supported my academic pursuit and helped me in every possible way. I also would like to give the thanks to my sisters for their selfless dedication and generous support. Last, I want to thank my wife, Wenqi Yin, for her love and encouragement throughout these years.

TABLE OF CONTENTS

Chapter		Page
1	INTRODUCTION	1
	1.1 Overview	1
	1.2 Literature Survey	3
	1.2.1 Shear Granular Flow	3
	1.2.2 Size Segregation Experiments	5
	1.2.3 Size Segregation Theory Analysis	12
	1.2.4 Simulation Studies of Segregation	13
	1.2.5 Motivation, Objectives and Methods	17
	1.3 Outline of Thesis	20
2	3-D DISCRETE ELEMENT METHOD SIMULATION MODEL	22
	2.1 DEM Algorithm Application	24
	2.2 Contact Searching and Neighborhood List	29
	2.3 Computational Force Model	30
	2.4 Data Output	34
3	DATA ANALYSIS METHODS	37
	3.1 FFT Spectrum and Auto-correlation	37
	3.2 Mean Square Displacement and Diffusion Coefficient	39
	3.3 Wavelet Analysis	40
4	GENERAL FEATURES OF GRANULAR SHEAR FLOW	48
	4.1 Simulation Cell Description	48
	4.2 General Features of Granular Couette Flow	51

TABLE OF CONTENTS
(Continued)

Chapter		Page
	4.3 Velocity Pattern on XY Plane	58
	4.4 Wavelet Analysis for Velocity Field	66
5	MOTION ANALYSIS OF THE INTRUDER PARTICLE	72
	5.1 General Motion Pattern of the Intruder	73
	5.2 Mean Square Displacement and Diffusion Coefficient	81
	5.3 Net Force and Velocity	82
	5.4 Size Ratio and Mass Ratio	88
	5.5 Contact Number Analysis	89
6	MOTION OF INTRUDER IN GRAVITY FIELD	95
	6.1 Brief Description of the Simulation System with Gravity	95
	6.2 Migration of the Intruder Particle	98
	6.3 Vortex Pattern on Velocity Field	101
7	SUMMARY AND CONCLUSIONS	103
	7.1 Research Summary	103
	7.2 Suggested Future Research Topics	105
APPENDIX A—POST PROCESSING CODE IN MATLAB		106
	A.1 Histogram	106
	A.2 Autocorrelation and FFT Analysis	109
	A.3 Velocity Field in Depth Direction	113
	A.4 Wavelet Analysis	115

A.5 2D Mean Packing Density 116

A.6 Mean Velocity Profile 119

A.7 2D Plot of the Intruder Particle 121

A.8 3D Animation of the Intruder Particle 122

A.9 Contact Angle and Force 123

APPENDIX B—ZONING INDEX SEARCH METHOD 130

REFERENCES 131

LIST OF TABLES

Table **Page**

4.1 Key Parameters for the Material and Simulation Configurations 49

4.2 The Possible Closest Distance Between Intruder and Boundary Plane 50

6.1 Relation Between Rotation Frequency, Linear Velocity, and Shear Rate..... 100

LIST OF FIGURES

Figure		Page
1.1	Diagram of the annular shear cell device	8
1.2	(a) Initial status at t=0s	19
1.2	(b) Segregation at t=20s	19
1.2	(c) Packing fraction profile at t=0s	19
1.2	(d) Packing fraction profile at t=20s	19
2.1	Flow chart of simulation algorithm	25
2.2	Linear normal force loading and unloading with stiffness K_1 and K_2	31
3.1	Schematic diagram for discrete wavelet transform	45
3.2	Diagram of wavelet decomposition tree	46
4.1	Simulation cell for Couette flow with moving bumpy boundaries	48
4.2	Diagram for the smallest distance between intruder and boundary plane	50
4.3	Evolution of normalized long term average velocity V_x	52
4.4	Evolution of normalized short term average of velocity V_x	52
4.5	(a) Mean velocity profile for simulation cell with a gap height H=16d	53
4.5	(b) Mean velocity profile for simulation cell with a gap height H=8d	53
4.6	(a) Granular temperature profile for H=16d	53
4.6	(b) Granular temperature profile for H=8d	53
4.7	(a) Solids packing fraction profile for H=16d	55
4.7	(b) Solids packing fraction profile for H=8d	55
4.8	Normalized granular pressure profile for P_{py} & P_{ky}	56
4.9	Total normal pressure with the inset shown the trend close to the wall	57

LIST OF FIGURES
(Continued)

Figure **Page**

4.10 Color –vector map of the velocity field on XY plane for 8*d* x 8*d* cell 58

4.11 Color-vector map of the velocity field on XY plane for 16*d* x 8*d* cell..... 59

4.12 Diagram of sub-cell to compute the average V_y 60

4.13 (a) $V_y(x)/U$ for H=8*d* cell with boundary velocity *U*=8 R/s..... 61

4.13 (b) Autocorrelation function of $V_y(x)/U$ with boundary velocity *U*=8 R/s 61

4.13 (c) FFT spectrum analysis of the autocorrelation for *U*=8 R/s..... 62

4.14 (a) $V_y(x)/U$ for H=8*d* cell with boundary velocity *U*=16 R/s..... 62

4.14 (b) Autocorrelation function of $V_y(x)/U$ with boundary velocity *U*=16 R/s .. 63

4.14 (c) FFT spectrum analysis of the autocorrelation function for *U*=16 R/s..... 63

4.15 (a) $V_y(x)/U$ for H=8*d* cell with boundary velocity *U*=32 R/s..... 64

4.15 (b) Autocorrelation function of $V_y(x)/U$ with boundary velocity *U*=32 R/s .. 64

4.15 (c) FFT spectrum analysis of the autocorrelation function for *U*=32 R/s..... 65

4.16 Wavelength of velocity pattern under different shear rate with *H*=8*d* 65

4.17 (a) Continuous wavelet analysis for $V_y(x)$ with *U*= 8R/s, *H*=8*d*..... 67

4.17 (b) Continuous wavelet analysis for $V_y(x)$ with *U*= 16R/s, *H*=8*d*..... 67

4.17 (c) Continuous wavelet analysis for $V_y(x)$ with *U*= 32R/s, *H*=8*d*..... 67

4.18 (a) Diagram of decomposition tree of $V_y(x)$ with *U*= 8R/s 70

4.18 (b) Diagram of decomposition tree of $V_y(x)$ with *U*= 16R/s 71

4.18 (c) Diagram of decomposition tree of $V_y(x)$ with *U*= 32R/s 71

5.1 (a) Y(t) for big intruder with size ratio ϕ=1.0..... 72

LIST OF FIGURES
(Continued)

Figure		Page
5.1	(b) Y(t) for big intruder with size ratio ϕ=2.0	73
5.2	Critical time T_c versus ϕ for boundary velocity U=16, 32, 64 R/s	74
5.3	(a) Y(t)/H of intruder with ϕ=1.0 in 2000s	75
5.3	(b) Hist(Y) of intruder with ϕ=1.0 in 2000s	75
5.3	(c) Log plot of FFT spectrum analysis of Y(t) for the intruder (ϕ = 1)	76
5.4	(a) Y(t)/H of intruder with ϕ=2.0 in 2000s	77
5.4	(b) Hist(Y) of intruder with ϕ=2.0 in 2000s	77
5.4	(c) Log plot of FFT spectrum analysis of Y(t) for the intruder (ϕ = 2.0)	77
5.5	(a) Y(t)/H of intruder with ϕ=3.0 in 2000s	77
5.5	(b) Hist(Y) of intruder with ϕ=3.0 in 2000s	77
5.5	(c) Log plot of FFT spectrum analysis of Y(t) for the intruder (ϕ = 3.0)	78
5.6	Trajectory trace of the intruder with size ratio ϕ=2.0 in the shear flow	80
5.7	MSD of each species with different size ratio	81
5.8	Diffusion coefficient of each species for different shear rates	82
5.9	Diagram of the net force around the intruder	84
5.10	(a) Velocity trace for intruder with size ratio ϕ=1.0	84
5.10	(b) Velocity for intruder with size ratio ϕ=2.0	84
5.10	(c) Net force history on an intruder with size ratio ϕ=1.0	85
5.10	(d) Net force history on an intruder with size ratio ϕ=2.0	85
5.11	(a) Net force (F_y) on a tracer particle (ϕ=1.0)	86

LIST OF FIGURES
(Continued)

Figure **Page**

5.11 (b) Velocity history for a tracer particle (ϕ=1.0) 86

5.11 (c) Net force (F_y) on a tracer intruder (ϕ=3.0) 87

5.11 (d) Velocity history for a tracer particle (ϕ=3.0) 87

5.12 (a) Effect of size ratio on RMS of F_y 88

5.12 (b) Effect of size ratio on $V_{y\text{-RMS}}$ 88

5.13 (a) V_{yrms} with different size ratio 89

5.13 (b) V_{yrms} versus mass ratio ϕ_m 89

5.14 Diagram of collision angle (θ) on XY plane 90

5.15 (a) Collision angle distribution function for intruder with ϕ=3.0 91

5.15 (b) Collision angle distribution function for intruder with ϕ=1.0 93

5.16 (a) Depth profile of contact number T_{low} and T_{up} for a tracer particle (ϕ=1.0) 94

5.16 (b) Depth profile of *dn* along the gap height for intruder with ϕ=1.0 94

6.1 Diagram of simulation cell in gravitational field 96

6.2 (a) Initial distribution of the binary mixture with 10 larger intruders 97

6.2 (b) Snapshot taken at t = 20s showing a layer of large particles (ϕ = 2) on the flow surface 98

6.3 Trajectory of the intruder in the YZ plane 99

6.4 Evolution of normalized position Z/H at f = 1.6 and 2.5 100

6.5 Average vertical speed V_z of the intruder (ϕ=2.0) versus shear rate U/D 101

6.6 Secondary flow pattern on the velocity field of YZ plane (U/D = 1/s) 102

LIST OF SYMBOLS

Symbols	Meaning
D	diameter of flow particle
E	Young's modulus
e	coefficient of restitution
g	gravity
H	shear gap height
K_1	normal loading spring constant
K_2	normal unloading spring constant
K_H	spring constant for Hertzian model
K_r, K_T	tangential spring constant
m	mass of each flow particle
N	magnitude of the normal force
n	step number for each contact
P	pressure
P_k	kinetic component of granular pressure
P_p	potential component of granular pressure
R	radius of flow particle
V_s	relative velocity before collision
V_a	relative velocity after collision
Δt	time step for calculation
T	magnitude of the tangential force

LIST OF SYMBOLS
(Continued)

Symbols	Meaning
$\overline{T}$	granular temperature
U	boundary velocity
u'	velocity component in x direction
v'	velocity component in y direction
w'	velocity component in z direction

Greek

α	contact penetration
μ	friction factor
τ	normal contact duration
ν	Poisson's ratio or average solid packing fraction
ρ	density of material
ϕ	particle size ratio
ϕ_m	mass ratio

CHAPTER 1

INTRODUCTION

1.1 Overview

One of the most interesting and intriguing features of granular flows is segregation, which can be described as the evolution of a well-mixed bulk solid to a spatially non-uniform state. This study focused on understanding the mechanism of size segregation in the granular shear flow composed of inelastic spheres using numerical simulation. The Discrete Element Method, which is an outgrowth of molecular dynamics simulations, is used to investigate the macroscopic information and transport properties of a granular Couette flow.

The current research is motivated by problems in the solids processing industries, in which segregation poses a tremendous impediment to the general requirement of creating and maintaining homogeneous mixtures. An inability to achieve and maintain a well-mixed condition of a bulk solid throughout its processing history can lead to serious flaws in the properties of an end product, leading to unfavorable economic consequences. Because solids handling equipment often includes moving walls to promote or induce flows, it is critical to understand how the shearing action of boundaries affects the dynamics of particles with varying properties.

The current study focuses on a model system consisting of a single large intruder in a flow of uniform spheres that are driven by parallel, moving walls. It has been remarked that boundary driven granular flows differ considerably from ordinary fluids in that the pressure depends on the square of the shear rate [1]. This interesting feature has

led to numerous experimental [2-7], theoretical [5, 8-10] and numerical studies [11-14] on mono-disperse systems in the literature.

Numerical simulation has the ability to provide insights into a number of practical problems related to the treatment of granular material in several industries. The urgency of industry's needs and increasingly rapid development of numerical simulation techniques provide a wide spectrum of simulation software products suitable for exploring the behavior of granular materials. On the other hand, numerical simulation also offered the possibility to investigate some transport properties which are not accessible in experiments. In the context of numerical simulation, "hard sphere" and "soft sphere" models are the two general approaches that are used in Discrete Element simulation studies. The "hard sphere" which is the so called "Event-Driven" model, does not allow interpenetration or deformation during impact. Hence it is restricted to flows in which enduring contacts are not predominant. Soft sphere models do not have this restriction since a finite contact time is an inherent feature. In this work, a soft sphere modified uniform shear code developed by Walton and Braun [15, 16]. Modifications to the original code [14] were implemented to incorporate moving upper and lower bumpy boundaries that would drive the shear flow. Diagnostics quantities (i.e., velocity, granular pressure, collision frequency and net force on a tracer particle) were computed by partitioning the spatial region into layers or strips parallel to the direction of shearing. All modifications and changes were validated by comparing numerical simulation results with existing simulation and experimental data. This included verification of the known depth profiles of the mean velocity field, granular temperature and normal stress along the gap height.

1.2 Literature Survey

A better understanding of the governing mechanism of basic shear flow is of critical importance to a wide variety of industrial, and scientific applications. Shear flows of granular materials commonly occur in industrial processes involving transport of bulk solids such as metals, powders, ceramics and gravel; they also can be observed in geophysical events such as powder snow avalanches, rock slides and debris flow.

1.2.1 Sheared Granular Flows

Bagnold [1] carried out innovative experiments that allowed him to separate the motion of granular flows into three major regimes that he termed the "macroviscous", "transitional" and "grain inertia". In the macroviscous" regime, flow behavior is determined by both the viscous effects of the interstitial fluid. The typical feature of this regime is that shear and normal stresses are linearly proportional to the shear rate. At the other limit--"grain inertia regime", stresses or pressure are dictated by particle collisions so that the interstitial fluid plays a minor role. In this regime, the relation of the stress to shear rate is changed from a linear dependence to a square one. The 'transitional regime" is the transitional state between these two limits. The current study will focus on the grain inertia regime which has a high solids packing fraction and relatively lower shear gradients.

In order to model velocity fluctuations, Ogawa [17] introduced the "granular temperature", which is the representation of mean kinetic energy associated with particle velocity fluctuations. He proposed a balance law for this term by only considering the inelastic and frictional interaction between particles while neglecting the rotational part. Although several assumptions were needed to model the particle-particle collisions while

averaging the data, his work reduced led to a simple way to quantify the velocity fluctuation.

Savage and Jeffrey [18] extended the study of Bagnold [1] by considering identical particles subjected to a rapid mean shear. They assumed that the particles were smooth, hard, elastic spheres and expressed the stress as an integral containing probability distribution functions for the velocities of the particles. From their theory, the relative velocity between colliding particles was allowed to be random. The importance of the mean deformation was reflected in the anisotropy of the distribution function, which was proposed to govern the probability of collisions between pairs of flow particles. They calculated the components of the mean stress that result from the exchange of momentum in collisions for perfectly elastic particles.

Jenkins and Savage [8] further improved the understanding of shear granular flow provided in the theory of Savage and Jeffrey [18] by focusing on an idealized granular material comprised of identical, smooth and nearly elastic spheres. They derived integral expressions for the stress, energy flux and rate of dissipation due to collisions of particles using the Maxwellian distribution functions for the velocity of a single particle and for binary collisions.

Shen and Ackermann [19] also derived constitutive equations for a granular flow of identical and frictional disks. They obtained stresses as the average rate of momentum transfer across a surface due to the inter-particle collisions, assuming that binary collisions would be the major mechanism for momentum transfer.

Lun et al. [20] developed the kinetic theory for a granular flow of uniform, smooth and inelastic spherical particles by considering instantaneous binary collisions

between particles. Their results demonstrated that the shear and normal stresses increase monotonically with increasing solids packing fraction when the contribution from particle collisions becomes dominant.

Experiments using annular shear cells [2, 4] have also provided valuable information about the effects on stresses due to shear rates, boundary conditions, material properties, and solids concentrations. However, problems with measuring depth profiles of transport properties related to velocity fluctuations (such as granular temperature and pressure) have hindered progress in understanding the intricacies of these flows.

1.2.2 Size Segregation Experiments

Studies of segregation under a variety of flow situations other than shearing have appeared throughout the literature on granular systems. When an assembly of uniform particles is vibrated, a larger "intruder" particle placed at the bottom of a container will tend to rise to the top surface of the bed. In 1963, Williams [21] carried out some interesting experiments on this phenomenon. He stated that particle size is the principle factor in the segregation, although density and shape may play a secondary role. In order to decipher the causes of segregation under vibration, he repeated the vibration experiment with a single large particle initially placed at the bottom of a bed of glass beads [22] He attributed the sphere's rising motion to the "locking" effect of the overburden pressure that it exerts on the column of materials directly beneath it, thereby preventing the large intruder from moving down. If this particle does experience an upward movement during the vibration, smaller ones could easily move beneath it and become locked.

Ahmad and Smalley [23] carried out the same type of experiments as Williams. They measured the time for the large particle to rise to the surface of a sand-filled vibrated bed. An acceleration range of 1-10g and frequency range of 50-150 Hz was used. It was observed that acceleration was an important factor affecting the segregation. Segregation increases with an increase in acceleration for all fixed frequencies, but it was reduced with increasing frequency at a constant acceleration. It was also confirmed that the higher the bed depth, the longer the segregation time, while the bigger the size of the large ball, the greater the tendency to segregate.

With a radioactive tracer, Harwood [24] measured the segregation effect in the real powder systems. The powder materials were selected to be of different cohesion, different size and density. The powder properties as well as vibratory parameters had profound effects on the results. Significantly increased segregation was observed when the powder was fluidized under sufficient energy.

Recently, Shinbrot [25] repeated the "Brazil-nut" experiment [42, 43] with large grains of different densities. It was observed that in deep beds under high amplitude vibrations, the large heavy grains rose to the surface of the bed, but the larger light grains appeared to sink to the bottom of the bed. In another experiment performed by Brew [26], a transition from the Brazil-nut effect to its reverse form was implemented with a given mass density ratio and excitation intensity. Hong [71] proposed a qualitative model for the crossover from Brazil nut problem (BNP) to Reverse Brazail nut problem based on a relation between the percolation effect which could be described by the granular temperature and the respective condensation for different species of hard spheres. His theory was an attempt to provide a general framework.

Much of the current understanding of the underlying mechanics for dry granular materials segregation comes from the fundamental theoretical and experimental studies of Bridgewater. Drahun and Bridgewater [27] studied the mechanism of free-surface segregation which occurs when particles are poured onto a heap. Several factors such as particle size, density and shape were studied. With a simple shear cell experimental device, Foo [28] confirmed that a single large particle in a sheared bulk of mono-sized small particles will migrate towards the regions of higher shear in which there is a greater mobility of smaller particles. In 1985, Bridgewater et al. and Foo [29] used another annular shear cell to investigate particle mixing and segregation over time. A mathematical model of the occurrence of mixing and segregation in the failure zone of a free-flowing particle was developed and compared with experimental evidence. Bridgewater and Stephens [30] continued the inter-particle percolation studies in another annular shear cell experiment with large particles in a bed of small ones. They characterized the shear gap with the presence of a concentration plateau in the center zones, which is similar to the current simulation. They also found the migration of large particles towards the center of the failure zone. Their results showed that migration occurs in the direction of a shear rate gradient and is directly proportional to the shear intensity.

Savage [2] designed an annular shear cell consisting of two concentric, circular, disk assemblies mounted on a fixed shaft. The bottom disk assembly was driven by a variable-speed DC motor and the top disk assembly was restrained from rotating by a torque arm connected to a force transducer. The granular material was placed in an annular trough between the bottom disk and annular ring on the top. The bottom and top

surface of the shear cell were lined with coarse sandpaper to increase the wall roughness, while the vertical walls of the trough were very smooth. Typically, the apparatus was thus designed to determine shear and normal stresses as functions of solids concentration and shear rate. In one of the tests, spherical polystyrene beads having a bimodal size distribution (30% of 0.55mm particles and 70% of 1.68 mm particles) were well mixed at the beginning of the test sequence.

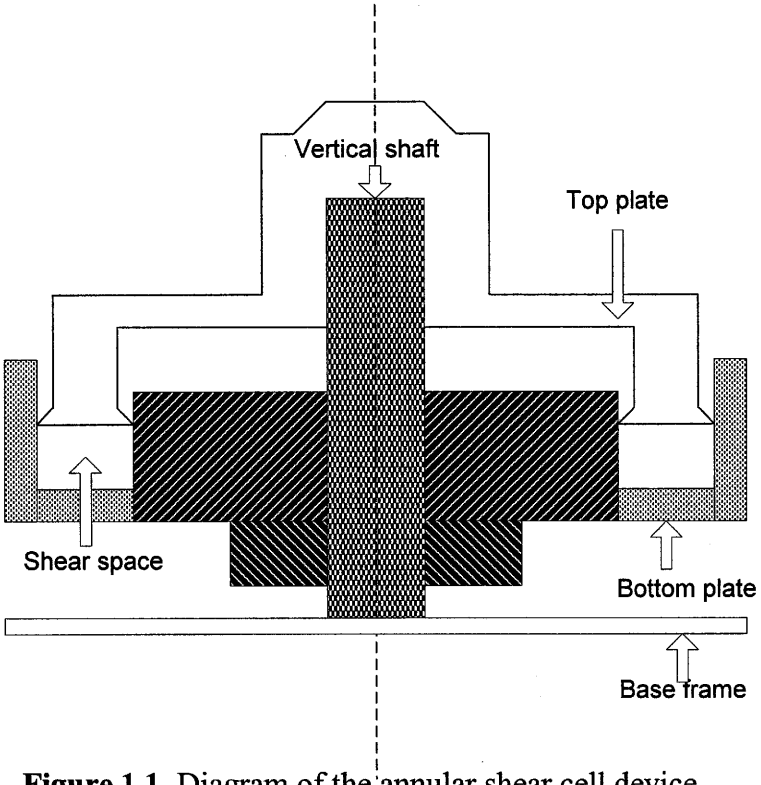

Figure 1.1 Diagram of the annular shear cell device designed by Savage [2].

It was observed that the primary shear flow in the shear cell was accompanied by a weak secondary flow in which particles moved radially inward at the top of the material and radially outward at the bottom. Typical shear and normal stresses measurement taken at the upper annular lid indicated that they were not uniformly distributed in the radial directions, and are higher at larger radii due to the segregation. A test with a binary

mixture dry granular material showed the segregation occurred in the radial direction where the fines migrated and concentrated at the outer radii. Savage explained this phenomenon as the fine particles percolation through the coarse particles which is driven by centrifugal force.

Savage and Lun [3] introduced binary mixtures in their chute-flow experiments where the particles were composed of identical material but with different sizes. In this inclined chute experiment, the bed surface had a large roughness so that granular flow was sheared in the presence of a gravitational field. Segregation occurred in which small particles percolated to the bottom and the larger ones drifted to the top of the shear layer. In order to collect the size distribution data, splitter pates were arranged to measure concentration profiles for each species at various points along the stream-wise direction. It was observed that a concentration difference quickly developed along the stream-wise direction. Zones of 100% fines grew sharply near the rough surface.

Savage and Lun [3] proposed a model that they termed called "kinetic sieving" to analytically describe their experimental results on segregation in which large particles are pushed to the surface and smaller particles percolate to the bed floor. Kinetic sieving consisted of two components – "randomly fluctuating sieve" and "squeeze expulsion". The "randomly fluctuating sieve" was devised to account for the fact that for a given solids fraction, the probability of a small particle encountering a big enough opening was assumed to be greater than that of a large particle encountering a gap of sufficient size. In order to maintain a zero mass flux in the direction perpendicular to the bed, a counterflow mechanism was introduced that allowed particles (both small and large) to percolate only towards the impermeable bed floor. The second mechanism, "squeeze

expulsion" took into account force imbalances on an individual particle that could cause a it to be squeezed out of its own layer into an adjacent one. Savage and Lun [20] proposed that this mechanism was not gravity driven or size preferential, and that it operated in either direction, and that the contact forces were more likely to force large particles upward than small ones. However, if small particles percolate downward more often than big ones, size segregation will occur regardless of whether the large particles are preferentially squeezed upward or are equally likely to be pushed either up or down.

Observations of Takahashi [31] showed some interesting phenomenon in small sized debris flow where coarse particles concentrate at the margins of the flow regime. In the study, randomly mixed sand and gravel slide down a roughened fifty degree inclined chute connected with a horizontal section where the gravel segregated to the front and top after the material came to rest. This observation was similar to the sorting process when mixtures of coarse and fine sand were used. Takahashi [31] suggested that this inverse longitudinal sorting occurs because large particles migrated upward owing to dispersive stress, then move to the front because velocities are faster in upper layers. The particles reaching the front tumble down and are buried in the flow. But if they are larger than the surrounding particles, they will again migrate to the surface.

Davies [32] performed experiments where particles flow on a roughened treadmill adjusted so that the flow front remained stationary. At high enough Froude numbers, the flow broke up into individual surges where large particles migrated to the front of the flow and accumulated at the nose. Films of Davies' [32] experiments confirmed that large particles circulate near the front of the flow, and fine particles migrated toward the tail of the flow in a circulatory path. In the case where more material was added and the height

was greater, the shear strain rate in the upper parts of the flow was small. Shear strain is necessary for the kinetic sieve to operate, and, where it is small, longitudinal segregation diminishes.

Recently, Khosropour and Zirinsky [33] have investigated the size segregation of a binary mixture in their shearing cylinders. They observed the migration of the larger particles coincident with the experimental results of Savage [2]. In their experiments, all the particles with a larger size ratio than those of the flow medium rose to the top surface of the Couette shear cell and remained on the top over a wide range of shear rates. Extensive measurements of the speed of the bigger tracer particles showed the dependency of size ratio on the motion. They believe that this segregation is a byproduct of the convection, because the flow medium appeared to go through a convection-like motion under shearing. They assumed that the convective nature of the flow which is found in the shearing medium should be the mechanism driving the segregation process. After measuring the position of a single intruder particle, they determined the convection pattern of this shear flow. Although the shape and the number of the convective rolls were not very clear, it is well known that the boundary roughness, and shear rate play important roles in creating convection. In addition, a peculiar transition, similar to laminar to turbulent, was noted in their measurement of the segregation velocity. This transition was marked by a sudden increase in the standard deviation of the vertical velocity and a deviation from the linear mean velocity field. They believed that this transition is dominated by diffusion and particle collision which is critical in the forming of convection rolls. The current DEM simulation study also revealed that the wave length of convection roll in the ring shear model have the relation with the boundary conditions.

1.2.3 Size Segregation Theory Analysis

Jenkins and Richman [34] developed a kinetic model for granular flows, by including the energy dissipation due to inelastic collision. Their theory assumed that the particles interact via binary collisions, usually using a constant coefficient of restitution to represent the energy dissipated by the normal impacts between the particles. This method has been further applied to solve shear flow problems. Jenkins and Richman employed the averaging technique in kinetic theory of dense gases flow to calculate the energy and momentum flux transferred between flow disks and boundary walls. With the energy equation, they established the relations for the shear stress, pressure and flux of fluctuation energy. Richman [9] extended their theory with smooth spheres, where a modified Maxwellian velocity distribution was used to analyze shear flow driven by the bumpy boundaries. He predicted the existence of a relation between boundary roughness and slip velocity of the shear flow near the boundary.

Jenkins and Mancini [35] formulated a similar theory for granular mixture in 1989. They derived the balance laws and a constitutive relation for plane flows of a dense, binary mixture of smooth, nearly elastic, circular disks. Their study focused on the flux of momentum due to binary collisions. The disks referred to their study may have different radii and masses and collisional properties. In a reduced gravity field, collisional flows become possible and the segregation is mainly driven by spatial gradients in the energy of granular velocity fluctuations. After the flow reaches steady state, segregation is triggered by the momentum balance exchanged in contacts among different species. This process requires the gradients of particle fluctuation energy to be balanced by concentration gradients.

Farrell, Lun and Savage [36] derived conservation equations for the rapid flow of a binary mixture of spheres. This theory is appropriate for smooth, inelastic spherical granular particles in a system where collisions dominate the motion. In a simple shear flow, they predicted that stresses will decrease with increasing concentration of smaller particles and decreasing diameter ratio of small to large particles.

Willits and Arnarson [37] developed a more precise theory based on the study of Jenkins and Mancini [35]. The constitutive relations for the binary mixture of nearly elastic, circular disks are developed by using the Chapman-Enskog procedure and by incorporating the Revised Enskog Theory derived by Van Beijeren and Ernst [38]. As a correction to Jenkins and Mancini's work, the viscosity which was calculated by integrating the shear stress correlation was quite close to the results of their simulations.

1.2.4 Simulation Studies of Segregation

Many investigations of granular Couette flow using the Discrete Element Method have been carried out. Earlier simulations have focused on the flow mono-sized, inelastic particles between bumpy walls, such as the studies of Kim and Rosato [14] and Lun [39]. On the other hand, Karion and Hunt [40] introduce mixed systems with different sizes to check the effect of solid faction ratios between species on the wall stress.

Two-dimensional Couette flow simulations of identical, inelastic, smooth disks driven by bumpy boundary walls were reported by Louge et al. [13]. Using a two-dimensional Fourier analysis of the concentration field, they found the relationship between the size and strength of these microstructures and the magnitude of the stress, thus showing that there is correlation between the magnitude of the stresses and the formation of inelastic microstructure. They found that disks tended to remain together

after collisions when the restitution coefficient was small. They also established that in the dilute limit of the flow, the kinetic mode dominates, and in the dense limit, the collisional mode dominates.

Another simulation for Couette flows of inelastic, frictional disks with flat walls was done by Campbell and Brennen [11]. Distributions of velocity, density and granular temperature were computed. It was found that the granular temperature was low across the central portion of the flow and large in the high-shear-rate regions next to each solid boundary. The high-temperature zones also corresponded to the low-density regions. In the absence of conduction effects and at constant density, their results showed that the temperature was proportional to the square of the shear rate.

Campbell and Zhang [41] used a wall model in which the flow-disks could collide with both the wall disks and the exposed flat area of the wall to study the transition from fluid-like to solid-like behavior of the Couette flow. Their research identifies a relation between the fluid-like behavior and Mohr-Coulomb failure criterion in the case where the particles are in the quasi-static regime. The results show that for a granular flow, the glassy-solid transition identifies, not the fluid/solid phase-change, but the initiation of the transition from rapid to quasi-static flow.

Lun [39] used a hard-sphere three-dimensional model to simulate Couette flow with boundaries composed of half spheres and a flat plate. He showed that there exists either an optimal wall-particle area fractions V_w for which the stresses may be maximized or the velocity slip may be minimized. At high solids concentrations, the wall-particle concentration and distribution were shown to have a significant effect on the dynamics of the flow system.

In 1986, a uniform shear flow simulation using smooth, inelastic, monodisperse disks was developed by Walton and Braun [15]. By means of non-equilibrium molecular-dynamics methods, Walton and Braun found that the kinetic contribution to the stress tensor decreases and the potential contribution to the stress tensor increases as the solids packing fraction increases. By extending the particle collision model to the spheres, they found the granular temperature generally increased as the solids packing fraction decreased, and decreased as the coefficient of restitution decreased.

Kim and Rosato [14] examined the effects of boundary properties on slip velocities and wall stresses in a Couette flow simulation using smooth, inelastic spheres. They found a dependency of these quantities on the bumpiness of the wall. A large stress drop occurred in dense flow when the shear gap was only a few particle diameters in scale, a result also found earlier by Savage [69]. Slip velocity was found to increase as the effective wall friction became larger or as the flow particles were made more elastic (i.e., as normal restitution coefficient increases).

Karion and Hunt [40] used inelastic hard-disks in their simulation of binary mixtures. For both uniform and binary mixtures, the regions of high shear near the walls exhibited low solid fractions and high rotational and translational granular temperatures. In mixture flows, the solids fraction of the large particles were negligible in the high-shear regions, an effect that was more pronounced in flows with larger discrepancies between the diameters of the two species. In good agreement with the results of Compbell and Brennen [11], they found normal and shear stresses on the bounding wall grew with solid fraction in uniform flows due to an increase in collision rate with

concentration. Also, the wall stresses increased with diameter ratio and decreased with the solid fraction ratio of small to large particles for fixed bulk solid fractions.

Simulation methods have been further developed to study granular flow and segregation in vibrating fluidized bed, inclined chutes and pouring heaps. In a vibrating bed simulation using a Monte Carlo method, Rosato et al. [42, 43] explained that the upward motion of particles in the bed is related to the higher probability of the smaller particles filling the voids generated underneath the larger ones. The mechanism has been referred in the literature as the "Brazil Nuts Effect", signifying the rise of a large particle to the surface of a vibrated assembly of uniform, smaller particles. Recently, additional simulations showed that the motion of an intruder to the surface of an energetically vibrated system can be caused by the development of bulk convection. The situation here is, however, different from the Brazil Nuts mechanism which is predominant when convection is absent. [44].

Comparison of physical experiments with DEM simulations [46] suggest that in dense flow calculations, the simulation results tend to be sensitive to the grain stiffness where the drag force arising from the interstitial fluid may have an important effect. A two-dimensional molecular dynamics study for size segregation was conducted by Hirshfeld and D. C. Rapaport [47] in which the larger grains rise to the upper surface of an inclined chute flow. Although the quantitative aspects of segregation were only probed in a preliminary fashion, it clearly shows that segregation is faster for larger differences in grain size, as well as for greater shear rates. This rate dependence was also seen in other earlier investigations.

Baxter and Tuzun [48] demonstrated the effect of impacts for size segregation on pouring heaps, in a series of granular dynamics simulation. This simulation repeats a recent experiment [48] and indicates that the stratification of poured mixtures into layers can be controlled by regulating the impact mode. High impact conditions result in new entrant particles initially embedding themselves within the heap rather than flowing down the free surface that occurs under the low impact conditions. From the marked differences in coarse fractions in the lowermost regions of the heap, they concluded that the heap was overall relatively well-mixed in a high impact mode.

Shinbrot and Muzzio's [72] experiment re-examined the Brazil-nut problem using heavy particles. In a deep bed with large vibration amplitudes, they observed that the large, heavy grains rise, but equally large, light grains sink to the bottom. This means that density plays a very important role in the phenomenon. Jenkins and Yoon [73] adopt a kinetic theory for a binary mixture of grains that differ only in size or in mass under gravity. In their predictions in the absence of temperature gradients, segregation is due to a competition between the inertia of the particles (through the ratio of their masses) and their size ratios. They were able to substantiate Hong's heuristic theory.

1.2.5 Motivation, Objectives and Methods

As mentioned above, size and density segregation are commonly observed behavior of granular material in shaken or vibrating bed [50, 51], and stockpiles [49]. Recent experiments [33], theories [8] and simulation studies [52] have revealed that in a micro-gravity field, segregation could be driven by a shearing boundary instead of an oscillating container. Jenkins and Mancini [35] concluded that in the fully-developed mixture flow, different species have different concentration gradients in order to balance the

momentum exchanged in collisional contacts among each species. Louge and Jenkins [53] constructed a shear cell experiment to observe collisional segregation driven by fluctuation energy gradients in reduced gravity fields. On the other hand, the shear cell experiment of Khosropour [33] found the existence of size segregation in a gravitational field, which suggests the existence of another mechanism for this behavior of shearing granular material --convection.

The use of discrete element simulations to duplicate this phenomenon, and to investigate the different responses of small and larger spheres under shearing will be useful in understanding this phenomenon. The simulation begins by initializing a dense assembly of particles contained in a cubic cell, with the upper and lower bumpy boundaries in a micro-gravity field. The bumpy boundaries were made of whole spheres that are rigidly fixed to parallel walls, while other boundaries are periodic. Shearing of the particles between the bumpy walls is accomplished by moving them in opposite directions at a constant velocity.

The phenomenon of interest is depicted in Figures 1.2a and 1.2b which show configurations taken at t = 0s and t = 20s, respectively from a simulation of a binary mixtures of uniform density spheres. Initially, the particles are well-mixed along the shear gap. As shearing begins, the starts to separate so that the larger particles migrate towards the central region of the flow. After 20 seconds, layers of small particles were seen to form near the moving boundaries while almost all of the large particles were in the center and away from the boundaries. Profiles of the solids fraction in Figure 1.2c and 1.2d for both species clearly show the segregation that has taken place.

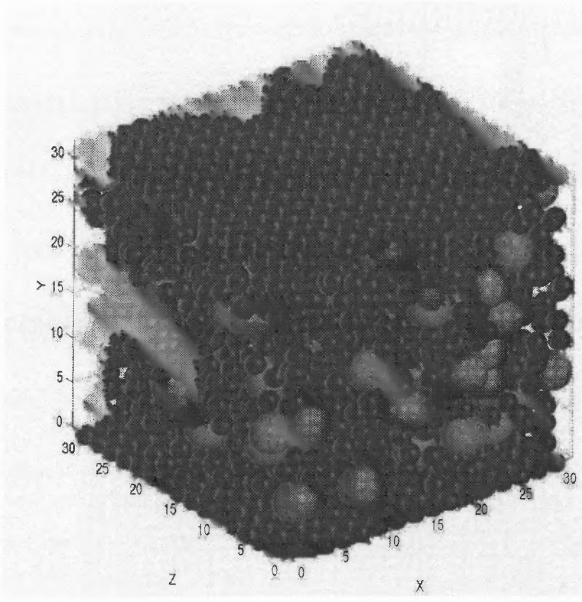

Figure 1.2a Initial status at t = 0s.

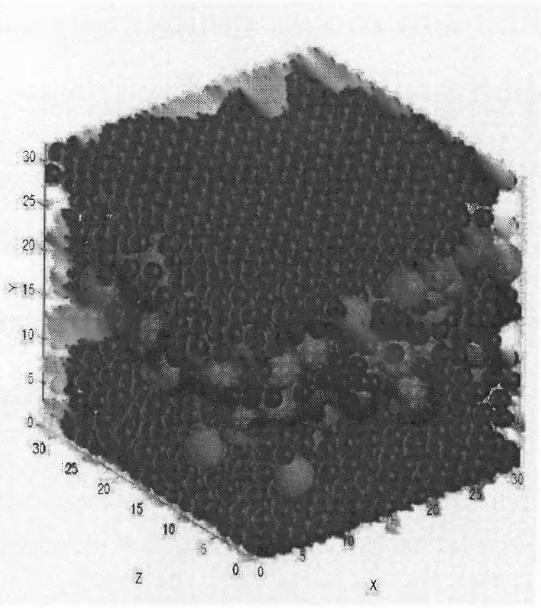

Figure 1.2b Segregation at t = 20s.

The same phenomenon was reported by Stephens and Bridgewater in their annular shear cell experiments [30]. The authors observed the migration of larger particles towards the center of the failure zone. The transition of the concentration depth profile for each species also confirmed the migration of the larger particles.

With the goal of establishing a 3D dynamics model and comparing the current

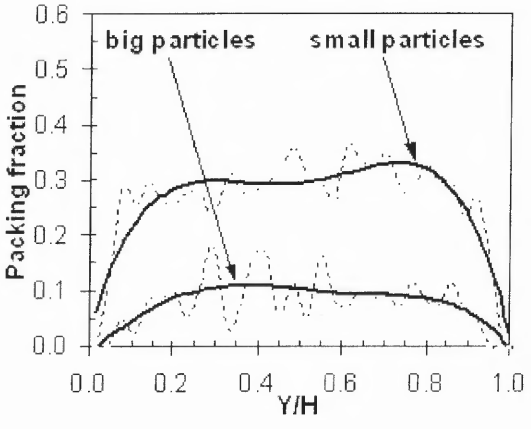

Figure 1.2c Packing fraction profile at t=0s.

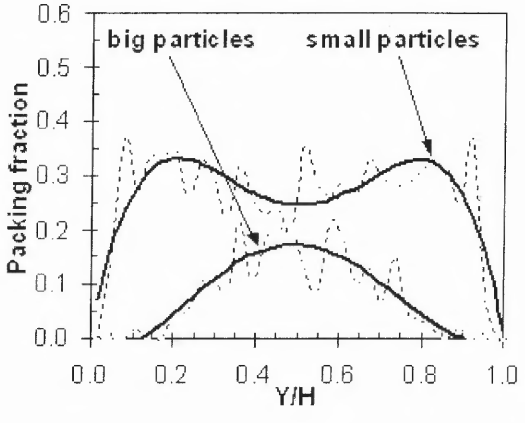

Figure 1.2d Packing fraction profile at t=20s.

simulation results obtained with existing theories, simulations and experiments, this study will is principally focused on the behavior of an individual intruder particle within a sheared monodisperse granular medium. The effect of size ratio on segregation is investigated, and a vortex-like pattern of the velocity field is identified and characterized through the use of wavelets.

1.3 Outline of Thesis

The remainder of this dissertation is organized as follows. Chapter 2 includes a description of the geometry of the Couette model, and an overview of the simulation method. After concisely introducing Walton's molecular dynamic soft-sphere model, a discussion of the boundary conditions and modification of the code are discussed along with the relevant parameters used in this investigation. In Chapter 3, the spatial and time averaging methods used to calculate the transport properties are explained. The limitations of Autocorrelation and FFT analysis for the fluctuation signal are presented while the discrete wavelet transform (DWT) method is introduced for use in the case studies. Chapter 4 includes a discussion of the general features of granular Couette flow that can be characterized via mean field depth profiles of velocity, granular temperature, pressure, and solids fraction. Furthermore, the velocity pattern of the mean shear flow velocity field is examined by checking the time and spatial averages with spectral analysis and the DWT method. Chapter 5 is concerned with the migration of one larger intruder for a series of size ratios in the simulation cell. In addition, the behavior of this single flow particle is analyzed in detail as a point of reference from which to compare and contrast with the intruder having a different size and/or mass. In Chapter 6, a

modified shear cell with a gravitational force is introduced for the segregation study, and by comparing the results from other experiments, the mechanism of the size segregation in the gravity field is determined. A summary and conclusions are presented in Chapter 7, together with other comments concerning future studies.

CHAPTER 2

3-D DISCRETE ELEMENT METHOD SIMULATION MODEL

The behavior of the intruder within the flow is examined in detail using the discrete element method (DEM) that was originally developed by Cundall [54]. The principle of DEM is to compute the trajectory and rotation of each particle (or particle cluster) in a system to evaluate its position and orientation. This is done by numerically integrating the equations of motion of a system of particles that interact via binary collisions. The forces between colliding particles are based on soft-sphere models, which will be briefly discussed further on. Other particle simulation techniques, such as cellular automaton [55] [56] and Monte Carlo methods (insert reference here) make use of random numbers and probability distributions, in contrast to the discrete element method, which is deterministic.

The main advantage of DEM is that highly complex systems can be modeled with basic data without over-simplifying assumptions. Examples include the transition from static to flowing particles in a complex hoper geometry [57-60] where continuum equations would not be tractable, or in mixing and segregation problems.

The main limitation for DEM is that it is computationally intensive, since this method uses an explicit time integration scheme and repeats sequential calculations over a limited time period with very small time steps. Due to rapid advanced in hardware, the number of particles that can be simulated within a reasonable time frame has increased rapidly in recent years. It worth noting that both the simulation size and time steps must be carefully considered in any rigorous evaluation of run time.

The DEM simulation was actually an outgrowth of molecular dynamics methods used in the field of statistical physics [61]. A critical distinction between molecular and granular systems is that energy dissipation is an intrinsic feature in the latter that must be incorporated into the collisional force models. In contrast to gas molecules, particulates cannot be modeled by perfectly elastic collisions since, during an a collision, a portion of kinetic energy is either dissipated in plastic deformation or converted into heat.

The first idea that comes to mind to simplify the level of difficulty in modeling solids in contact is to treat them as hard spheres. In the context of numerical simulation, however, the word "hard" does not imply that the collisions are perfectly elastic. It simply means that there is no interpenetration or deformation during impact. A "soft sphere" approximation is based on an entirely different principle. Here, friction and elastic restitution come into play only when spheres penetrate into each other, and the magnitude of the interaction depends on the penetration depth. In this study, the inelastic "soft sphere" ratchet contact model of Walton et al. [15] has been used, which correctly reproduces experimental observations and finite element calculations for plastic deformation in collisions.

It is important to understand that these simulations are inherently non-equilibrium in the context of non-uniform "granular temperatures". Results presented herein represent steady-state averages, which generally require only a few seconds (or equivalently approximately 30 collisions per particle per second) to achieve. The duration for the system to reach the steady-state will depend on the system configuration parameters. For example, shear ratio is critical to the turning point of the steady-state which was determined by the gap height of the simulation cell and boundary velocity.

2.1 DEM Algorithm Application

The computer simulations performed in this study uses smooth, inelastic, frictional spheres migrating in the Couette shear flow driven two parallel bumpy boundaries. These boundaries are composed of spheres (arranged in a planar square configuration) having same properties as the flow particles. The simulation begins by first assigning the coordinates of all flow particles using a random number generator. In order to avoid overlaps, the initial radii of flow particle are smaller than the input value. The radii are then slowly expanded to the desired size, where any overlaps that occur during the process are effectively removed by allowing the resulting forces to push the overlapping particles apart. Upon completing of the expansion process, all variables are reinitialized.

The motion of two parallel bumpy walls in opposite direction provides the energy source to drive shear flow. Due to rapid inelastic collisions between particles in the first few seconds after the initialization, there is a dynamic state which the energy loss from inelastic collisions cannot be balanced by the energy input provided by the parallel bumpy walls. Eventually, the shear flow will attain a steady-state situation that can be determined from the evolution of the mean velocity profile. In the study described in this dissertation, it is assumed that the coefficient of restitution is constant. However, for soft particles and/or for very energetic collisions, this assumption may be violated since it is known that the restitution coefficient is inversely proportional to the one-quarter power of the relative incident velocity. The parallel bumpy walls are moving with constant horizontal velocities in opposite directions, that is, the upper wall is moving with U in positive x-direction and the bottom wall is moving with U in negative x-direction.

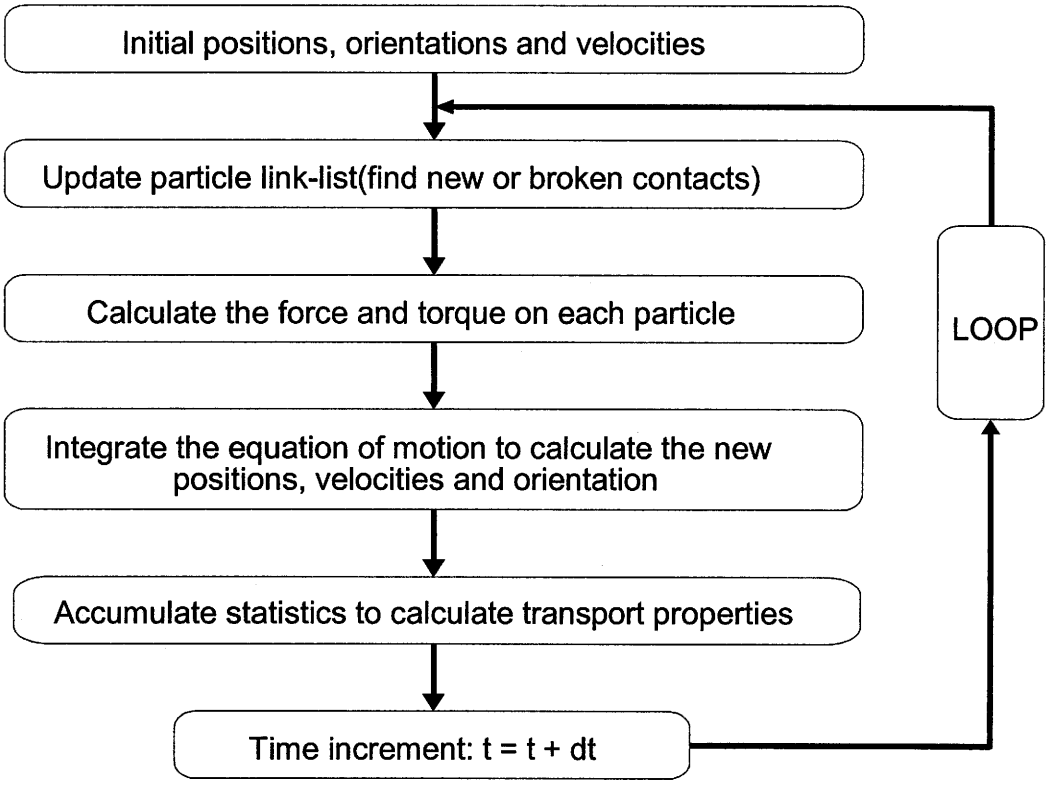

Figure 2.1 Flow chart of simulation algorithm.

The flow chart in Figure 2.1 shows the basic algorithm steps for the simulation:

i. Initializing the system and input the data for all the particles.

ii. Searching the system and referencing all the particles.

iii. Applying interaction laws (normal, tangential force and moments) at inter-particle and particle-wall collision.

iv. Integration Newton's motion equation to determine particle behavior. (position, velocity and accelerations)

v. Averaging output data with time averaging method or special averaging method, and updating the link list of particles contacts.

A more detailed explanation is discussed below by classifying the code's subroutines into five groups in accordance with these steps.

A. System initialization and data input:

i3ds

Assign input data for case studies for the geometric parameters (number of particles, particle size, computational cell size, running time), boundary configuration (boundary roughness and boundary particle arrangement and size), material properties (coefficient of restitution, friction coefficient, density) and shear condition (boundary velocity).

datain . f

This subroutine reads the input data from *"i3ds"* (unit=2).

bound . f

Assign coordinates, velocities and other properties for boundary particles. Select square coordinates for boundary sphere assigned on XZ plane at $y = 0$ and $y = H$ when " *bdry* = 1", and triangular coordinates for *"bdry* = 2". The array of boundary particles in X and Z directions could be changed in ***i3ds***.

init . f

This is subroutine initializes general parameters. Initial coordinates and fluctuation velocities of particles in a system are generated. The number of zones along the y direction and the time step are also calculated here.

Findrad . f

This subroutine finds the maximum allowable particle radii at time t = 0 and increases radii each time step thereafter until it reaches a predetermined (input) value. This subroutine will be actuated every time when the simulation start from t = 0s.

B. Inter-particle force subroutines:

forces . f

This subroutine calculates the inter-particle forces between particles. The force model used in this routine is a partially latching spring model of Walton and Braun [Walton, 1986 #65; Walton, 1986 #62]. The collisional or potential contribution to the stress tensor is calculated in this routine. In addition, the net force around the intruder particle is also calculated in this routine at each time step.

update . f

This subroutine checks all particle pairs and update the near neighbor arrays for all flow particles.

C. Integration subroutines:

initstep . f

This subroutine initializes the integration step. The zone index needed in calculating zone diagnostics is established. Using this index, volume fractions of particles which occupy each y-zone are computed as mass-weighted average quantities.

integ1 . f

This subroutine performs an iterative integration of the velocity equations to solve for v_x and v_y at the start of the current time step only. The Verlet leapfrog algorithm is used to perform the integration.

integ2 . f

This subroutine calculates the coordinates at the end of the current time step. The current coordinates will be used as the initial input information for the next running step. And this subroutine will be repeated at the end of each calculation step.

D. Diagnostic calculation subroutines:

initcum1 . f

This subroutine initializes the cumulative short-term averages of computed quantities such as granular temperature, the average velocity in each zone, and stress tensors.

initcum2 . f

This subroutine initializes cumulative long-term averages of computed quantities.

diagnos2 . f

This subroutine calculates all of the diagnostics, both locally and globally. Local volumes are called y-zones. The kinetic contribution to the stress tensor is calculated in this routine.

E. Data output and Others:

datasave . f

This subroutine writes output data to the output files:

zzbig1 : coordination of the intruder.

zzvel1 : velocity of the intruder.

zzforce1: net force around the intruder.

zzdiff: mean square displace of the intruder.

deletem . f

This subroutine looks through all near neighbors in the linked list and deletes near neighbors that are beyond the maximum distance. It is only used when the maximum distance has been reduced to save total memory used for the near neighbor.

dumpread . f

This subroutine is called from the main routine and it reads the restart information

from *"D3DS"* (unit=4).

rand . f

This subroutine is a pseudo-random number generator to create random numbers from a uniform distribution. The randomly distributed initial locations and velocities for the flow particles are generated by this sub-routine.

2.2 Contact Searching and Neighbor Lists

Within each time step of the DEM simulation, the inter-particle contacts must found. For a of N particles, each update to the linked list of contacts would require an $O(N^2)$ search if done in a direct manner. To reduce this order and thus increase calculation speed, the code has a data structure called "neighbor lists" to find new and broken particle contacts. This structure is used in the evaluation of contact forces (subroutine **Forces.f**) between particles. The algorithm searches for all "near" neighbors around a given particle i (of radius R_i) that lie within a user-specified distance denoted at "search". When the distance between the centers of particle j and i is smaller than $R_i + search$, then particle j is included with the list of neighbors associated with particle i. The neighbor lists of all N particles are stored in a large array as a formatted "linked list". It is not necessary to update the linked list every time step. Rather, updates are done (by subroutine **Update.f**) when the maximum cumulative displacement of any particle exceeds the parameter *search*. The main advantage of this strategy is that the identification of contacts requires only local searches within each particle's neighbor list.

There are cases when the algorithm fails to detect collisions so that there are large and physically unrealistic overlaps between particles. This can occur is the integration

time step *dt* is not small enough, or the particles moves so fast that they penetrate into or through the search area within given time interval. Since the calculation of collision forces between the contacting pairs contained within in the search area only considers the change in the last updated time, an error will occur when force model fails to compute the interactions due to the overlap. In the case when flow velocities are too fast, it is possible for a particle to pass right through another particle. In order to avoid such problems, care must be taken selecting particle properties (which dictate the time step), the search distance and flow velocities.

The subroutine **Update.f** plays a crucial role since it creates and updates the neighbor information of each particle's neighbor list. For each particle *i*, the routine checks to ascertain if the center of a particle *j* lies within the search region. If it does, a further test is carried out to determine if particle *j* is already in the neighbor list of particle *i*. If it's already there, then the next particle is examined. However, if particle *j* is not already in *i*'s list, it will be added to the end of particle *i*'s neighbor list. The other subroutine involved with the maintenance of the linked list is called **Deletem.f**. The function of this routine is to remove particles from a neighbor list if it has move beyond the search distance.

2.3 Computational Force Model

In this section, a summary of the normal force model for inelastic, frictional spheres as developed by Walton and Braun [15] is given. Complete details on the tangential model can be found in the paper by Walton [64] and so it will not be repeated here. The "normal" force lies in the direction connecting the line of centers of the contacting

particle pair, while the "tangential" forces lie at right angles to this. The net force on a particle-particle is given as the vector sum of all binary (pair) interactions. The specific force approximations in the code are an implementation of the "soft sphere" model developed by Walton et al. [16]. Collisions of a finite duration occur that depend on the amount of allowed overlap between particles, (generally less than approximately one to two percent of the particle diameter). Because a soft sphere model is used, flows admitting enduring contacts can be simulated.

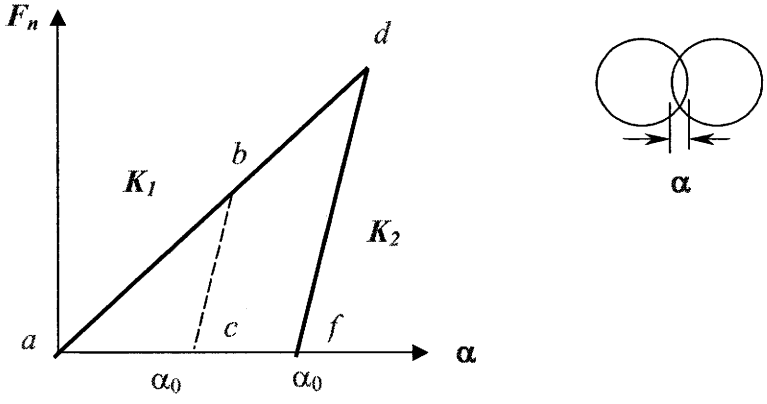

Figure 2.2 Linear normal force loading and unloading with stiffness K_1 and K_2, α is the penetration.

The collision process is divided into two parts: deformation and restitution. The deformation period is the time during which the distance between particle centers decreases, and hence the interaction force between particles increases to a maximum value. The restoration period represent the process in which the particle centers move apart, and hence the interaction force decreases from maximum value to zero. The above two steps are simplified using conventional linear springs with different coefficients of stiffness K_1 (for deformation) and K_2 (for restoration).

For two colliding spheres, the normal force (i.e., along the line of centers) consists of loading and unloading paths that are governed by linear springs of stiffnesses K_1 and K_2, respectively. (Figure 2.2) In this model, the initial loading force follows the slope K_1 from *a* to *d*, while unloading is along the line with slope K_2 (path from *d* to *f*) to a residual overlap α_0. At this point, the spheres move apart with zero normal force along the path *f* to *a*. In the case that unloading takes place from point *b*, the normal force follows path b to c with slope K_2. The model can be expressed analytically as,

$$F_{load} = K_1\alpha, \text{ and } F_{unload} = K_2(\alpha - \alpha_o) \tag{2.1}$$

where α is the normal penetration and α_o is its value when $F_{unload} = 0$. This force model has been shown by Walton and Braun [16] to have a good agreement with the experiments result and calculations from FEM analysis [62] . The normal force model just described produces energy dissipation governed by a constant coefficient of restitution given by,

$$e = \frac{V_s}{V_a} = \sqrt{\frac{K_1}{K_2}} \tag{2.2}$$

In the tangential direction, the force, which approximates Mindlin's [63] theory, admits a tangential stiffness that decreases with relative tangential surface displacement until full sliding occurs at the friction limit with coefficient μ. Full details can be found in Walton's work [64].

The approximate collision τ duration can be derived from loading and unloading period as,

$$\tau = \pi e\sqrt{\frac{m}{2K_1}} \tag{2.3}$$

Integration of the equations of motion for the N interacting spheres of diameter d is done through an explicit Verlet leap-frog difference scheme through a time step Δt given by

$$\Delta t = \tau / n = (\frac{\pi \cdot e}{n}) \cdot \sqrt{\frac{m}{2K_1}} = (\frac{\pi \cdot e}{n}) \sqrt{\frac{\pi d^3 \cdot \rho}{12 \cdot K_1}} \tag{2.4}$$

where ρ is the density of the material. For the simulations in this investigation, $n = 30$ and $e = 0.9$.

The procedure to determine the loading spring constant K_1 that was given by Lan [44] is repeated here. For uniform spheres which undergo small deformations of the order of one to two percent of the diameter, behavior is governed by the Hertzian model given by,

$$F = K_H \cdot \alpha^{3/2} = \frac{E\sqrt{d}}{3(1-\nu^2)} \alpha^{3/2} \tag{2.5}$$

where K_H is the stiffness, E is the Young's modulus, ν is Poisson's ratio, d is the diameter of the particle, and α is the relative displacement or overlap after initial contact. For this model, the maximum strain energy can be found through a simple integration as,

$$U_{\max} = \int_0^{\alpha_{\max}} F_H \cdot d\alpha = \int_0^{\alpha_{\max}} K_H \cdot \alpha^{3/2} \cdot d\alpha = \frac{2}{5} K_H \cdot \alpha_{\max}^{5/2} = \frac{2 \cdot E\sqrt{d}}{15 \cdot (1-\nu^2)} \cdot \alpha_{\max}^{5/2} \tag{2.6}$$

In the above formula, α_{max} is the maximum overlap suffered during the loading process. The kinetic energy of two colliding particles is given by

$$U_{\max} = \frac{1}{2} m v_{\max}^2 \tag{2.7}$$

where v_{max} is the maximum relative incident velocity and m is the mass of the sphere. If it is assumed that all of this kinetic energy is stored as strain energy, then

$$\frac{1}{2}mv_{\max}^2 = \frac{2\cdot E\sqrt{d}}{15\cdot(1-\nu^2)}\cdot\alpha_{\max}^{5/2} \tag{2.8}$$

from which,

$$\alpha_{\max} = \left[\frac{15mv_{\max}^2\cdot(1-\upsilon^2)}{4\cdot E\sqrt{d}}\right]^{2/5} \tag{2.9}$$

For the linear model, the maximum strain energy is found in a similar fashion so that

$$U_{\max} = \int_0^{\alpha_{\max}} F_1\cdot d\alpha = \int_0^{\alpha_{\max}} K_1\cdot\alpha\cdot d\alpha = \frac{1}{2}K_1\alpha_{\max}^2 = \frac{1}{2}mv_{\max}^2 \tag{2.10}$$

from which,

$$K_1 = m\cdot\left(\frac{v_{\max}}{\alpha_{\max}}\right)^2 \tag{2.11}$$

In the above expression, equation (2.9) may be substituted for α_{max} to obtain an expression for K_1 only in terms of v_{max}.

2.4 Data Output

There are several output files that are produced by the code, each of which can be described as being in one of three categories. In what follows, the name of the output file with the file unit number in "parentheses" is given.

A. Restart Information:

zo3ds (3):

This file describes general information about the simulation such as time step, cell dimensions, boundary type, material properties, and so on.

zvel (12):

This file stores the deviatoric velocity of each particle.

zposition (13):

This file stores the coordinates of particles.

B. Computed Transport Properties:

zenergy (14):

The energy corresponding to the particle fluctuation velocities and interactions between particles is stored in this file.

ztensor (15):

The kinetic and collisional portions of the pressure tensor for the individual layers (or y-zones) and for the entire computational cell are store in this file.

zpack (18):

The average number of particles occupied in each y-zone is stored in this file.

zxvel (19):

Mass weighted average values of particle velocities in each zone are stored.

zbdot (20):

This file stores the strain rate in each y-zone. This is used in a calculating the piece-wise linear curve for the mean shear field in a system. Each particle's random motion is then calculated using this mean shear field.

zbstress (22):

Dimensionless stresses on a boundary are stored in this file.

zgyx (24):

The deviatoric kinetic energy associated with particle fluctuations in x direction is stored in this file.

zgty (24):

The deviatoric kinetic energy associated with particle fluctuations in y direction is stored in this file.

zgtz (25):

The deviatoric kinetic energy associated with particle fluctuations in z direction is stored in this file.

zdistb (26):

The distribution of particle coordinates in x, y and z direction is stored in this file.

zveldistb (27):

The distribution of deviatoric velocities in x, y and z directions is stored in this file. The deviatoric velocities are normalized by an initial deviatoric velocity.

C. Output File Associate with the Intruder Particle:

zzbig1 (30): Coordination of the intruder.

zzvel1 (31): Velocity of the intruder.

zzforce1 (32): Net force of the intruder.

zzdiff (34): Mean square displacement of all each species.

zcv (90): Short term velocity field in XY plane.

zcvt (91): long term velocity field in XY plane.

CHAPTER 3

DATA ANALYSIS METHODS

In a dynamic simulation of granular Couette flow, it is possible to obtain a substantial amount of data from the granular flow which is difficult to extract from experiments, including profiles of mean velocity, granular temperature, pressure, and other transport quantities. Various other diagnostic computations were incorporated into the code and several post-processing methods were used to analyze the data. These are described in detail in what follows.

3.1 FFT Spectrum and Auto-correlation

The Fast Fourier Transforms (FFT) is a powerful tool to generate a spectral analysis of data generated from the flow simulation. It is possible to obtain the frequency distribution (in the frequency domain) of the position of a tracer particle. While it may appear that, for example, the motion of a tracer particle larger than the uniform flow spheres (i.e., an "intruder") is random, the spectral density function obtained from an FFT analysis suggests Brownian noise is the case. More precisely, the noise signal has a feature of that the power spectra P(*f*) is proportional to $1/f^{beta}$, where *beta* is approximately 2. Another interesting feature from the results to be discussed in following chapter is the existence of a cyclic structure in the velocity field, which has a wavelength that decays with shear rate.

In carrying out the FFT analysis, data was post-processed using MATLAB to implement the Fourier transformation with the optimized algorithm. If *P(f)* is the Fourier

transformation form of real time function $p(t)$, the power spectral density function $S(f)$ can be shown to be,

$$S(f) = \lim_{\tau_p \to \infty} \left(\frac{1}{\tau_p} \right) P(f) P^*(f) \tag{3.1}$$

Here, $S(f)$ is the spectral density function in frequency domain, τ_p is the mean value of the period, and $P^*(f)$ is the complex conjugate of $P(f)$.

Another statistical measure is the correlation function, which is useful in measuring the "similarity" between two stochastic signals generated in a granular flow. The correlation between them is determined by multiplying the ordinates of the two records at each time t and then computing the average value, denoted by $\langle x(t)y(t) \rangle$, where $\langle\ \rangle$ denotes the average over the ensemble. In the case where $x(t)=y(t)=f(t)$, the autocorrelation function is computed,

$$R(\tau) = \langle f(t) f(t+\tau) \rangle \tag{3.2}$$

If the process is ergodic, (i.e., the ensemble average can be replaced by a time average taken from only a single sample that is representative of the ensemble), then the autocorrelation can be computed as,

$$R(\tau) = \langle f(t) f(t+\tau) \rangle = \left(1/T_{\max} \right) \sum_{t=1}^{T_{\max}} f(t) f(t+\tau) \tag{3.3}$$

Here, t is the sampling time, and T_{max} is the maximum time over which the computation is performed, usually one-half of the simulation run time. In the current simulation, when autocorrelation was introduced to check the self-similarity of the velocity field, the computation always start to pick up the results at the moment when $\tau = 0$.

3.2 Mean Square Displacement and Diffusion Coefficient

The mean square displacement (MSD) of particles in a simulation can be easily computed from its definition

$$MSD = \left\langle \left| r(t) - r(0) \right|^2 \right\rangle \tag{3.4}$$

where r(0) is the position of the mass center of an individual particle at $t = 0$, and r(t) is its position t seconds later. The brackets $\langle\ \rangle$ denote an average over all the flow particles (or all the particles in a given sub-region). Care must be taken to avoid considering the "jumps" of particles to refold them into the box when using periodic boundary conditions as contributing to diffusion [48].

The diffusivity or diffusion coefficient can be computed as the long-time slope of the MSD versus time curve. The diffusion coefficient in the context of a granular flow can be interpreted as an average measure of the dispersive behavior of the flow particles. Suppose that $t = 0$, a cluster of particles is concentrated within a small volume centered at $r = 0$. After t seconds, denote the solids fraction of the cluster of particles in the unit volume centered around r by $G_s(r, t)$. This quantity obeys the diffusion equation given by,

$$\frac{d}{dt} G_s(r,t) = D\nabla^2 G_s(r,t) \tag{3.5}$$

where D is the self-diffusion coefficient. If the system is isotropic, and the initial condition is given by a delta distribution $G_s(r,0) = \delta(r)$, the solution of (3.5) is

$$G_s(r,t) = \frac{1}{(4\pi Dt)^{3/2}} \exp(-r^2 / 4Dt) \tag{3.6}$$

The quantity $G_s(r,t)dr$ represent the probability of finding a particle in a region dr around origin r at time t when the particle starts from point r at time $t=0$. Thus, the mean square displacement $\langle |r|^2 \rangle$ is computed as a weighted average in the usual manner,

$$\langle |r|^2 \rangle = \int_0^\infty r^2 G_s(r,t) \cdot 4\pi r^2 dr \tag{3.7}$$

Upon substitution of (3.6) into (3.7), one obtains the Einstein expression relating the mean square displacement to D as,

$$2tD = \frac{1}{3}\langle [r(t) - r(0)]^2 \rangle \tag{3.8}$$

The self-diffusion coefficient D is computed as the long time limit

$$D = \lim_t \left(1/6t\right) \langle |r(t) - r(0)|^2 \rangle \tag{3.9}$$

3.3 Wavelet Analysis

Fourier analysis is a mathematical technique for transforming the view of a signal such as the motion fluctuation of a particle in granular flow from the time-based to the frequency-based domain. The Fourier transform pair is

$$S(\omega) = \int_{-\infty}^{\infty} s(t) e^{-j\omega t} dt \tag{3.10.1}$$

$$S(\omega) = \frac{1}{2\pi} \int_{-\infty}^{\infty} s(\omega) e^{j\omega t} d\omega \tag{3.10.2}$$

Hence, a Fourier transform breaks down a signal into constituent sinusoids of different frequencies. For many signals, Fourier analysis is extremely useful because the signal frequency content is of great importance. But Fourier analysis also has drawbacks.

In transforming to the frequency domain, time information is lost, which means that it is impossible to obtain detailed information about when a particular event took place.

For stationary signals which have properties that do not change much over time, the results from Fourier analysis are generally acceptable. However, most of the interesting signals in this granular flow study have non-stationary or transitory features: drift, trends, abrupt changes, and beginnings and ends of collisions. A complete characterization of non-stationary signals in the frequency domain must therefore include the time aspect, resulting in the time-frequency analysis of signal. In this case, Fourier transformation could not obtain enough information from those important parts of the signals.

If the spectrum of a signal is time dependent, it is necessary to use sufficiently short segments of it to compute the spectrum--a technique called windowing the signal. Dennis Gabor (1946) maps a signal into a two-dimensional function of time and frequency which is called the Short-Time Fourier Transform (STFT). However, in the time—frequency analysis of a non-stationary signal, there are two conflicting requirements. The window width T must be long enough to give the desired frequency resolution but must also be short enough so as not to blur the time dependent events. STFT is a compromise between these two requirements--time and frequency information, while only the information with limited precision can be obtained from this method.

The wavelet transform, similar to the STFT, also maps a time function into a two-dimensional function of a and τ. The parameter a is called the scale, it scales a function by compressing or stretching it, and τ is the translation of the wavelet function along the time axis. The continuous wavelet transform of $s(t)$ which is assumed to be square

integrable, denoted as $s(t) \in L^2(R)$. Thus, the continuous wavelet transformation of s(t) is

$$CWT(a,\tau) = \frac{1}{\sqrt{a}} \int s(t)\psi(\frac{t-\tau}{a})dt \tag{3.11}$$

where $\psi(t)$ is the basic wavelet and $\psi(\frac{t-\tau}{a})$ is the wavelet basis functions.

The basic wavelet $\psi(t)$ can be real or complex, with the resulting wavelet transform being real or complex. For some applications, it may be advantageous to use complex wavelets since the phase of the wavelet transform may contain useful information. The following are examples of basic wavelets:

Modulated Gaussian (Morlet):

$$\psi(t) = e^{j\omega_0 t} e^{-(\frac{t^2}{2})} \tag{3.12}$$

where ω_0 is the analyzing frequency.

Complex Morlet Wavlet:

$$\psi(t) = \sqrt{\pi f_b}\, e^{2i\pi f_c t} e^{-(\frac{t^2}{f_b})} \tag{3.13}$$

Where f_b is a bandwidth parameter and f_c is a wavelet center frequency.

The integration operation above computes the inner product, or the cross-correlation of s(t) with $\psi(t/a)/\sqrt{a}$ with a shift τ/a. Therefore, it computes the 'similarity' between s(t) and $\psi(t/a)/\sqrt{a}$, or the component of s(t) which is 'common' to $\psi(t/a)/\sqrt{a}$. By choosing different scales a for the define wavelets, the wavelet transform can achieve any desired resolution in time or frequency.

There are four basic types of wavelet transforms:

(i) The continuous wavelet transform:

$$CWT(a,\tau) = \frac{1}{\sqrt{a}} \int s(t)\psi(\frac{t-\tau}{a})dt \tag{3.14}$$

has a parallel in the Fourier transform. The variable t, scale a and shift τ are all continuous.

(ii) The discrete parameter wavelet transform:

$$DPWT(m,n) = a_0^{\frac{-m}{2}} \int s(t)\psi(a_0^{-m}t - n\tau_0)dt \tag{3.15}$$

where the parameters a, τ are discretized to $a = a_0^m$ and $\tau = n\tau_0 a_0^m$ with a_0, τ_0 the sampling intervals and m, n integers. Both $s(t)$ and $\psi(a_0^{-m}t)$ are still continuous. The equivalent is the Fourier series, where only the frequency is a discrete parameter. For computational efficiency, $a_0=2$ and $\tau_0=0$ are commonly used, resulting in a binary dilation of 2^{-m} and a dyadic translation of $2^m n$.

(iii) The discrete time wavelet transform:

$$DTWT(m,n) = a_0^{\frac{-m}{2}} \sum_k s(k)\psi(a_0^{-m}k - n\tau_0) \tag{3.16}$$

which is a time discretization of equation(3.15), with $t=kT$ and the sampling interval $T=1$. This is similar to the discrete Fourier series, where both time and frequency are discrete. Note that for $a_0=2$, there is an output only at every 2^m sample when $2^{-m}k$ is an integer.

(iv) The discrete wavelet transform:

$$DWT(m,n) = 2^{\frac{-m}{2}} \sum_k s(k)\psi(2^{-m}k - n) \tag{3.17}$$

where the discrete wavelet $\psi(k)$ can be, but is not necessarily, a sampled version of a continuous counterpart. It is possible that $\psi(k)$ may not have a continuous time version. When $\psi(k)$ is a discretization of a $\psi(t)$, the DWT is identical to the DTWT. In this case, a parallel for the DWT is the discrete Fourier transform.

Calculation of the wavelet coefficients with continuous wavelet transform at every possible scale requires considerable computational work, and it will generate a lot of data which is hard to analyze. If discrete wavelet transformation are used in the calculation, where only a subset of scales and positions based on powers of two–the so called *dynadic* scales and positions are introduced in the algorithm, the analysis will be much more efficient without losing much accuracy.

An efficient way to implement this scheme using filters was developed in 1988 by Mallat [65]. The Mallat algorithm is in fact a classical scheme known in the signal processing community as a two-channel sub-band coder. This very practical filtering algorithm yields a fast wavelet transform-a box into which a signal passes, and out of which wavelet coefficients quickly emerge.

For many signals, the low-frequency content is the most important part. It is the part which gives the signal its identity. The high-frequency content, on the other hand, imparts fluctuation. In wavelet analysis, when mentioning approximation and details, the approximations are the high-scale, low-frequency components of the signal, and the details are the low-scale, high-frequency components.

The original signal –S, passes through a discrete wavelet analysis box which is composed of two complementary filters, while the data has been separated into two channels which represented the approximations and details in each of them.

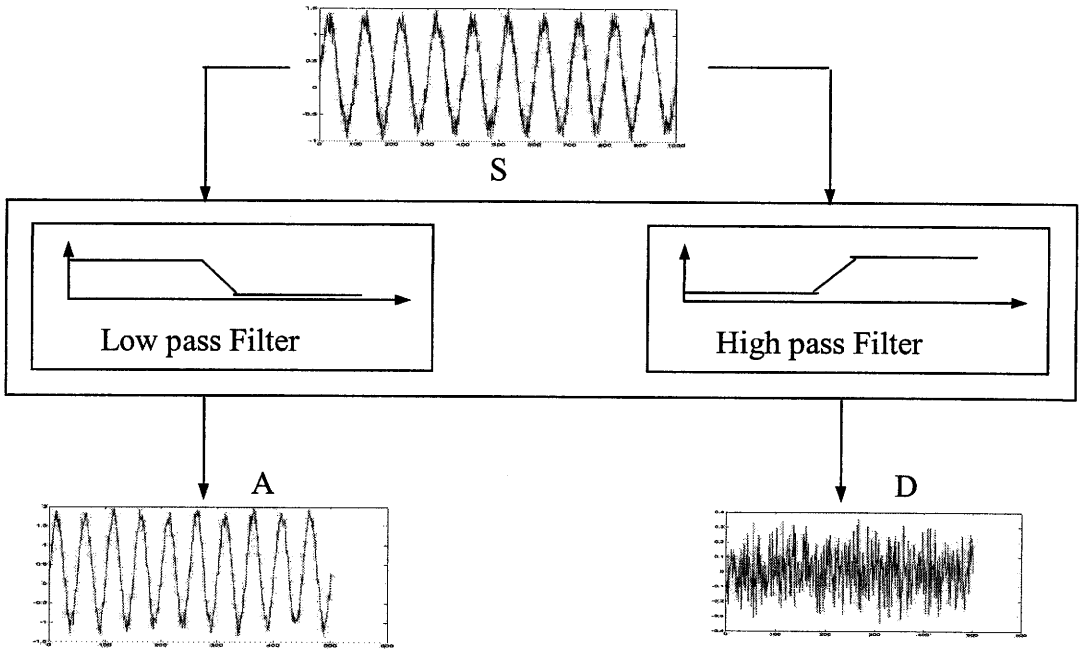

Figure 3.1 Schematic diagram for discrete wavelet transform.

It can be shown that the detail coefficient plot D is focused mainly on the high-frequency noise of the original signal, and the approximation coefficients A contain much less noise than the original signal.

The above decomposition process can be iterated, with successive approximations and details being decomposed in turn, so that one mother signal has been broken down into many lower resolution components. This is called the wavelet decomposition tree. Since the analysis process is iterative, in theory it can be continued indefinitely. In reality, the decomposition can proceed only until the individual details consist of a single sample or pixel. In practice, one selects a suitable number of levels based on the nature of the signal, or a suitable criterion. The wavelet analysis for current velocity field has been extended to 5-6 levels base on the estimation for the wavelength of the convection rolls revealed in the FFT analysis.

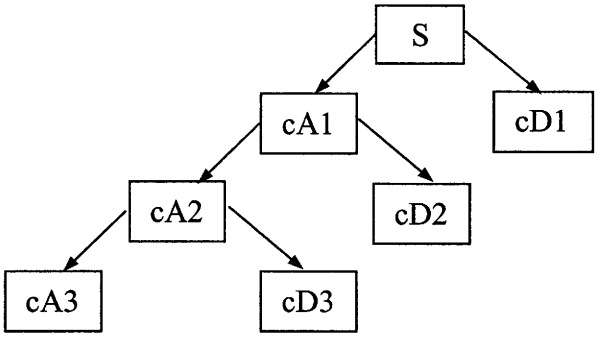

Figure 3.2 Diagram of wavelet decomposition tree.

The decomposition of signals with wavelet analysis has practical applications in the experimental study of dynamics of mechanical systems. Since scientists are interested in estimating the displacement and velocity of components of a system, the displacement data are a set of discretely sampled points which are processed and recorded by a computer connected to measurement devices. The velocity, which is defined as the temporal derivative of the displacement, can be approximated using finite differences of the displacement data. However, finite differences are very sensitive to noise, so that velocity estimates are often too inaccurate to be of practical value. Wavelet analysis can be used to practically eliminate noise and find smooth functions which accurately approximate the displacement and velocity.

Wavelet noise reduction method is based on the assumption that the displacement and velocity functions are reasonably smooth. When the wavelet components in the higher levels of the decomposition tree are discarded, the rest of the signal will reproduce the original data curve with less noise. This is particularly useful in the data analysis of the velocity pattern in the granular flow simulation along the shear direction where the

transition to vortex structures introduces a lot of noise into the major velocity curve. Using wavelet analysis to essentially remove the noise has several advantages compared to conventional Fourier or polynomial fitting methods: the associated computations are simple and inexpensive based on the calculation time, and since wavelet analyses have the ability to essentially remove the unnecessary noise, they are well suited to the processing of signals with strong background noise.

CHAPTER 4

GENERAL FEATURES OF GRANULAR SHEAR FLOW

4.1 Simulation Cell Description

The computational Couette cell consists of a rectangular control volume bounded by four periodic sidewalls as shown in Figure 4.1. The system is driven through collisions transmitted to the flow particles by upper and lower, parallel, bumpy walls that move in opposite direction at a constant velocity U. The upper and lower walls are composed of a square arrangement of spheres that have the same diameter as the flow particles. All the other boundaries are periodic: when a particle exits from right side, it reenters the simulation cell on the left at the same vertical position and velocity.

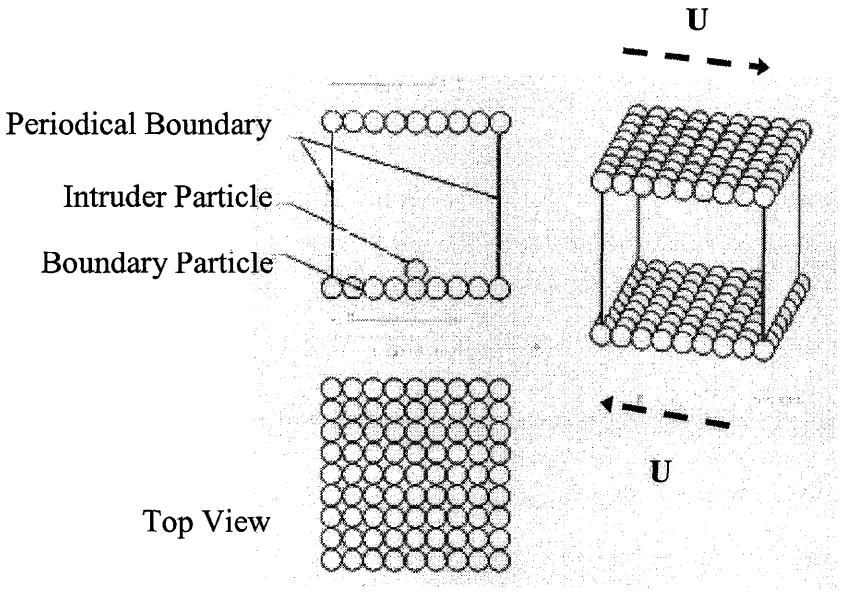

Figure 4.1 Simulation cell for Couette flow with moving bumpy boundaries.

The shear gap H is defined as the distance between the centers of the boundary particles, and hence the effective shear rate $\dot{\varepsilon} = 2U/H$ due to the opposite movement of the bumpy walls with velocity +/-U. The spheres are composed of glass, which has a mass density ρ, a normal restitution coefficient e and a coefficient of sliding friction μ. Parameters are listed in Table 4.1.

Table 4.1 Key Parameters for the Material and Simulation Configurations

Name	Value
Flow particle diameter (d)	0.02m
Gap height (H/d)	16
Average solid packing fraction (ν)	0.4
Intruder size ratio ($\phi = D/d$)	1.0-3.0
Shear rate ($2U/H$)	2.0
Material Density (ρ)	2700 kg/m^3
Coefficient of restitution (e)	0.9
Coefficient of friction (μ)	0.02

The flow has been examined in a gravity free environment since several of the preliminary studies showed that the inclusion of micro-gravity caused the system to eventually collapse, resulting in a loss of contact with the upper wall. However, kinetic theory suggests that it is possible to generate a fluid-like "grain-inertia" flow regime [3] if $\dot{\varepsilon}d/g$ is sufficiently large.

Each spherical particle has 6 degrees of freedom with the center of mass being in the geometric center of the particle. Because of the presence of the bumpy boundary, there is a limitation to the distance of a flow sphere to the boundary Figure 4.2 portrays a portion of the boundary where particles of radius r are arranged in a square lattice (S_2 = 0) with an area fraction $\nu_a = \pi/4$. The closest distance between an intruder and the boundary plane (H) increases with the size ratio of the intruder sphere (Table 4.2).

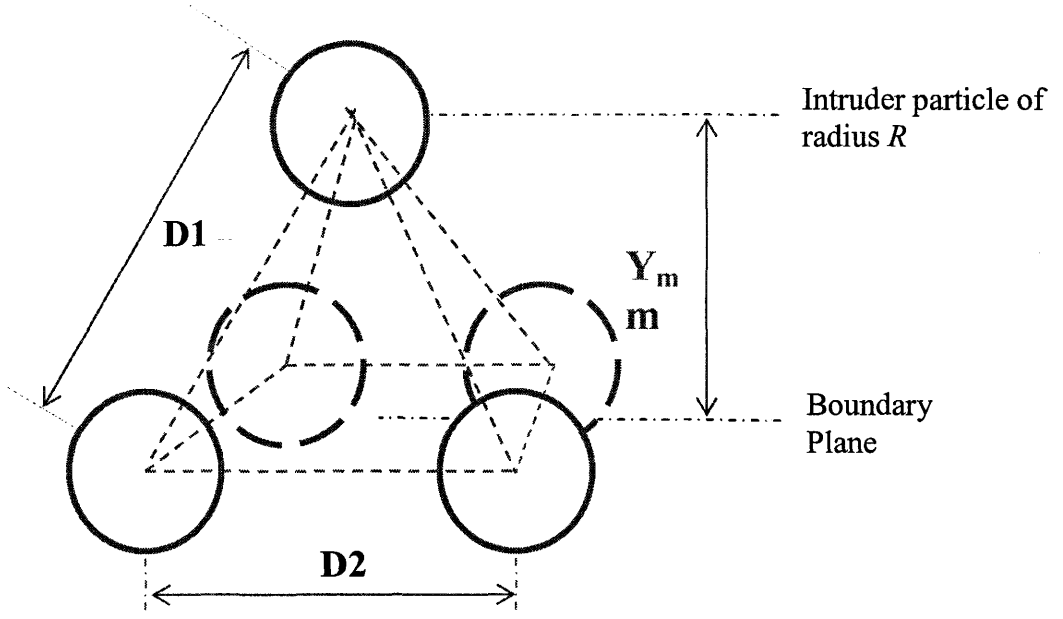

Figure 4.2 Diagram for the smallest distance between intruder and boundary plane.

At $t = 0$, flow spheres are randomly packed in the cell with a mean solids fraction (i.e., fraction of available volume occupied by solids) $\nu = 0.40$. The system quickly attains steady state after approximately 3-4 seconds, which is equivalent to about 90-120 collisions per particle (Figures 4.3, 4.4). Subsequently, data was collected to compute relevant transport quantities. All results discussed here are for fully developed flows, and computations represent mass-weighted, spatial, long time averages. However, as will be described below, the system is not in equilibrium because of the non-uniform profile of the "granular temperature" [13] in Figure 4.6.

Table 4.2 The Possible Closest Distance Between Intruder and Boundary Plane

Size ratio of intruder $\phi = R/r$, $r = 1.0$ (cm)	$D_1 = R + r + S_1$ $(S_1 = 0)$	$D_2 = 2 \cdot r + S_2$ $(S_2 = 0)$	$Y_m = \sqrt{D_1^2 - 2 \cdot (D_2/2)^2}$
1.0	2.0	2.0	1.414
1.5	2.5	2.0	2.061
2.0	3.0	2.0	2.646
3.0	4.0	2.0	3.742

Several of the simulations to be presented in this work indicated that the profile of the mean steady-state velocity was not symmetric. A similar finding was reported in the studies of Karion and Hunt [40] and Savage and Dai [66]. The fact that the velocity profile was not centered at zero implies that there is a net momentum flux in one direction.

4.2 General Features of Granular Couette Flow

There are several important steady-state depth profiles that can characterize the granular shear flow, i.e., mean velocity $\overline{u}$, granular temperature $\overline{T}$, pressure P and solids fraction ν. In order to remove the effect of the unstable data from the initial stage, all the averaging computations are initialized from three to four seconds after the start of the simulation. Plots of the evolution of both long term (Figure 4.3) and short term averages (Figure 4.4) show that critical after about 4 seconds, the velocity profiles reach a plateau and fluctuations are at a minimum. This is the steady-state for which energy input through collisions with the bumpy, moving boundaries is balanced by collisional energy dissipation. It should be noticed, however, that the short-term averages appear to show fluctuations that may be indicative of a secondary flows.

The slip velocity is an important quantity that provides some information about the ability of the bumpy boundary to transfer momentum into the flow. If v represents the x-component of the velocity field, then the mean velocity is $\overline{u} = v/U$, where U is the is the boundary velocity. An important feature of the bounded shear flow is that the mean velocity and granular temperature depth profiles are not linear, in contrast to a uniform shear flow [15].

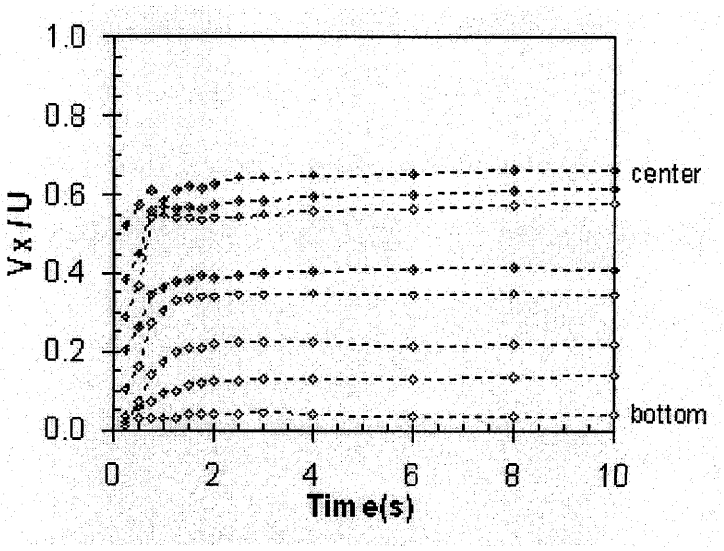

Figure 4.3 Evolution of the normalized long-term averaged velocity V_x in each layer along the gap height.

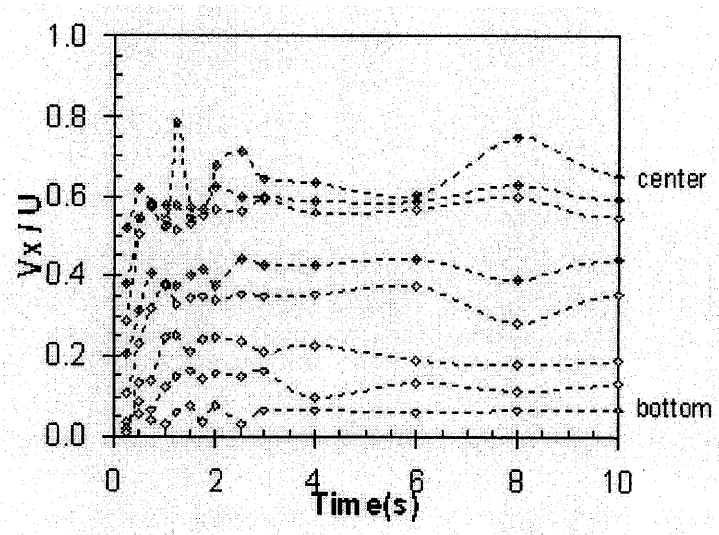

Figure 4.4 Evolution of the normalized short term average of V_x in each layer. (The time for the system to reach the steady-state is about 3-4 seconds.)

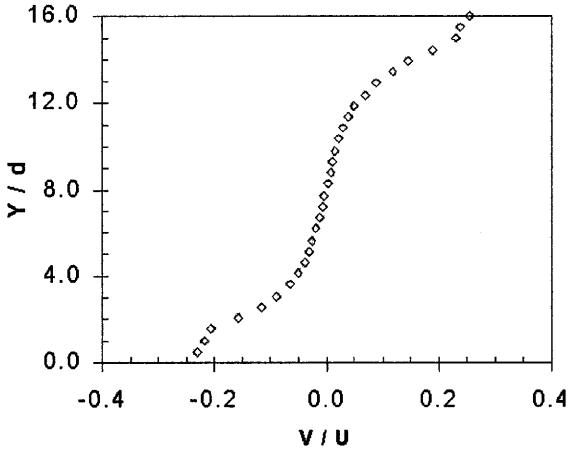

Figure 4.5a Mean velocity profile for simulation cell with a gap height *H=16d.*

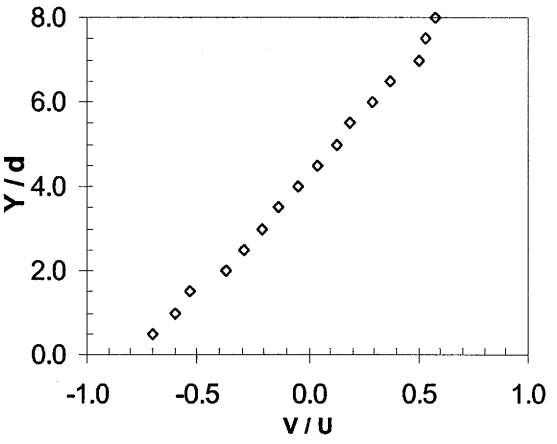

Figure 4.5b Mean velocity profile for simulation cell with a gap height *H=8d.*

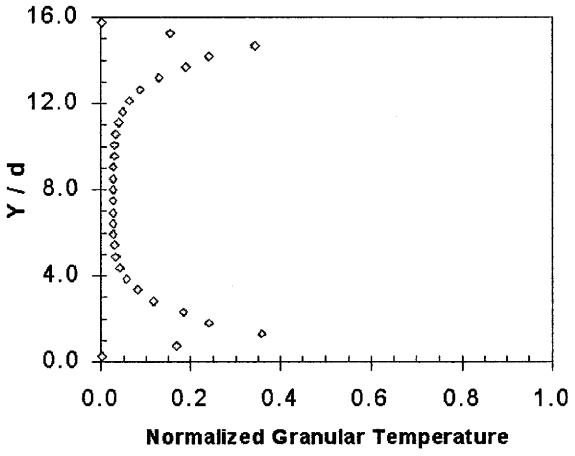

Figure 4.6a Granular temperature profile for *H*=16*d.*

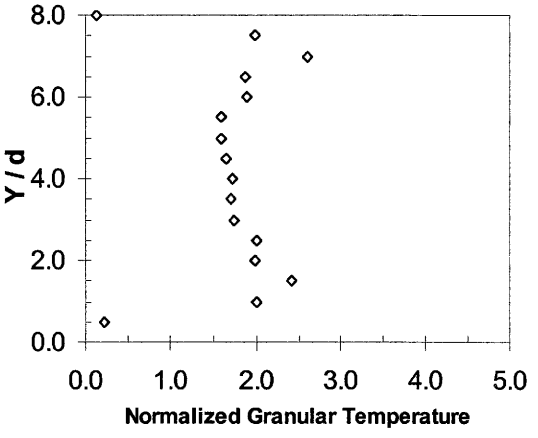

Figure 4.6b Granular temperature profile for *H*=8*d.*

A typical steady state (i.e., averaged over 100 seconds) depth profile of the velocity is shown in Figure 4.5 for the case H/d = 16, where the slip can be easily seen at the moving boundaries. Rosato and Kim [14] computed the slip velocity at one mean particle diameter $\sigma_m = 1/2(\sigma_{fp} + \sigma_{wp})$ away from the wall-sphere center plane. In the latter expression, σ_{fp} is the diameter of flow particle and σ_{wp} is the diameter of wall particle. Thus, the "slip velocity" at y = σ_m was determined from $\overline{U}_{slip} = [U - u(\sigma_m)]/U$,

where U_{slip} represent the difference between the apparent velocity U of a layer adjacent to the moving wall based on assumed non-slip linear velocity profile, and the mean flow-velocity $u(\sigma_m)$ of the same layer.

When the shear gap H is larger, the boundary is less able to supply enough energy for the volume of particles between the walls to shear, and so the curvature of the velocity profiles becomes more pronounced. Other simulations by the same authors have shown that particle material properties play an important role on the depth profile of mean velocity. That is, when the coefficient of restitution decreased, energy dissipation will be enhanced by the inter-particle collisions, which may change the slip velocity and gradient of the depth profile. In the current investigation, it was possible to affect the velocity profile and slip velocity by changing particle sizes and densities. In the current investigation, when a binary system was modeled, the depth profile of the velocity and slip velocity was different from that obtained using uniform particles at the same solids For the current simulation, when $H = 16d$, shear rate ($2U/H$) is about 2.0, the mean velocity profile has more curvature than the case when $H=8d$. The slip velocity for $H=16d$ was approximately 0.75, which is much higher than narrower system ($H=8d$) with slip velocity 0.3.

The simulations have demonstrated that the mean flow behavior is sensitive to shear gap height and other boundary properties. In the study to be presented here, for each gap height H tested, the arrangement of particles on the walls, friction coefficient and restitution coefficient were fixed.

The "granular temperature" is a quantity that describes the mass-average kinetic energy associated with the velocity fluctuations. This concept was proposed by Ogawa

[17] as an analogy between the usual thermodynamic temperature and the fluctuating motion of particles in an energetic, collision-dominated granular flow. The normalized granular temperature is computed as,

$$\bar{T} = \frac{\boldsymbol{u}\cdot\boldsymbol{u}/3}{d^2(2U/H)^2} = \frac{(u\cdot u + v\cdot v + w\cdot w)/3}{d^2(2U/H)^2} \tag{4.1}$$

where $u' = (u, v, w)$ represents the deviatoric velocity components along each coordinate direction. The granular temperature $\bar{T}$ profile (Figure 4.6) has the largest velocity fluctuations occurred near the wall due to the low solids fraction there (with a corresponding high shear rate) as well as the presence of the bumps. The temperature exhibits a steep gradient as it decreases towards the center of the sheared region, which in agreement with the simulation studies of Lun [39]. With a narrower gap height, the depth profile of granular temperature become flatter because the solids fraction is nearly flat.

The solid fraction for H/d = 16 (Figure 4.7) is smaller near the bumpy walls and higher in the center when compared with other cases with smaller gap height separation. The depth profile of solids packing fraction the system tends to arrive at fully developed steady-state for which the density is greater in the center of the channel where the granular temperature is smallest.

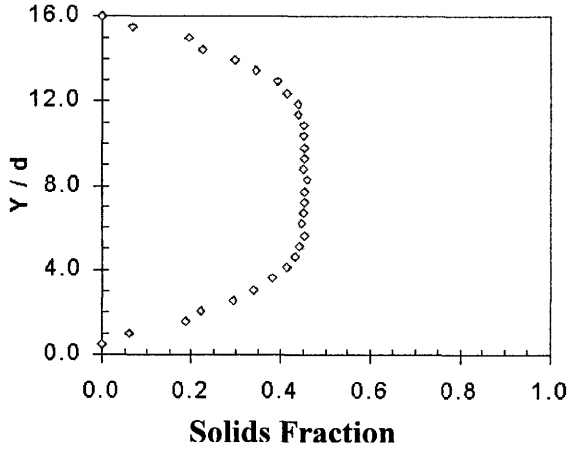

Figure 4.7a Solids fraction profile for *H=16d.*

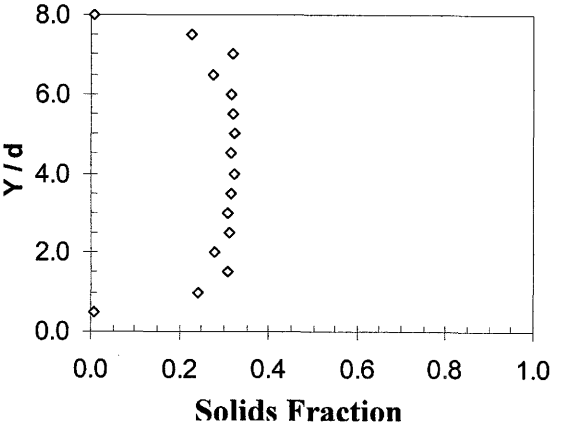

Figure 4.7b Solids fraction profile for *H=8d.*

When only one intruder of a different diameter compared with flow media was introduced, no change in the computed transport properties just discussed was found. It is also noted that solids fraction and granular temperature become flat at the same points along the profiles. This is just a reflection of the coupling between these two transport quantities.

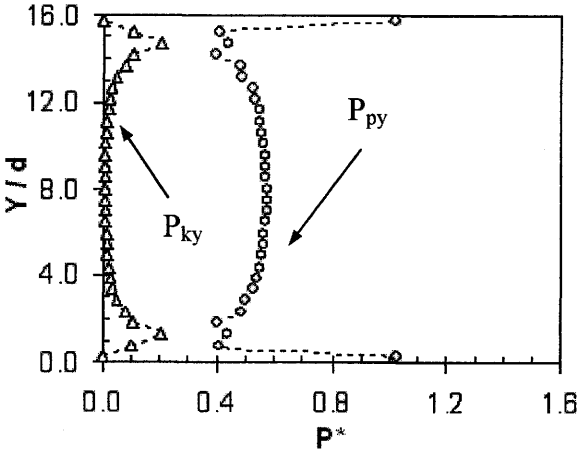

Figure 4.8 Normalized granular pressure profiles. P_{py}, and P_{ky} are the potential and kinetic components of the normal pressure, respectively.

Another transport property of interest is the granular pressure, which consists of a kinetic part due to fluctuations in particle velocities P_k, and a potential component P_p as a result of momentum transfer via collisions. Thus, the pressure can be written

$$\mathsf{P} = P_k + P_p = \frac{1}{\mathcal{V}}\left[\sum_{i=1}^{N} m_i \boldsymbol{u}_i' \otimes \boldsymbol{u}_i' + \tfrac{1}{2}\sum_{i\neq j}^{N} \tilde{r}_{ij} \otimes \tilde{F}_{ij}\right] \tag{4.2}$$

where $\tilde{r}_{ij}$ is the vector connecting the centers of particles i and j, $\tilde{F}_{ij}$ is the collision force on particle i due to j, and $\mathcal{V}$ is the averaging volume. The pressure is normalized by the product of the particle density, and the square of the diameter and shear rate [15]

$$P^* \equiv P/\rho d^2 \dot{\varepsilon}^2 \tag{4.3}$$

It was observed that the major contributor to the pressure P arose from particle collisions rather than velocity fluctuations because of the high bulk solids fraction (Figure 4.5) selected for these studies. Results shown in Figure 4.8 indicate that the potential component is almost an order of magnitude greater than the kinetic component.

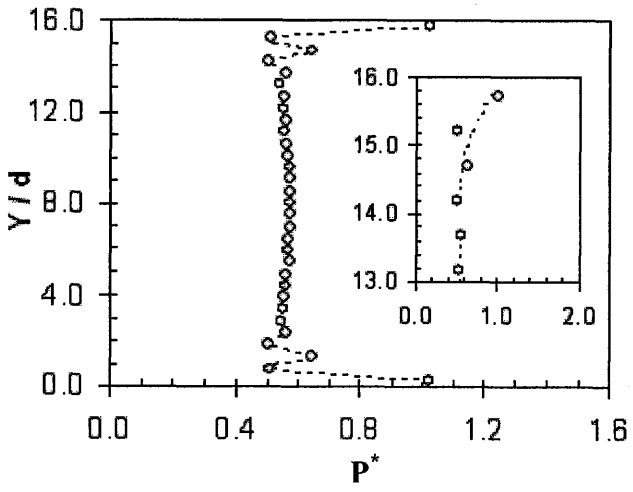

Figure 4.9 Total normal pressure with the inset shown the trend close to the wall.

The potential part of the pressure is very large at the layer close to the boundary due to the frequent collisional interactions between the bumpy wall and the flow particles. The kinetic part of the granular pressure (Figure 4.8) has a profile similar to the granular temperature (Figure 4.7) because this component is derived from the particle velocity fluctuations. The profile of total normal pressure P_{yy} in Figure 4.9, which is a mass-weighted spatial average over 100 seconds, has a sharp gradient within approximately 2.5d of the walls (see Figure 4.9 inset) where the pressure is higher. In the central region, the pressure is relatively flat. Due to relative higher pressure in the region adjacent to the boundary, all the flow particles are pushed by the pressure gradient away from the walls.

4.3 Velocity Field in the Shearing Plane

Previous work on transport properties revealed that high granular temperature and normal pressure and low solids fraction occurred in the regions adjacent to the moving boundaries. A typical long-term velocity field is shown in Figure 4.10 for 8*d* x 8*d* simulation cell. (*d* represents the flow particle diameter). The superimposed vector array represents the secondary velocity field in the XY plane (where X is parallel to the shear direction and Y is along the gap height) in which the mean X velocity has been removed so that the Y fluctuations are apparent. This is also referred to as the "secondary velocity field". A careful inspection of the direction of the velocity vectors reveals a weak single vortex-like structure. The color map indicates the magnitude of the fluctuations, which are larger near the walls. The distortion of the data in the vicinity of the periodic boundaries required that it be removed in order to display a meaningful color map.

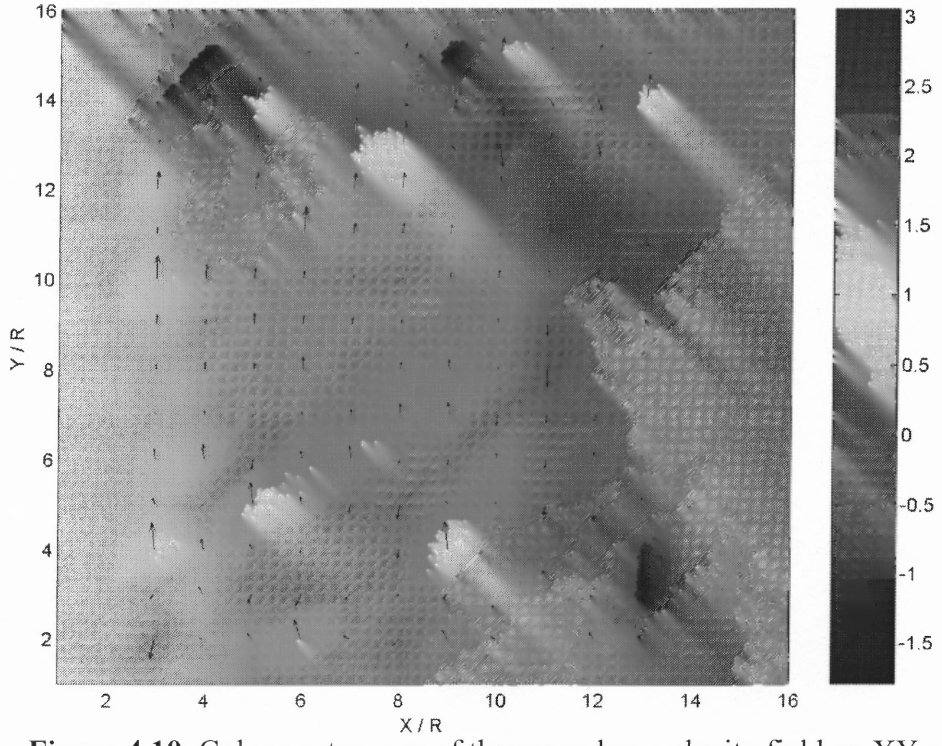

Figure 4.10 Color-vector map of the secondary velocity field on XY plane for 8*d* x 8*d* cell. A positive value in the color scale are values in the + Y direction, while negative values are in the negative Y direction.

The influence of cell width on the pattern was examined by using several channel lengths from *8d-256d* with the boundary conditions fixed. The principal finding is that the number of vortex-like structures increases. Figure 4.11 shows the computed field for a computational cell of dimensions 16*d* x 8*d*. The principal finding is that the number of vortex-like structures increases, and results discussed further on provide evidence that the wavelength of the pattern depend on the shear rate.

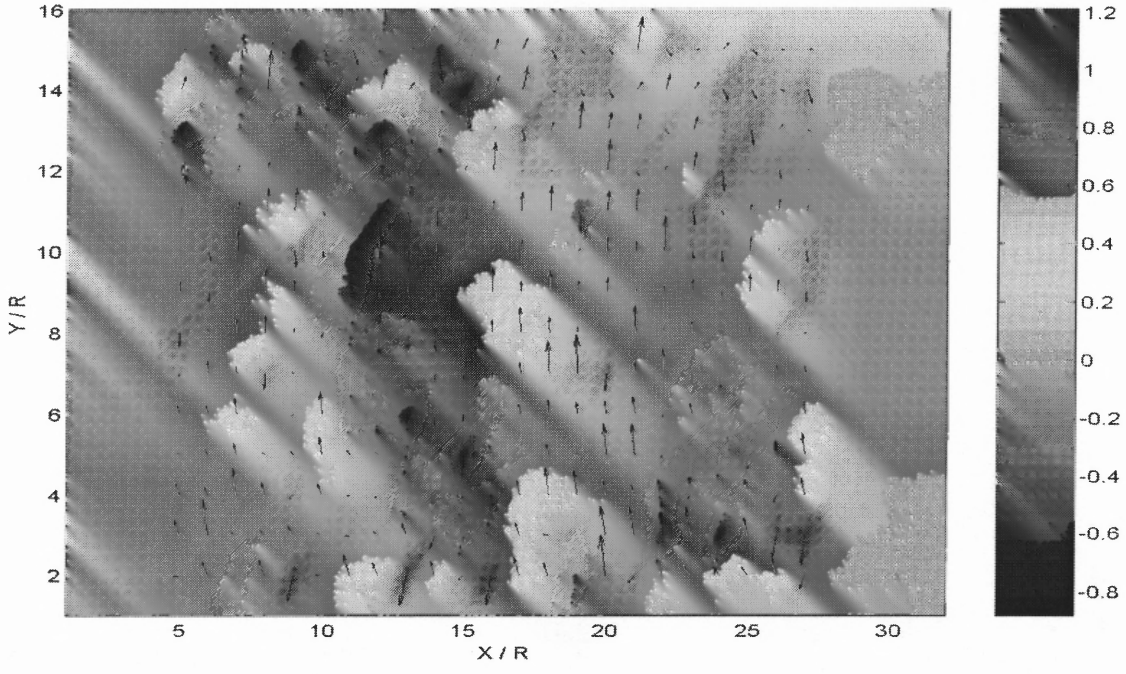

Figure 4.11 Color-vector map of velocity field on XY plane for 16*d* x 8*d* cell. A positive value in the color scale are values in the + Y direction, while negative values are in the negative Y direction.

By carefully studying the color pattern together with the velocity field arrows in Figure 4.11, it is possible to see alternating regions of upward and downward secondary motions of the particles. The question arises as to whether or not this pattern remains fixed when the boundary velocities are changed.

It is useful to find the wavelength of this velocity pattern to quantify the effect of the shear rate on the velocity field. In Figure 4.12, the simulation cell has been uniformly partitioned into N sub-cells along the shear direction (X) whose sizes are restricted to have a minimum length equal to the radius of flow particles. The instantaneous value of the velocity $V_y(x,t)$ assigned for a sub-cell located between x and $x+\Delta x$ is determined by averaging the velocities of the $N_x(t)$ particles whose centers occupy the sub-cell through the depth of the flow (Z direction). Thus,

$$V_y(x,t) = (1/N_x(t)) \sum_{i\in(x,x+\Delta x)} v_i(t) \tag{4.4}$$

The long term mean velocity field V_y is computed as a time average of the above expression given in equation (4.4) as

$$V_y(x) = \frac{1}{T}\sum_{t=0}^{T} V_y(x,t) \tag{4.5}$$

In the following simulations, three cases have been run with a fixed gap height $H=8\,d$, by varying the width of the simulation cell under different boundary velocities.

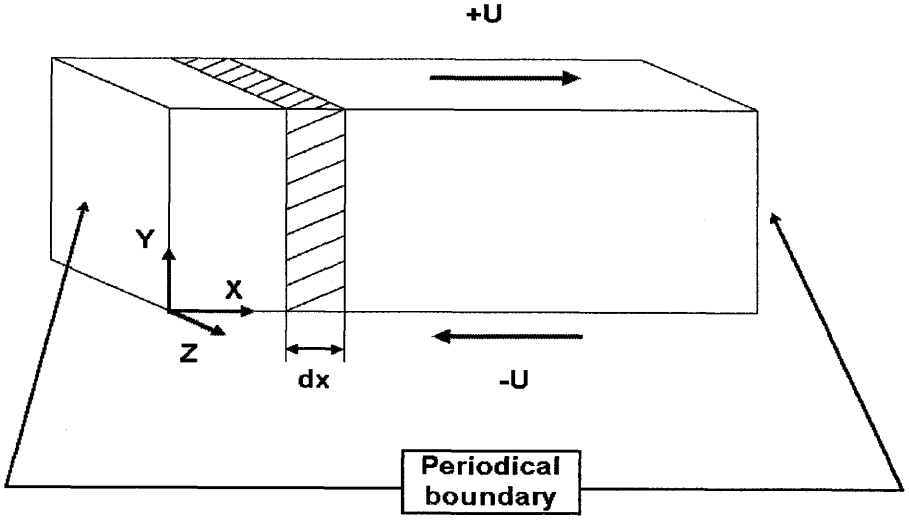

Figure 4.12 Diagram of sub-cell to compute the average V_y.

Figure 4.13a illustrates the normalized long term velocity V_y/U for which the boundary velocity U=*8 R/s*, shear rate $\dot{\varepsilon} = 2U/H = 1\,\mathrm{s}^{-1}$, and the cell width was *128d* or *256R*; (*R* is the radius of flow particle). The auto-correlation of this signal $AC(V_y/U)$ pictured in Figure 4.13b appears to have a periodic component with somewhat of a constant wavelength.

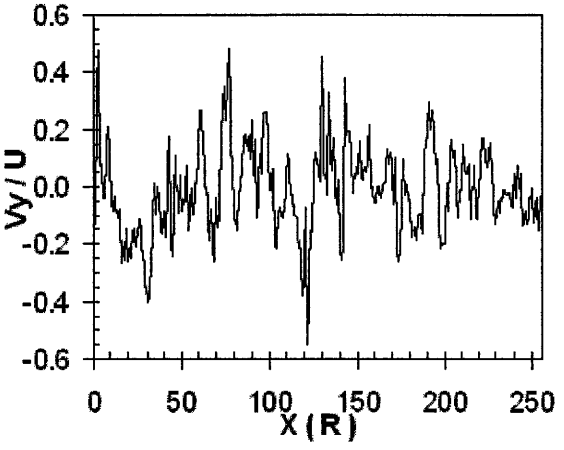

Figure 4.13a $V_y(x)/U$ for the H=8*d* cell with boundary velocity U=8 *R*/s, $\dot{\varepsilon} = 1\,\mathrm{s}^{-1}$.

This provides support for the existence of vortex-like structures in the secondary (or fluctuating) velocity field. The power spectrum obtained from a fast-Fourier

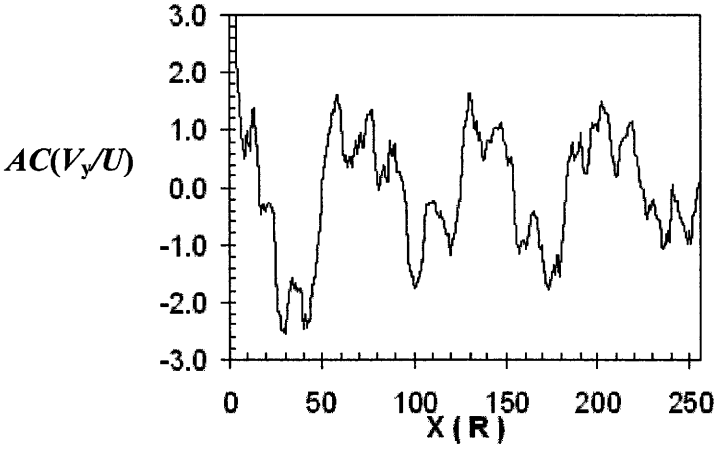

Figure 4.13b Autocorrelation function of $V_y(x)/U$ for boundary velocity U=8 *R*/s.

transform (FFT) of the auto-correlation signal shown in Figure. 4.13c reveals dominant frequency at wavelength $\lambda \cong 70R = 35d$.

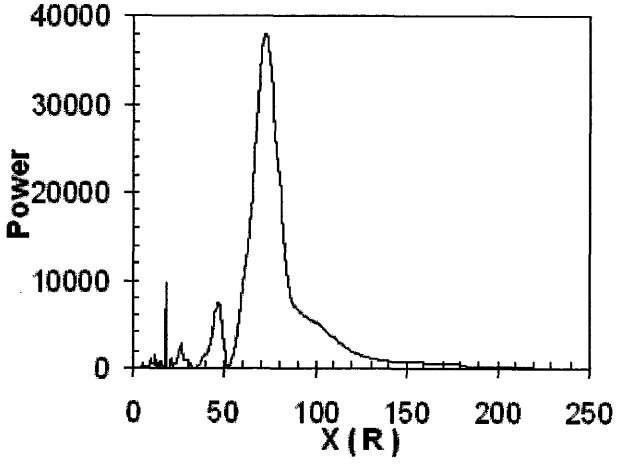

Figure 4.13c FFT spectrum analysis of the autocorrelation for *U=8* R/s, the major wavelength of $V_y(x)/U$ is about $70R = 35d$.

When boundary velocity is doubled to *U=16 R/s* and $\dot{\varepsilon} = 2\,s^{-1}$ (Figure 3.14), it was found that a cell length (= $64d = 128R$) was sufficient to because of the formation of a shorter wavelength $\lambda \cong 15R = 7.5d$. Results are depicted in Figure 4.14a-c.

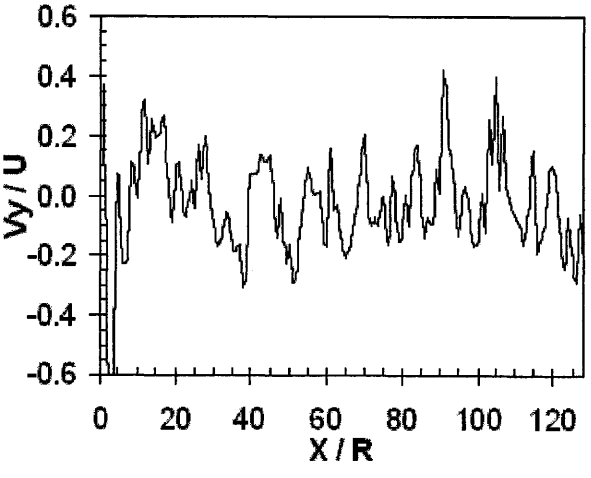

Figure 4.14a $V_y(x)/U$ for $H=8d$ cell with boundary velocity *U*=16 *R*/s. $\dot{\varepsilon} = 2\,s^{-1}$.

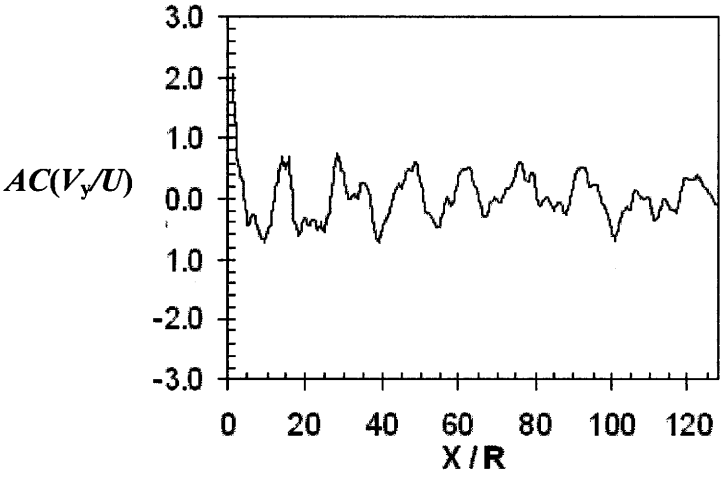

Figure 4.14b Autocorrelation function of $V_y(x)/U$ with boundary velocity U=16 R/s.

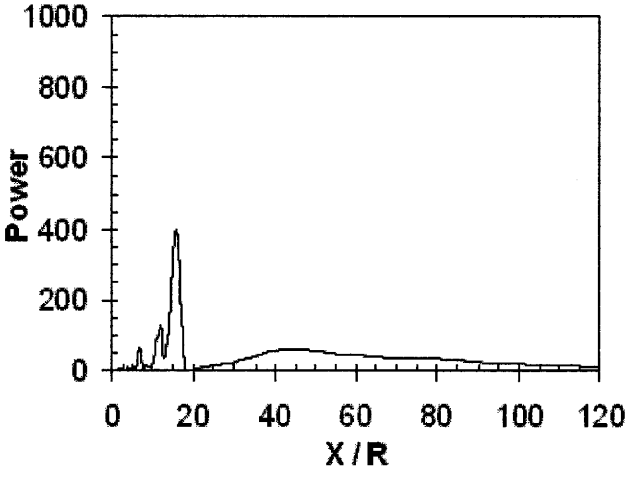

Figure 4.14c FFT spectrum analysis of the autocorrelation function for U=16 R/s. The major wavelength of $V_y(x)$ is about 15R.

While the boundary velocity is increased to U=32 R/s and $\dot{\varepsilon} = 4\,\mathrm{s}^{-1}$ a FFT spectrum analysis produced a wavelength $8R < \lambda < 9R$ (See Figures 4.15a-c). Thus, this

series of case studies illustrates that higher shear rate creates structures in the second velocity field that have shorter length scales or wavelength.

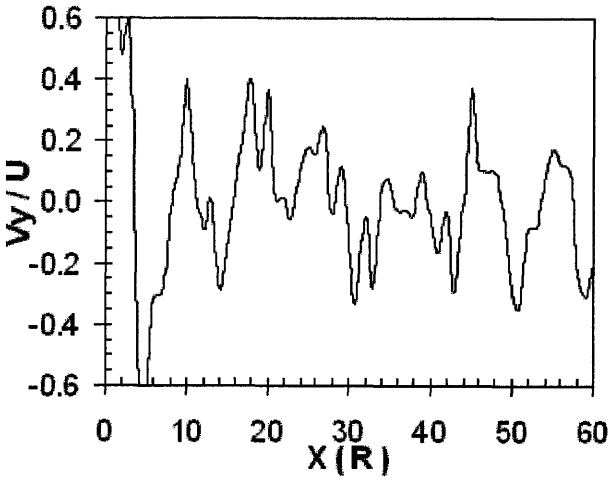

Figure 4.15a $V_y(x)/U$ for the H=8d cell with boundary velocity U=32 R/s, $\dot{\varepsilon} = 4\,s^{-1}$.

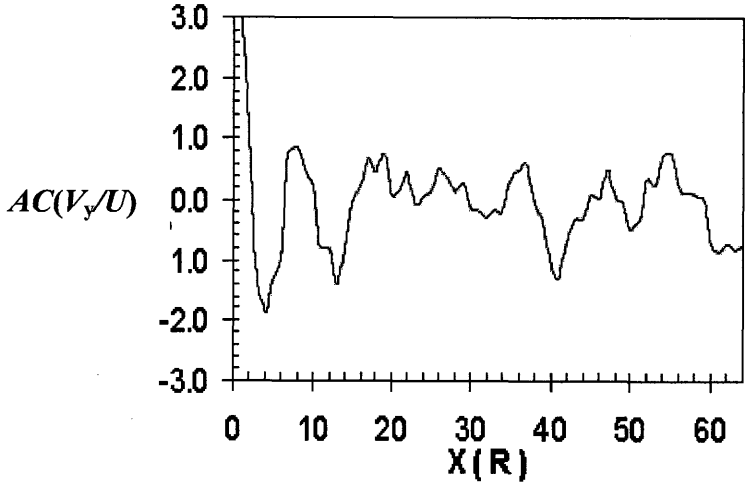

Figure 4.15b Autocorrelation function of $V_y(x)/U$ with boundary velocity U=32 R/s.

Figure 4.16 shows the behavior of the wavelength of the secondary velocity field versus shear rate for the case in which the shear gap was narrow, i.e., H = 8d. Clearly, as shear rate grows, the wavelengths decrease.

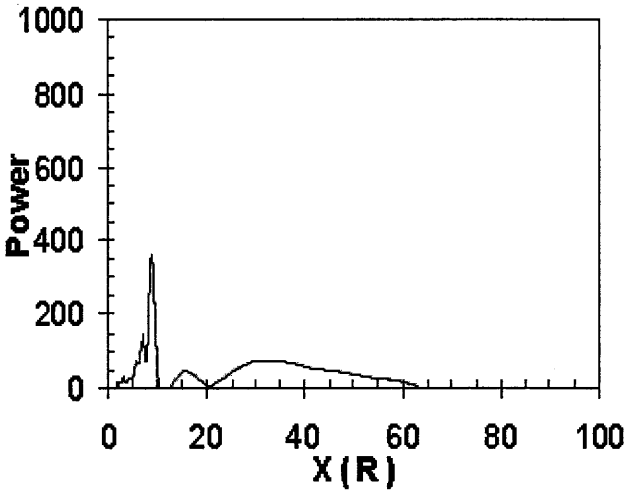

Figure 4.15c FFT spectrum analysis of the autocorrelation function for U=32 *R/s*. The major wavelength is 8*R*.

In order to determine if this dimension affects the wavelength results previously described, three gap distances H = *8d, 16d,* and *32d* were selected to examine any influence on the vortex patterns that form under fixed shear rates $\dot{\varepsilon} \equiv 2U/H = 1/s$ and $2/s$. The corresponding parameters are U= *8 R/s* with *H=8d*, *U=16R/s* with *H=16d* and U= *32 R/s* with *H=32d*. The results, although not shown here, are similar to that of Figure 4.16 except at the lower shear rates.

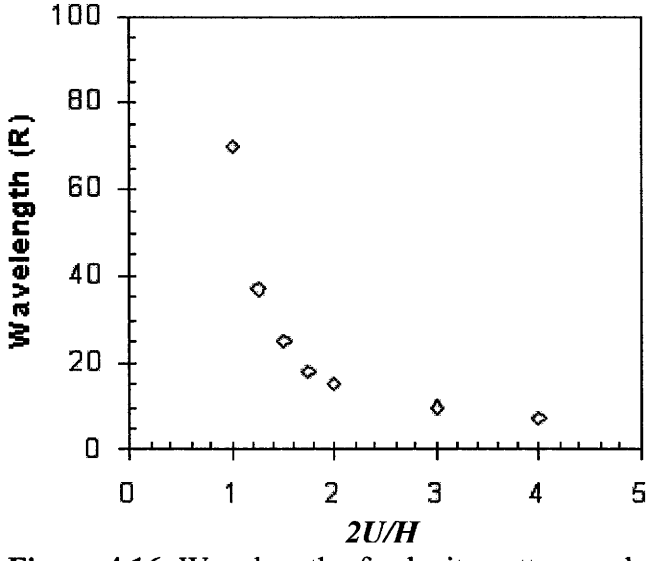

Figure 4.16 Wavelength of velocity pattern under different shear rates with shear gap height *H=8d.*

4.4 Wavelet Analysis the Secondary Velocity Field in the Shearing Plane

In the previous section, a spectrum analysis of the autocorrelation of the secondary velocity field against the cell width demonstrated the existence of seemingly stable structures with "measurable" wavelengths that decay with increasing shear rate. The analysis, however, is somewhat flawed because the Fourier coefficient derived from the FFT are affected by data over the entire signal domain. This deficiency can be removed by applying a wavelet analysis for which the spectrum coefficients can depend on local length scales.

In this section, a wavelet transform is used to decompose a signal into significant components of activity at different times and at different length scales that are useful in deciphering the vortex-like patterns observed in the $V_y(x)$ function. Here, the information of velocity field within the simulation cell with dimension $16d$ x $64d$ has been utilized for the wavelet analysis. The wavelet feature of MATLAB was used for this purpose, and the code appears in Appendix A. For a selected velocity field function $V_y(x)$, the data series were wavelet transformed and the decompositions compared and correlated in Figures 4.17a-c. Each scale of calculation gives rise to a set of wavelet coefficients defined by equation (4.6), which is simply the correlation of original data curve $V_y(x)$ and the wavelet mother curve $\psi(\frac{x-b}{a})$. The parameter b represents a spatial shift or phase change of the mother curve while a is a scaling coefficient which handles the window size for the wavelet analysis.

$$C(a,b) = \frac{1}{\sqrt{a}} \int V_y(x) \psi(\frac{x-b}{a}) dx \tag{4.6}$$

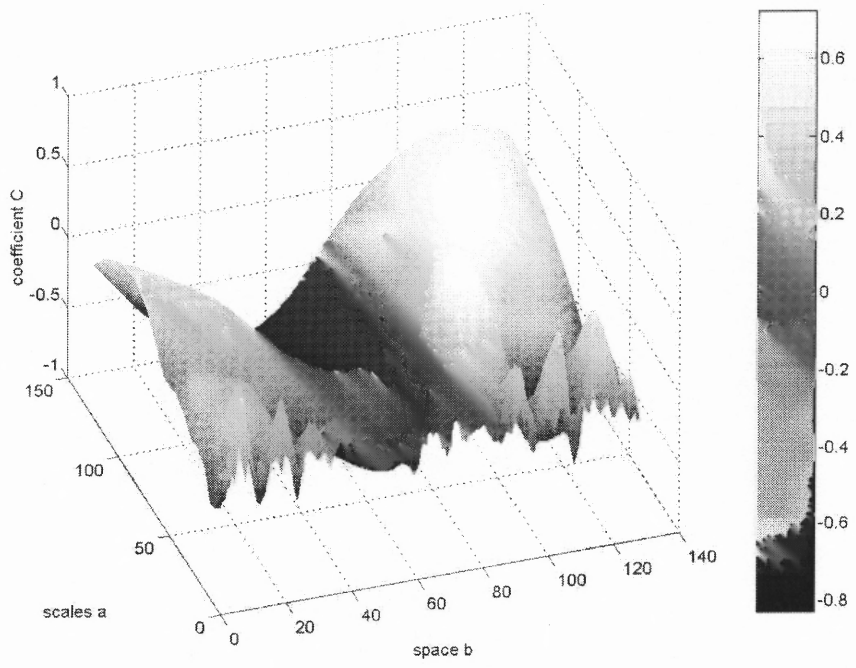

Figure 4.17a Continuous wavelet analysis for $V_y(x)$ with *U=8 R*/s, *H=8d*.

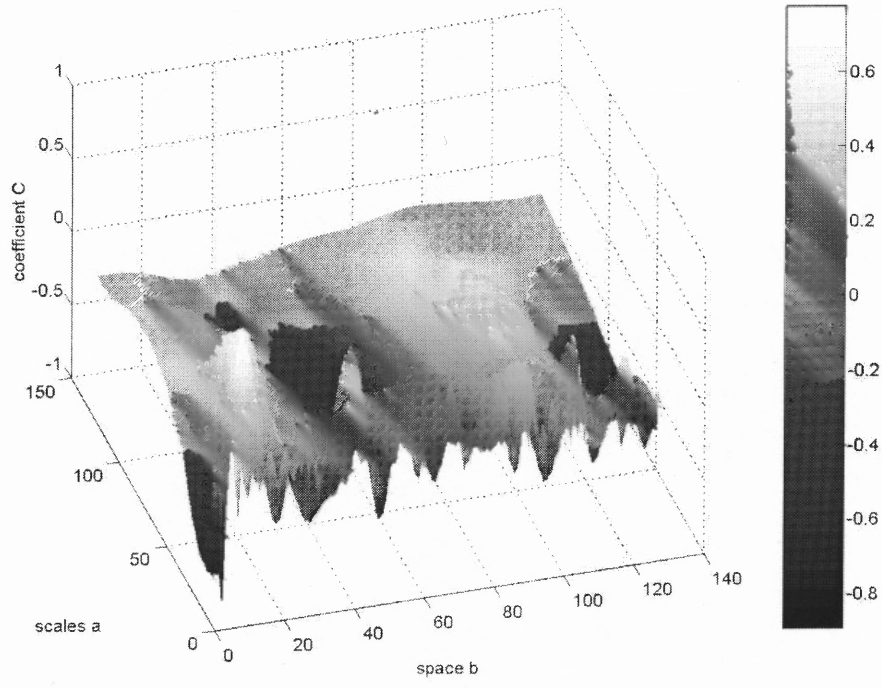

Figure 4.17b Continuous wavelet analysis for $V_y(x)$ with *U*=16 R/s, *H=8d*.

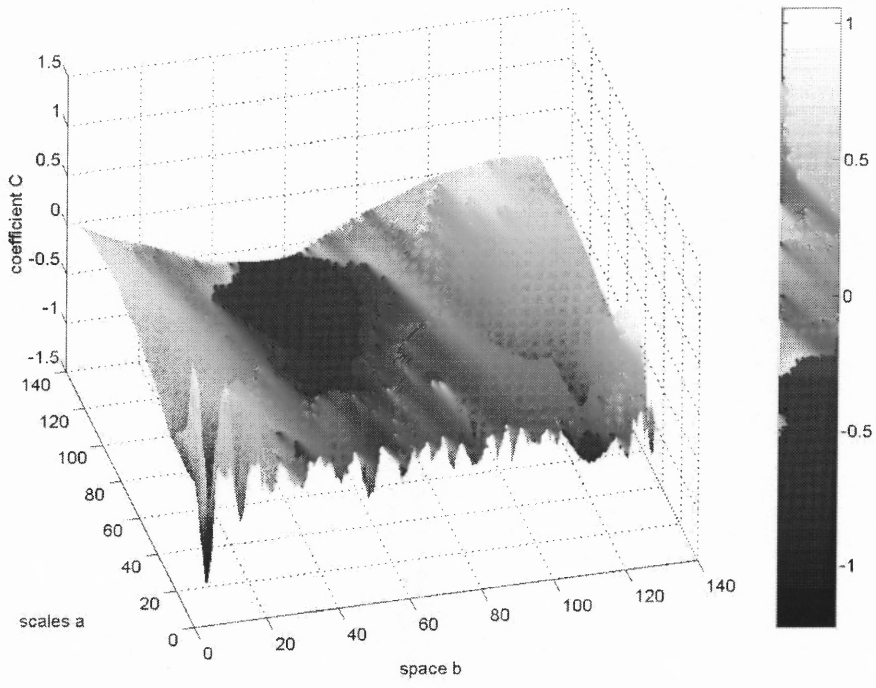

Figure 4.17c Continuous wavelet analysis for $V_y(x)$ with U=32 R/s, H=8d.

The figures show the rather complex behavior of the coefficients C for the different scales a and b. Note that a refers to the size of the "window" through which the data is processed. The colors are provided to more clearly show the positive and negative values of C. It is noted that these results were obtained using the discrete wavelet formulation described in Chapter 3.

To further isolate noise from the real data, only a subset of scales and positions based on powers of two were introduced into the algorithm using a discrete wavelet transformation. An efficient method of accomplishing this is to separate the noisy components from the data using filters called a *two-channel sub-band coder* developed by Mallat [65]. The data signal in the secondary velocity field can be decomposed into two subsignals namely, the low-frequency content gives the signal its approximation in

the high scale end (a is large) and high-frequency content yields the details in the low-scale section (a is small). The details of the method have already been explained in Section 3.3 of Chapter 3. Wavelet noise reduction method is rooted in the above filter concept. When the wavelet components at the higher levels of the decomposition tree are discarded, the remainder of the signal approximates the original data curve with less noise. The use of wavelet analysis to remove the noise has several advantages compared to conventional Fourier or polynomial fitting methods: the associated computations are simple and inexpensive, and since the wavelets have the ability to inspect signals at different scales, they are well suited for processing signals of finite length.

Figure 4.18 shows the wavelet coefficients based on the filtered signals. The original signal is denoted as S; the wavelet coefficients for the low pass filtered signal (or the approximation) are designated as A, while the coefficients of the high-frequency portion (or details) are labeled as D. The x-axis is in units of particle diameter d. The subscripts refer to the level of decomposition, which, in the current analysis, was carried to the 5^{th} level. In this current case, decomposition proceed are stopped at level 5 based on the appearance of periodic oscillation on A5 and D5, while the approximation of the wavelength is about 30-40d in sub-signal D5 for the case with boundary velocity U=8 R/s. Thus, the typical length scale of velocity pattern under this shear rate has same order of the wavelet coefficient at level 5 which is about 2^5 R. This result is consistent with that obtained from the FFT analysis for which $\lambda \cong 35d$.

As boundary velocity U=16 R/s in Fig 4.18b, the coefficients for the signal at level D3 revealed a cyclic pattern that had wavelength of 8-10d, corresponding to the typical length scale of $2^3 d$.

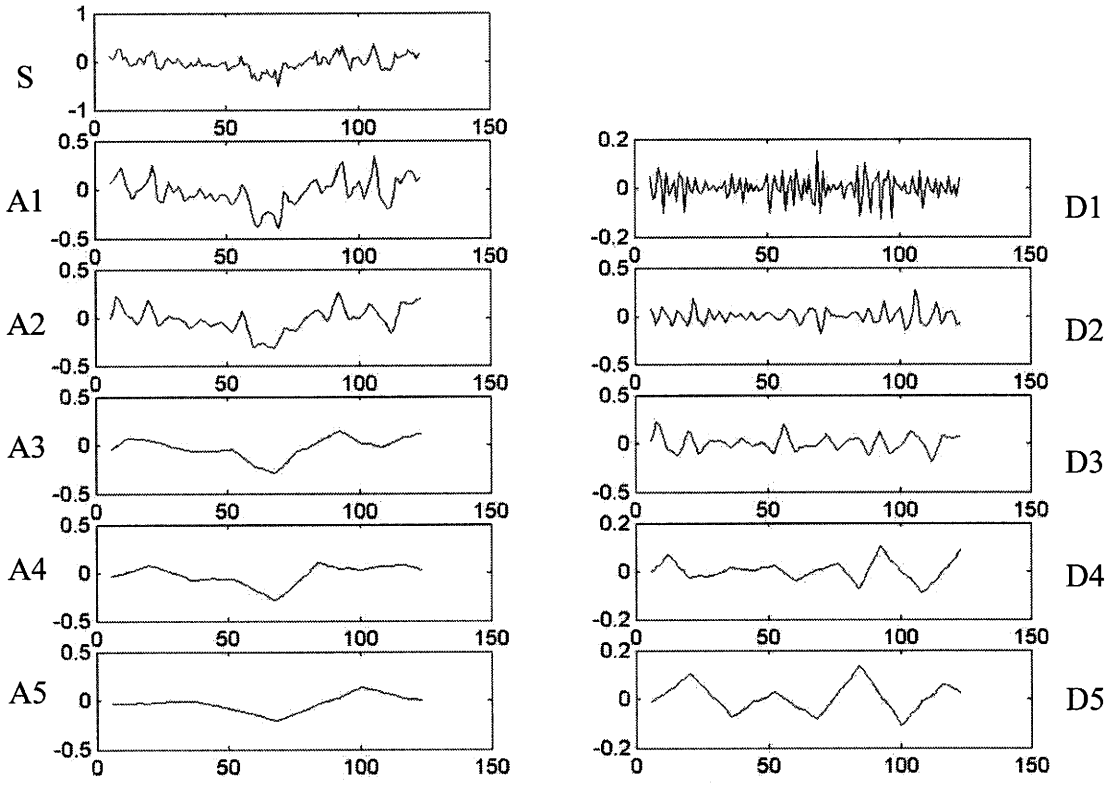

Figure 4.18a Diagram of decomposition tree of $V_y(x)$ for U= 8 R/s. Periodicity appears at the 5th level with a wavelength between 30d to 40d.

Further examination with boundary velocity U=32 R/s in Fig 4.18c showed the same trend occurred at D2 level with a wavelength dropped to 6-9d. As mentioned above, D2 level has a typical length scale of 2^2d. These results are also consistent with the FFT analysis, i.e., $\lambda_{U=16} \cong 7.5d$ and $\lambda_{U=32} \cong 4d$.

The above wavelet analysis of the time-average secondary velocity field $V_y(x)$ agrees with the FFT spectrum results. The length scale of the cyclic pattern is reduced as the shear rate increases. The presence of this secondary flow pattern in the current system should be one of the critical features for the segregation behavior in poly-disperse systems.

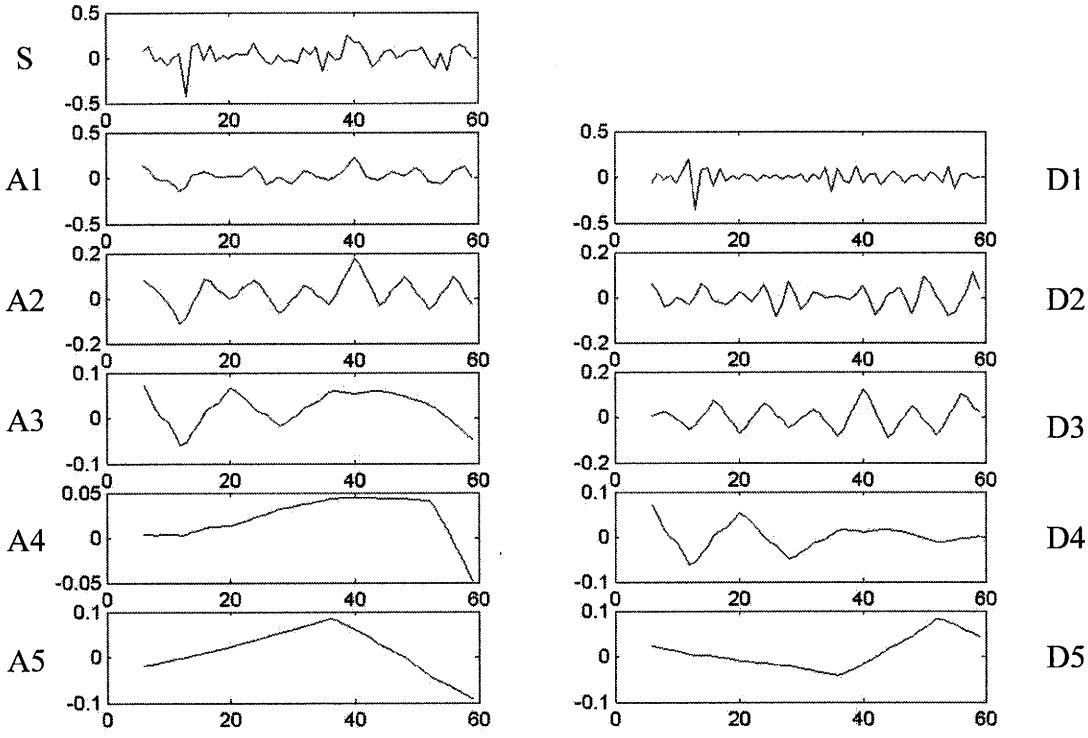

Figure 4.18b Diagram of decomposition tree of $V_y(x)$ for U= 16 *R/s*.

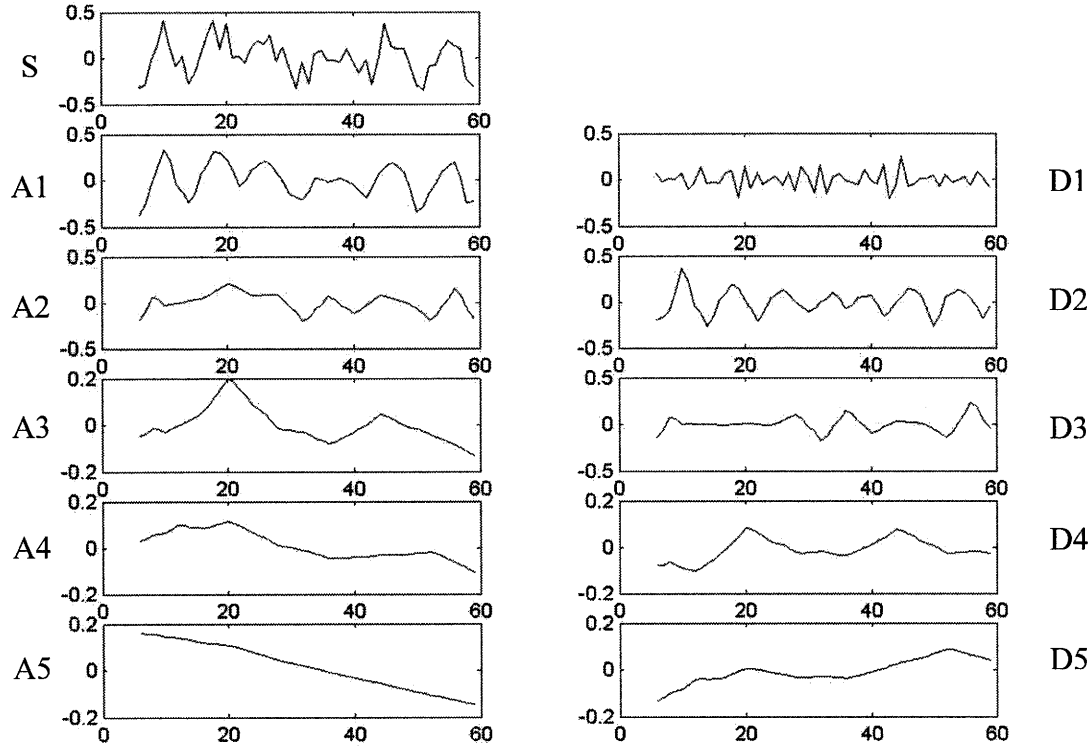

Figure 4.18c Diagram of decomposition tree of $V_y(x)$ for U= 32 *R*/s.

CHAPTER 5

MOTION ANALYSIS OF THE INTRUDER PARTICLE

In this section, the behavior of a single intruder within the granular Couette flow is examined. The simulation begins by randomly positioning particles within a cubic computational cell in which the upper and lower bumpy boundaries move at constant velocities in opposite directions. For the case studies to be described, gravity was set to zero. The bumpy boundaries consist of whole spheres similar to flow particles arranged in a square configuration, while and other boundaries of the simulation cell are periodic.

In order to demonstrate the size segregation phenomenon, a binary system of two different particle sizes ($\phi = D/d = 2.0$) is sheared. (See Figure 1.2a, b). The particle volume of the large species was 30%. Initially, the particles are well-mixed with the larger species dispersed across the shear gap.

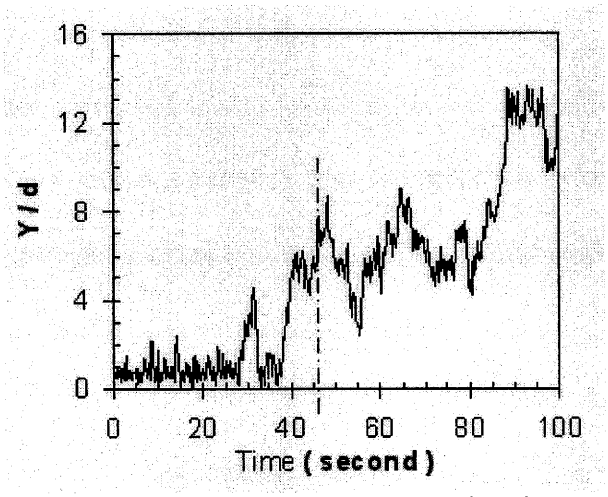

Figure 5.1a Y(t)/d for intruder with size ratio ϕ=1.0.

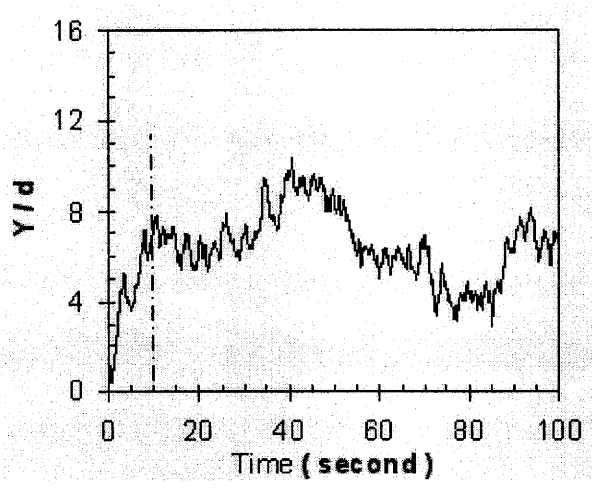

Figure 5.1b $Y(t)/d$ for the large intruder with size ratio ϕ=2.0.

During the initial stages of the process, the well mixed small and large particles begin to segregate along the gap height. In particular, small spheres move toward the moving boundary while the large spheres migrate to the center zone of the shear flow. After 15-20 seconds, layers of small particles had formed near the moving boundaries and almost all the big particles migrate to the center zone away from the boundaries in this micro-gravity simulation. Further examination of depth profile of packing fraction in Figure 1.2c-d shows this trend clearly. For both species, the variance of packing fraction is more pronounced in the middle of the shear zone as compared with the initial status. The same phenomenon was reported by Stephens and Bridgewater [30] in their annual shear cell experiments. They observed the migration of larger particles towards the center of the failure zone.

5.1 General Motion Pattern of the Intruder

In the binary system study just described, large particles moved away from the walls; after approximately 20 seconds, there was little change in the solids fraction depth profile

for each species, which suggests that the segregation process had reached a fully-developed steady-state. In this section, the results of a study of the motion of a single "intruder", whose diameter or material density differs from other uniform flow spheres is presented.

The intruder particle was initially placed at the region near to the boundary walls. A range of operating parameters was examined in a series of preliminary studies to find the most favorable conditions for the sphere to migrate. In particular, it was observed that the migration speed of the intruder spheres increased with a decreasing average solids fraction. For this investigation, the bulk solids fraction ν was set to 0.40. In addition, a series of boundary velocities was selected, i.e., U= +/-16, 32, 64 R/s (R is the flow particle radius) in a system for which H=16d.

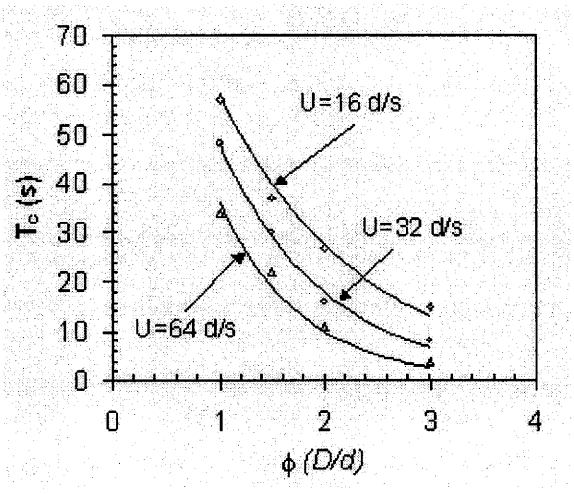

Figure 5.2 Critical time T_c versus ϕ for boundary velocity U=16, 32, 64 R/s.

In a series of case studies, the intruder is placed near the wall at t = 0, and then the flow is initiated by moving the walls at a constant velocity in opposite directions. Results

were quantified by computing the time T_c required for the intruder to cross the geometric center of the simulation cell. Figures 5.1a and 5.1b show the evolution of the normalized y-trajectories for an intruder with size ratio $\phi = 1$ and $\phi = 2$, respectively. Although it is not evident from the plots (since only a 100 second duration is shown), the large intruder ($\phi > 1$) is eventually "trapped" within a central region of the shear flow.

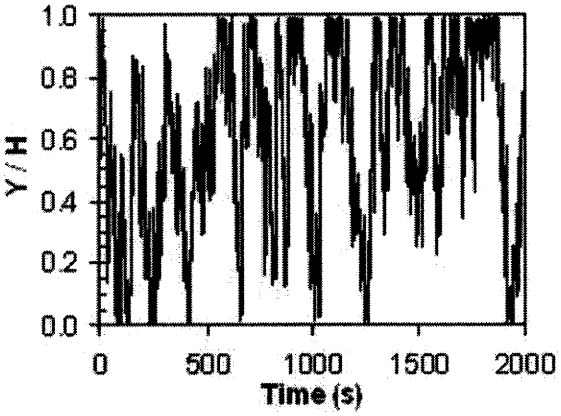

Figure 5.3a Y(t)/*H* of intruder with ϕ=1.0 in 2000s.

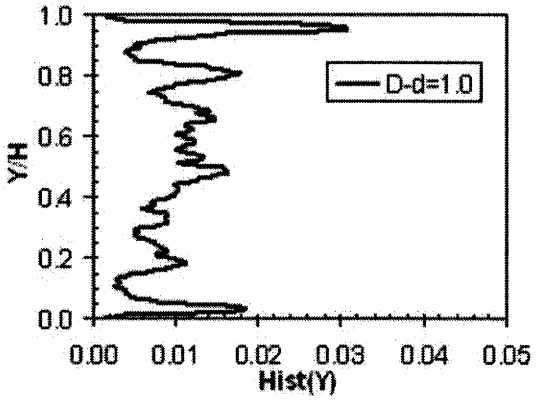

Figure 5.3b Hist(Y) of intruder with ϕ=1.0 in 2000s.

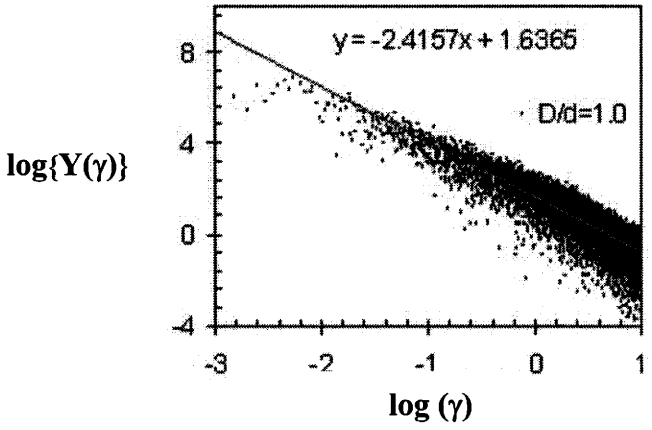

Figure 5.3c Log plot of FFT spectrum analysis of *Y*(t) for the intruder (ϕ = 1.0).

For $\phi = 1$, this trapping does not occur, i.e., the particle samples the entire shear gap for the duration of the flow. A subsequent analysis of the trajectories demonstrated

that the width of this trapping region depends on the value of ϕ. Results are summarized in Figure 5.2, which shows the dependency of T_c on ϕ, as well as boundary speed U. The curves, which are best fits to a functional form $T_c = T_0(U)e^{-k(\phi-1)}$, are included to show the trend. Here the critical time T_c was smaller with an increase of size ratio, which means a larger intruder will move to the center region of the flow with a higher velocity than the smaller ones. The shear rate, which is proportional to the boundary velocity, is also an important factor here since this sets the overall speed of the flow. This effect is visible in Figure 5.2 from the relationship between the curves at U = 16, 32 and 64 R/s.

The histories of the normalized displacement Y* along the gap for a tracer (ϕ=1.0) is given in Figure 5.3a, with its histogram Figure 5.3b and a spectral analysis plot in Figure 5.3c. In this study, the boundary velocity U = 16 R/s so that the shear $2U/H$ = 2/s. The displacement of intruder has been normalized by taking into account the geometric constraints due to the presence of the bumpy wall particles. Let $Y_m(\phi)$ denote the closest distance between the center of the intruder and the boundary plane, as defined in Table 4.2 of Chapter 4. Then, $Y^* = (Y - Y_m(\phi))/(H - 2*Y_m(\phi))$.

Power spectral density $Y(\gamma)$ of its displacement $Y(t)$ is computed in the usual form, which is $S(\gamma) = \lim_{\tau\to\infty}(1/\tau)\hat{Y}(\gamma)\hat{Y}^*(\gamma)$. Here τ is the averaging period, $\hat{Y}(\gamma)$ is the Fast Fourier Transformation of the displacement $Y(t)$, and $\hat{Y}^*(\gamma)$ is its complex conjugate. Both of x and y axis are in log scale, where the curve shows a linear relation between the $\log(Y(\gamma))$ and $\log(\gamma)$. With different particle size ratio ϕ, the curve showes different slope.

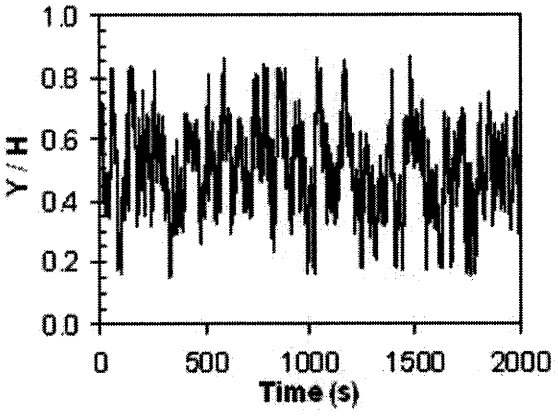

Figure 5.4a Y(t)/*H* of intruder with ϕ=2.0 in 2000s.

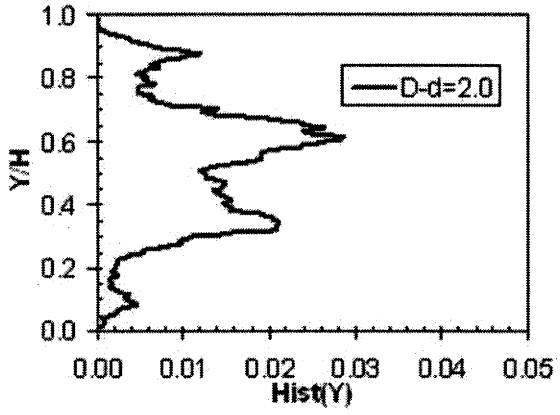

Figure 5.4b Hist(Y) of intruder with ϕ=2.0 in 2000s.

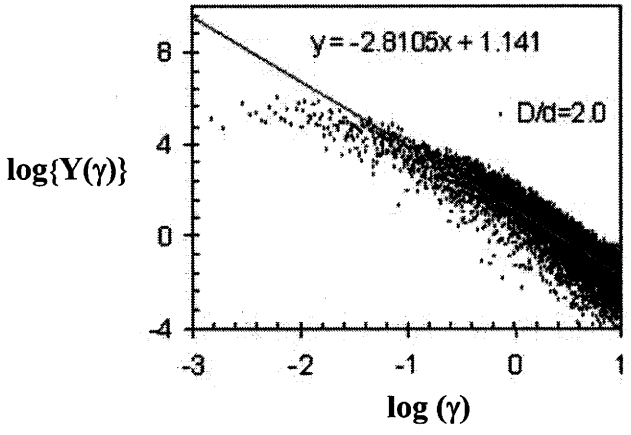

Figure 5.4c Log plot of FFT spectrum analysis of Y(t) for intruder (ϕ=2.0).

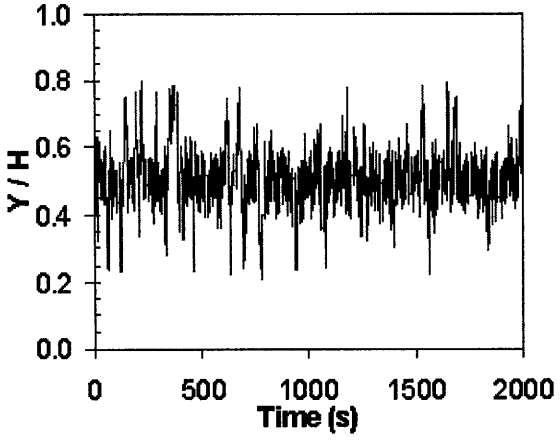

Figure 5.5a Y(t) of intruder with ϕ = 3.0 in 2000s.

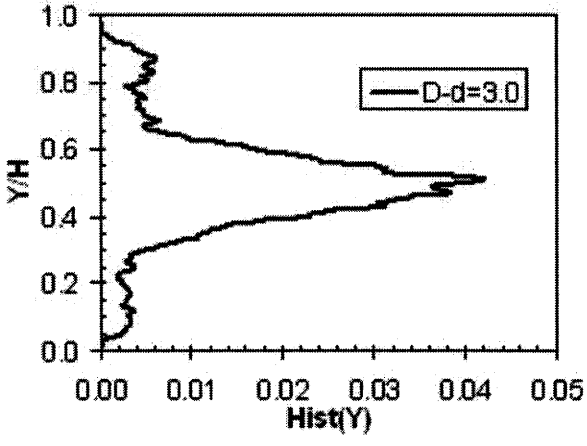

Figure 5.5b Hist(Y) of intruder with ϕ=3.0 in 2000s.

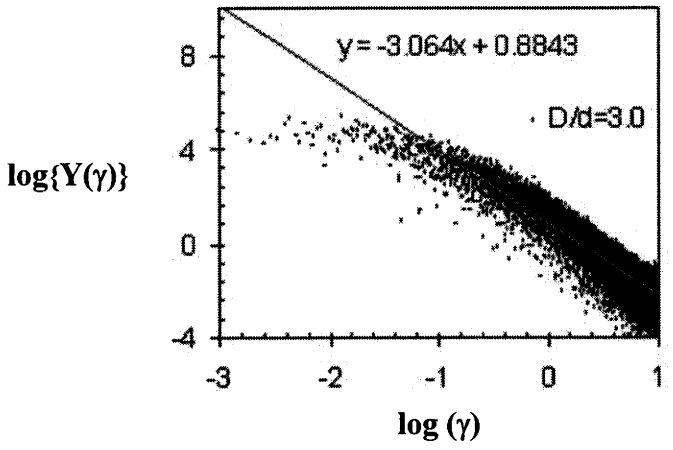

Figure 5.5c Log plot of FFT spectrum analysis of Y(t) for intruder (ϕ=3.0).

The log plot of power spectrum versus frequency shows a linear relationship so that $Y(\gamma) \propto 1/\gamma^{2\mathcal{H}+1}$ for the cases considered (ϕ = 1.0-3.0). Here, $Y(\gamma)$ is the power spectrum, γ is the frequency, $\mathcal{H}$ is the Hausdorff (or Hurst) exponent. For white noise, all frequencies contribute equally to the process, so the power spectrum is not frequency dependent and thus $\mathcal{H} = 0$. For regular Brownian motion, the power spectrum and the fluctuation frequency should such that $\mathcal{H}$ has a value ½. When $\mathcal{H}$ in not exactly equal ½, one has a fractional Brownian motion (fBm). By changing $\mathcal{H}$, fBm displays either persistence ($\mathcal{H}$>1/2), a trend of motion at any time t is likely to be followed by a similar trend at next moment t +1, or anti-persistence ($\mathcal{H}$ < ½), a trend at t is not likely to be followed by similar trend at next moment t +1. The difference between fBm and regular Brownian motion is that the motion increments in fBm are dependent on history while this relation vanishes in regular Brownian motion.

A comparison of Figures 5.3 –5.5 reveals that the displacement history depends on the size ratio ϕ. This is clearer from the histograms in which the largest intruder has

the narrowest distribution. An inspection of Figure 5.3a (ϕ = 1.0) indicates that the trajectory the tracer is random in nature. The seven peaks of its histogram (Figure 5.3b) suggest that at this bulk solids fraction (ν =0.4), the particle undergoes jumps from one layer to an adjacent one. As the size ratio ϕ increased to 3.0 (Figure 5.5), significant changes have been taken place with the motion of the intruder as can be seen from its trajectory $Y(t)$ and histogram that provides information about the fluctuation in the particle's steady-state position along the gap. The large intruder becomes "trapped" in a central region of the flow from which is cannot escape because it has settled in a low energetic region (low granular temperature) of the system. The results presented indicate that the scale of the trapping region depends on the value ϕ.

There is an interesting trend of the Hurst number $\mathcal{H}$ in the power spectrum relationship $Y(\gamma) \propto 1/\gamma^{2\mathcal{H}+1}$ with size ratio ϕ, which says something about the dynamical behavior of the intruder. For ϕ=3.0, $\mathcal{H}$=1.0 (Figure 5.5c), for ϕ = 2.0, $\mathcal{H}$= 0.9 (Figure 5.3c) and for the tracer particle (ϕ=1.0), $\mathcal{H}$ = 0.7. These results suggest that the behavior is governed by a Brownian motion with a persistent trend because in all cases, $\mathcal{H} > ½$. The growth of the Hurst Number with size ratio suggests that the intruder's dynamics at any time t is likely to be history dependent.

A description of the trajectory of the intruder from several animations revealed a close relationship with the y-component of the velocity field. Figure 5.6 shows a trace of the particle's trajectory placed again a backdrop of the positions of the particle centers projected onto the XY plane. The particle follows the shear flow as it moves away from the bumpy boundaries.

It is conjectured that the secondary flow with a vortex like structure in local velocity field influences the transverse motion of the intruder. Once the intruder reaches the center region of the flow, it remains here and simply fluctuates around an equilibrium (steady-state) location. In addition, this pattern of motion appeared to be independent of the starting location of the intruder. For example, when the intruder was initially placed near slightly off the geometric center of the flow, it will quickly moved toward an equilibrium without reaching the boundaries.

The above behavior is in contrast to that of a typical tracer particle, whose motion was quite persistent in the sense that does not get trapped. In some typical runs, when the tracer gets bumped into the zones below than the center, it migrates towards the positive x-direction for a while. Then, as soon as it finds itself above the center, the direction of its velocity reverses. This movement suggests a circulation in the XY plane that is the combined effect of the secondary flow and a depth-dependent net force.

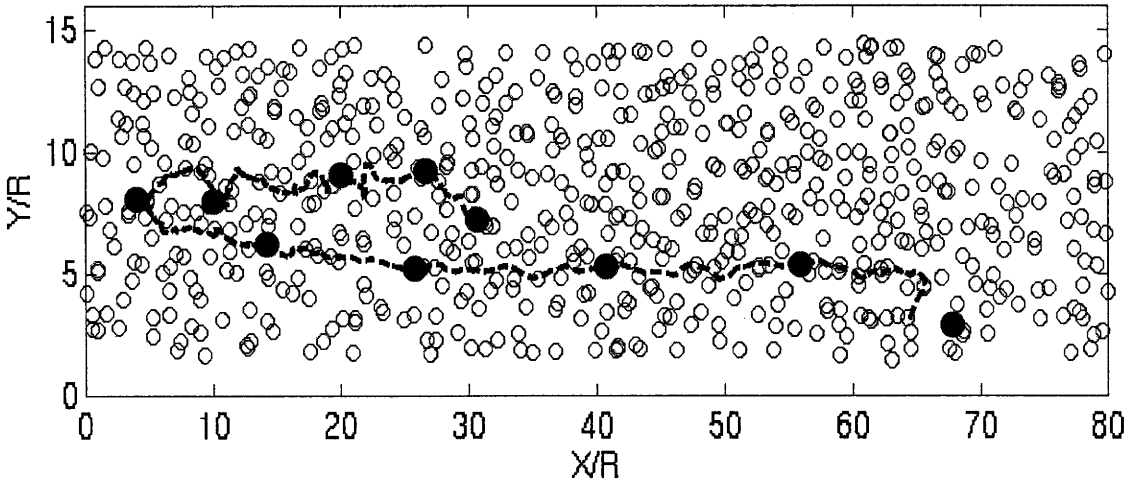

Figure 5.6 Trajectory trace of the intruder with size ratio ϕ=2.0 in the shear flow.

5.2 Mean Square Displacement and Diffusion Coefficient

In order to better understand the trajectory of intruders of various sizes, mean square displacement and diffusivity computations are carried out. The cases under consideration are depicted in Figures 5.3 – 5.5 for which $2U/H = 2/s^{-1}$ and $\nu = 0.4$. The mean square displacement is computed in the usual manner, i.e.,

$$\left\langle \Delta Y^2 \right\rangle = \frac{1}{N} \sum_{i=1}^{N} \left\langle \left[Y_i(t + \Delta t) - Y_i(t) \right]^2 \right\rangle \tag{5.1}$$

As expected, its value is very sensitive to the size of the intruder relative to the flow particles as is apparent in Figure 5.7. Within 5 seconds, the mean square displacement of the largest particle (f = 3.0) increases very rapidly and then flattens out after the intruder has entered the central trapping region.

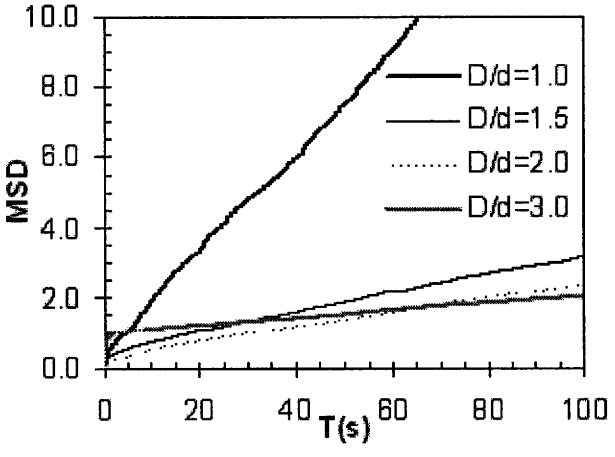

Figure 5.7 MSD of each species with different size ratio.

Because the slope in the limit as $t \to \infty$ is constant, it is possible to compute a diffusion coefficient using the Einstein relation which is expressed as the limiting slope of the mean square displacement versus time curve,

$$\left\langle |r(t) - r(0)|^2 \right\rangle = 6D\,t \tag{5.2}$$

In the equation (5.2), $\left\langle |r(t) - r(0)|^2 \right\rangle$ represents the mean square displacement of the particle and D is diffusion coefficient. These coefficients are shown in Figure 5.8 for different boundary velocities as a function of the relative intruder size.

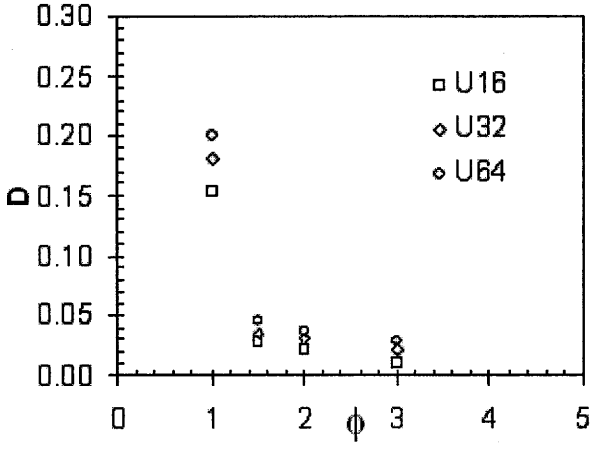

Figure 5.8 Diffusion coefficient of each species for different shear rates $2U/H = 2, 4, 8$ (s^{-1}).

Over the three shear rates tested ($2U/H$ = 2, 4, 8 s^{-1}), the results indicate that the motion of the largest intruder is far less diffusive than the tracer particles, with an order of magnitude difference. The effect of the shear rate is also apparent as larger values promote diffusivity.

5.3 Net Force and Velocity

One of the principal advantages of computer simulations is that it is possible to extract data on the particle level forces that are virtually impossible to directly access in experiments. One such quantity is the evolution of the net or resultant force on a particle

$$\mathbf{F}(t)_{net} := \frac{1}{N_c}\sum_{j=1}^{N_c}\mathbf{F}_j = \left(F_x(t)_{net}, F_y(t)_{net}, F_z(t)_{net}\right) \tag{5.3}$$

$$\left\langle F_y \right\rangle := \frac{1}{T}\sum_{t=t_1}^{t_2} F_y(t)_{net} \tag{5.4}$$

as depicted in Figure 5.9. These quantities are non-dimensionalized as follows,

$$\overline{\mathbf{F}} = \frac{\mathbf{F}_{net}}{\rho_p(\sigma^2{}_p \frac{U}{H})^2} \tag{5.5}$$

$$\overline{V} = \frac{V}{U} \tag{5.6}$$

where ρ_p is the density of particle, σ_p is diameter, U is the boundary velocity and H is the gap size. The force defined above will also be referred to as the diffusion force.

The results presented in Figure 5.10 correspond to the net *diffusion* force $\overline{\mathbf{F}}$ and velocity $\overline{V}$ of the intruder in the Y direction as function of time. The velocity trace in Figure 5.10b for $\phi = 2$ is quite different from that of Figure 5.10b for $\phi = 1$; the large intruder is clearly weighted towards positive values, while the tracer sphere velocities appear to be more balanced. Thus, during the time duration of 10s shown Figure 5.10b, the large sphere is moving in the positive Y direction away from the wall towards the center of the sheared region. The smaller magnitude of the velocity fluctuations of the intruder compared with the tracer is in accord with the intruder having a smaller diffusion coefficient (Figure 5.8).

This is accompanied by a net force history (Figure 5.10d) that has larger values in the positive Y direction, again indicative of the large intruder's motion away from the wall.

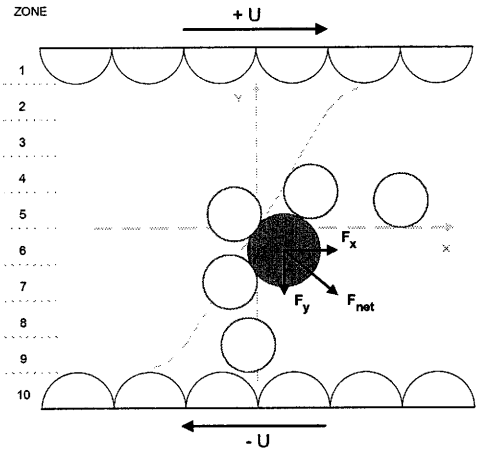

Figure 5.9 Diagram of the net force around the intruder.

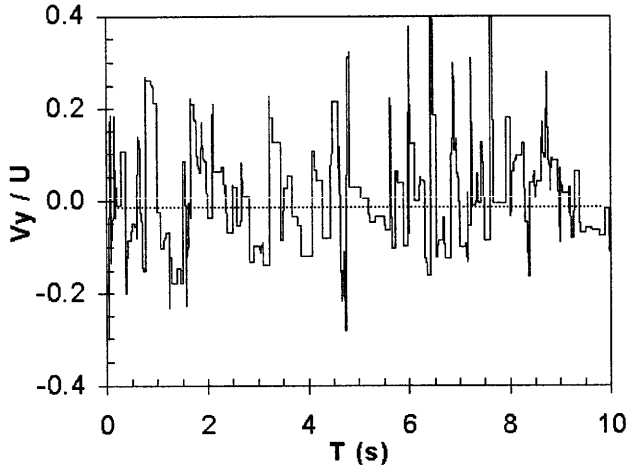

Figure 5.10a Velocity trace for an intruder with size ratio ϕ=1.0.

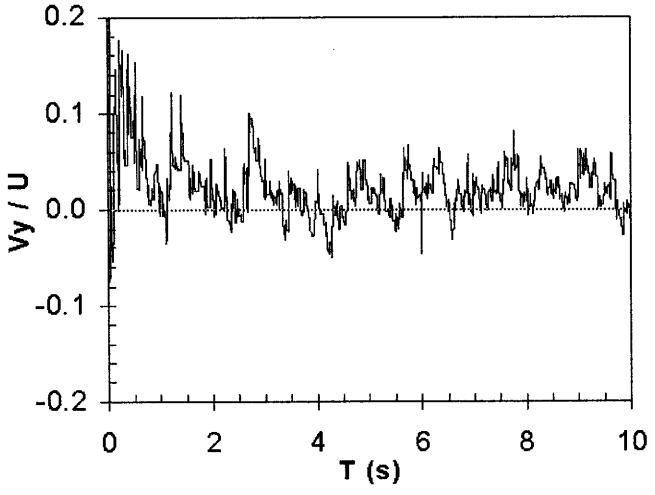

Figure 5.10b Velocity trace for intruder with size ratio ϕ=2.0.

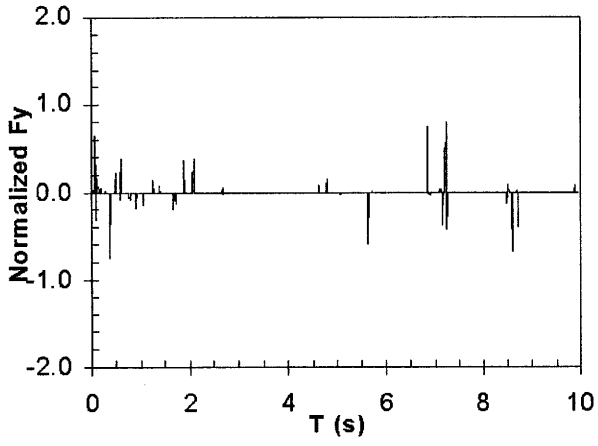

Figure 5.10c Net force history on an intruder with size ratio ϕ=1.0.

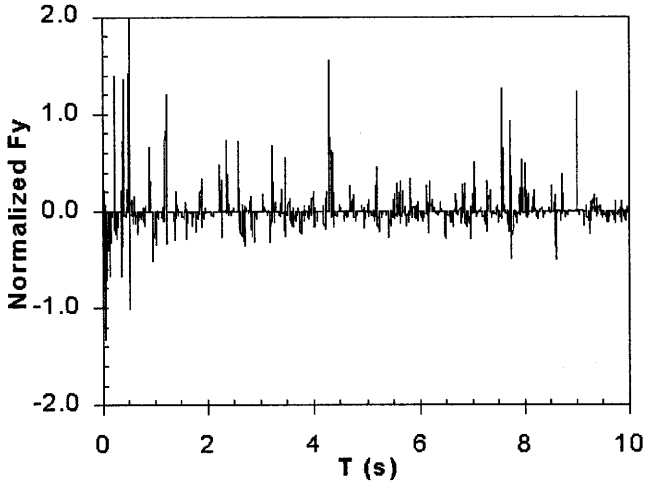

Figure 5.10d Net force history on an intruder with size ratio ϕ=2.0.

The results of the spectral and wavelet analyses of the secondary y-component of the secondary velocity field showed evidence of structures whose length scale (or wavelength) depended inversely on the shear rate (Figure 4). It is not clear if a correlation exists between this field and the motion of an intruder. However, it is likely that a tracer particle (that is, a typical flow particle) follows a trajectory that is in some manner associated with these structures.

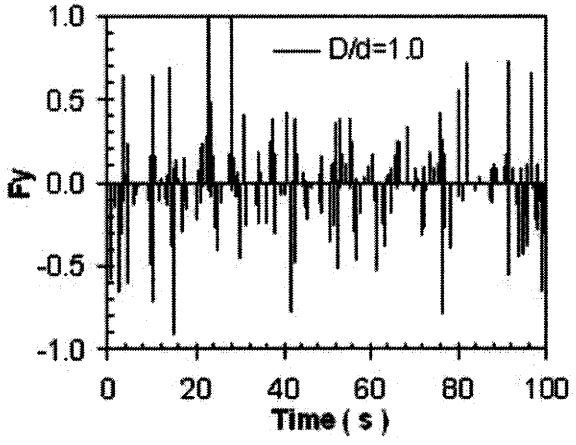

Figure 5.11a Net force F_y on a tracer particle (ϕ=1.0).

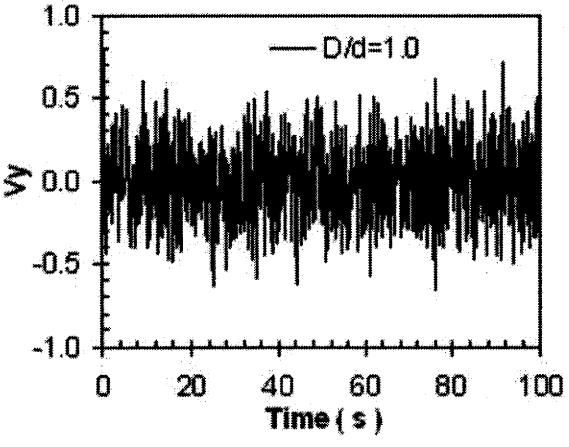

Figure 5.11b Velocity history for a tracer particle (ϕ = 1.0).

As indicated in Figures 5.10 c-d, there is a predominantly upward component of F_y on the intruder for the first 10 seconds of its motion. However, as this particle reaches the trapping region in the center of the shear flow, this net force become balanced between positive and negative values. (See Figure 5.11c).

A measure of the fluctuations in the velocity and net forces histories is given by the room mean square (RMS) values computed over the 100 second duration of the flow. F_y.

$_{RMS}$ and $V_{y\text{-}RMS}$ are normalized in the same manner as shown in equations (5.4) and (5.5), respectively.

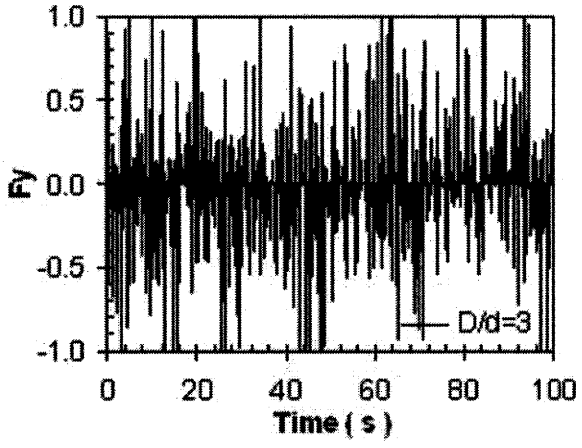

Figure 5.11c Net force history F_y on an tracer particle(ϕ=3.0).

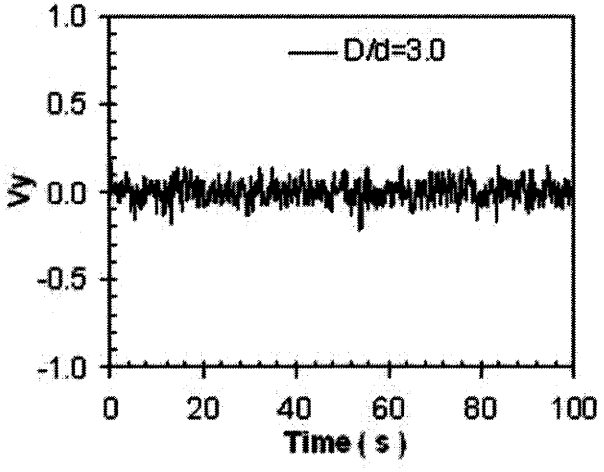

Figure 5.11d Velocity history for a tracer particle (ϕ=3.0).

Figure 5.12a reveals a linear relationship between size ratio ϕ and $F_{y\text{-}RMS}$ such that larger intruders experience greater fluctuations in the diffusion force in steady-state. However, $V_{y\text{-}RMS}$ decreases with the square of the size ratio ϕ (Figure 5.12b) within the tested range ($0.5 < \phi < 3$). This suggests that in the central trapping region, a more massive intruder suffers smaller velocity fluctuations because of the inability of the

lighter surrounding particles to cause it to undergo significant displacements. This interpretation is further corroborated by the diffusion results in Figure 5.8. It is conjectured that larger species in poly-disperse systems (such as in Figure 1.2) obey similar laws that keep them constrained to the low energy (granular temperature) region (in the center) of the flow.

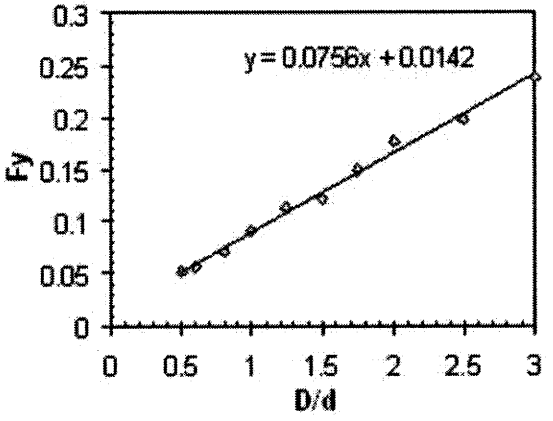

Figure 5.12a Effect of size ratio on RMS of $F_{y.}$

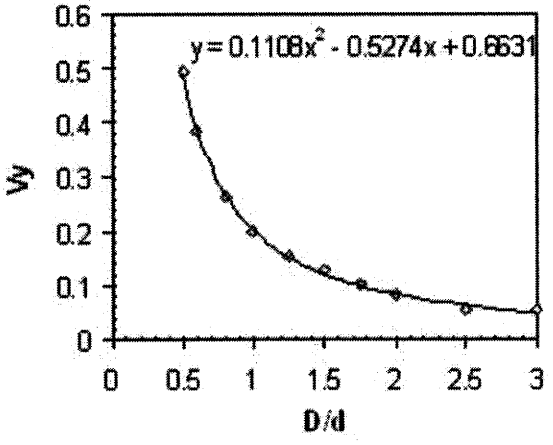

Figure 5.12b Effect of size ratio on $V_{y\text{-RMS.}}$

5.4 Size Ratio and Mass Ratio

In the simulations discussed above, all of the intruders were assigned the same material density so that they were more massive than the uniform flow particles. Therefore, the

behavior seen for the intruders is due to combined effects of size and mass. In order to examine which of the two may be more important on the dynamics, two different cases were designed. In the first, the size ratio was varied while keeping the mass ratio constant by suitably adjusting the intruder's material density. The second scenario kept the size of the intruder equal to that of the flow spheres while varying the mass ratio.

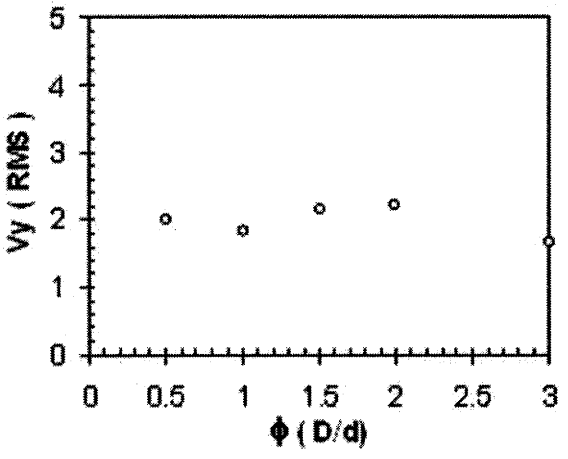

Figure 5.13a V_{yrms} with different size ratio.

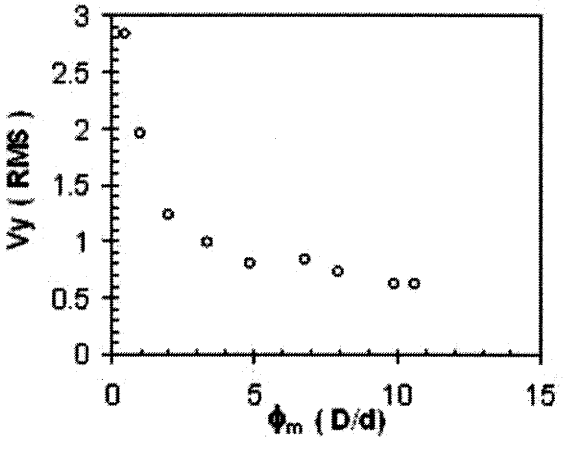

Figure 5.13b $V_{y\text{-}rms}$ versus mass ratio ϕ_m.

For the situation where the intruder size was equal to the flow spheres, results are presented in Figure 5.13b. The RMS value of V_y decreases with mass ratio ϕ_m, in agreement with the investigation of McElwaine [67]. Beyond ϕ_m = 5.0, the curves appears to flatten out. In contrast, the situation for fixed mass and varying size ϕ in Figure 5.13a shows little influence of ϕ on $V_{y\text{-}RMS}$. Consequently, these results suggest that the dominant factor affecting velocity fluctuations is the intruder mass.

5.5 Contact Number Analysis

The fact that the intruder tends to migrate away from the bumpy boundaries towards the low temperature region in the flow center implies that there is an effective force that acts.

This force is essentially the resultant of the all the nearest (contacting) neighbor interactions. Hence it is reasonable to examine in detail the nature of these contacts.

The contact or collision angle in the shearing (XY) plane is determined in each of the four quadrants as diagrammed in Figure 5.14: Quadrant **I** = 0 ° – 90 °, Quadrant **II** = 90 ° – 180 °, Quadrant **III** =180° – 270°, Quadrant **IV** = 270° – 360°. The collision-angle distribution $N(\theta)$ is defined as the number of collisions occurring in an interval $\Delta\theta$ divided by the total number of collisions that occur during the 200 seconds period of observation. The collision angle θ itself may fall into one of the four quadrants already defined, or, with low probability, on an axis. The circle is partitioned into 30 intervals so that $\Delta\theta$ = 12 °. The results of the time-averaged distributions for a tracer particle ϕ=1.0 and a large intruder ϕ=3.0 are shown in Figure 5.15.

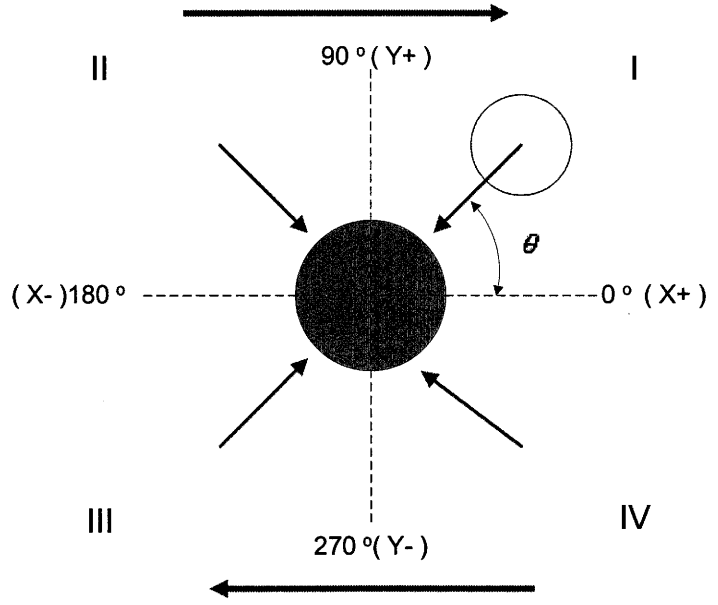

Figure 5.14 Diagram of collision angle (θ) in the XY plane.

The first observation from these plots is that the distribution in not uniform. In a boundary driven shear flow, the distribution is expected to be larger in quadrants II and IV, corresponding to collisions occurring more frequently in the upper left and lower right quadrants of the intruder particle. These findings are in agreement with the simulations of Campbell [17] and Karion [23].

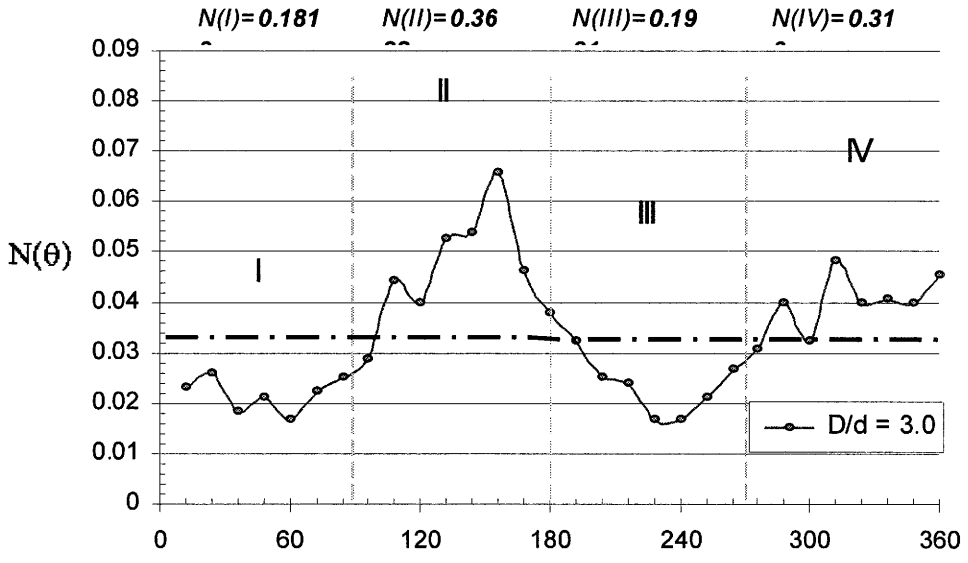

Figure 5.15a Collision angle distribution function for intruder with $\phi = 3.0$.

Furthermore, in order to correlate the motion of intruder with mean velocity profile, the shear gap has been partitioned into M strips parallel to the shearing direction. The time and spatial average of the number of contacts experienced by the intruder in each strip k is separated into two terms, i.e., contacts on the top half of the sphere for collisions in quadrants I and II, denoted by $T_{up}(k)$, and contacts on the lower half of the sphere for collisions in quadrants III and IV, denoted by $T_{low}(k)$. The index k ranges from 1 to M. In the investigation, M was between 10 to 20.

Let $N(\theta,k,t)$ designates the number of contacts at angle θ in strip k at time t. The cumulative number of contacts over $(t_2 - t_1)$ seconds $\langle N(\theta,k)\rangle$ as a function of θ in strip k is given by

$$\langle N(\theta,k)\rangle = \sum_{t=t_1}^{t_2} N(\theta,k,t),\ k=1,2,\ldots M \tag{5.7}$$

For the upper and lower halves of the sphere, the total number of contacts is computed by summing over the appropriate range of angles, i.e.,

$$\begin{aligned} N_{up}(k) &= \sum_{\theta=0}^{\pi} \langle N(\theta,k)\rangle \\ N_{low}(k) &= \sum_{\theta=\pi}^{2\pi} \langle N(\theta,k)\rangle \end{aligned},\quad k=1,2,\ldots,M \tag{5.8}$$

The deviations of the quantities in equation (5.8), denoted by $T_{up}(k)$ and $T_{low}(k)$, are computed by subtracting away the mean number of contacts (obtained by averaging over all of the strips). Thus,

$$\begin{aligned} T_{low}(k) &= N_{low}(k) - \frac{1}{M}\sum_{j=1}^{M} N_{low}(j) \\ T_{up}(k) &= N_{up}(k) - \frac{1}{M}\sum_{j=1}^{M} N_{up}(j) \end{aligned},\quad k=1,2,\ldots M \tag{5.9}$$

Depth profiles of T_{up} and T_{low} of a tracer (ϕ = 1.0) are presented in Figure 5.16a, where the ordinate axis represents the index of the strip from the bottom to the top along the shear gap, while the abscissa are the values of T_{up} and T_{low} defined by equation (5.9). For ϕ = 1.5, profiles were qualitatively similar to the tracer results, but quantitatively the distribution was narrower and more peaked at the center due to trapping of the intruder in the central flow region.

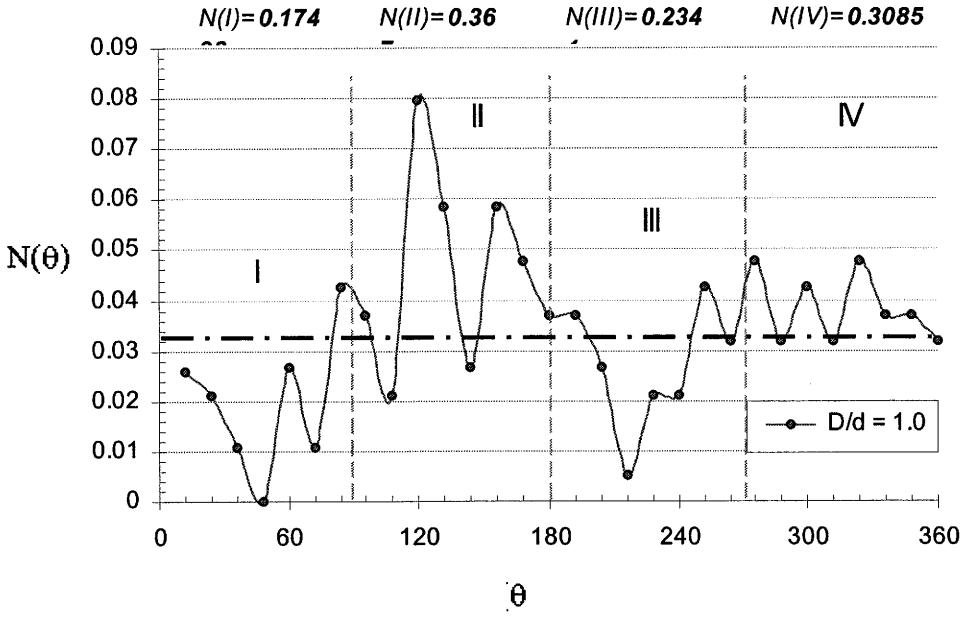

Figure 5.15b Collision angle distribution function for a tracer ($\phi = 1.0$); the mean of the function is shown as the dotted, horizontal line.

The difference between T_{up} and T_{low} (Figure 5.16) computed as $\Delta = 2(T_{up} - T_{low})/(T_{up} + T_{low})$, for the tracer particle, clearly shows that the net number of contacts on the lower half of the sphere when it is below the center line; conversely, the net number of contacts on the sphere's upper half is greater when it is above the center line. This unbalance results in a net force that pushes the tracer away from the moving boundaries toward the center. Results for an intruder ($\phi = 1.5$) is shown in Figure 5.17 that shows a greater unbalance, from which one infer a larger diffusion force. For much larger intruders, the computations only make sense for short time periods during which the particle is on its way to the trapping region. Accumulation of contact number statistics after it is "trapped" and averages subsequently computed distort the results so that the unbalance is smeared out.

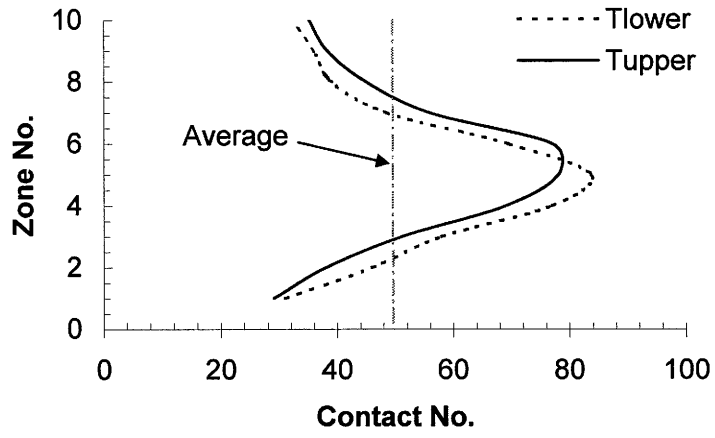

Figure 5.16a Depth profile of contact number T_{low} and T_{up} for a tracer particle (ϕ=1.0).

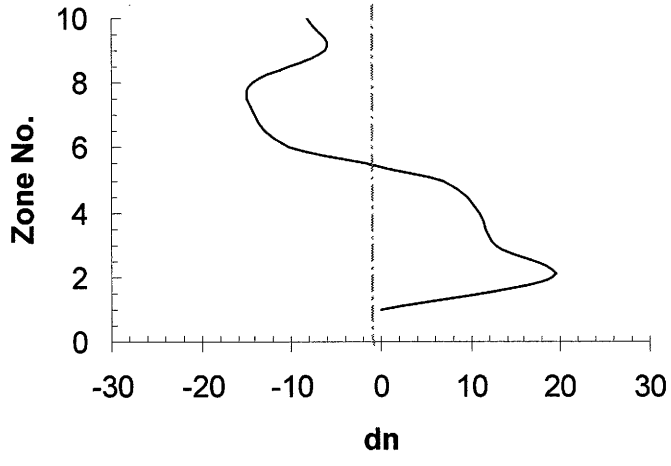

Figure 5.16b Depth profile of *dn* along the gap height for intruder with size ratio ϕ=1.0.

CHAPTER 6

MOTION OF INTRUDER IN GRAVITY FIELD

The previous chapter discussed the behavior of an intruder in a zero gravity, boundary-driven shear flow. In this situation, the particle was driven away from the "hotter" to the "colder" region of the flow in the center of the shear gap. In the current Chapter, DEM simulations of a sheared granular mixture under a gravitational field that acts in a direction perpendicular to the plane of shearing are presented. Results show that an intruder will rise against gravity to the surface. At the first stage, an intruder with different size ratio has been mixed with other regular flow particles in order to explain the role of gravity force on size segregation. Finally, all the big particles will migrate to the top surface of the shear cell and segregate from other flow particles. Experiments reported by Savage and Hutter [68] on binary mixtures revealed a similar phenomenon.

6.1 Brief Description of the Simulation System with Gravity

The simulation cell pictured in Figure 6.1 models a small slice of the experimental device used by Khosropour and Zirinsky [33], which consisted of two coaxial vertical cylinders. The inner cylinder rotates while the outer cylinder is stationary. The actual slice has an open top, periodic sidewalls perpendicular to the direction of shear (X), and two bumpy boundaries along the shear direction (Y). Each of these walls consists of spheres in a square configuration. In order to drive the particles within the cell, a constant velocity U in positive X-direction is imposed on the inner wall.

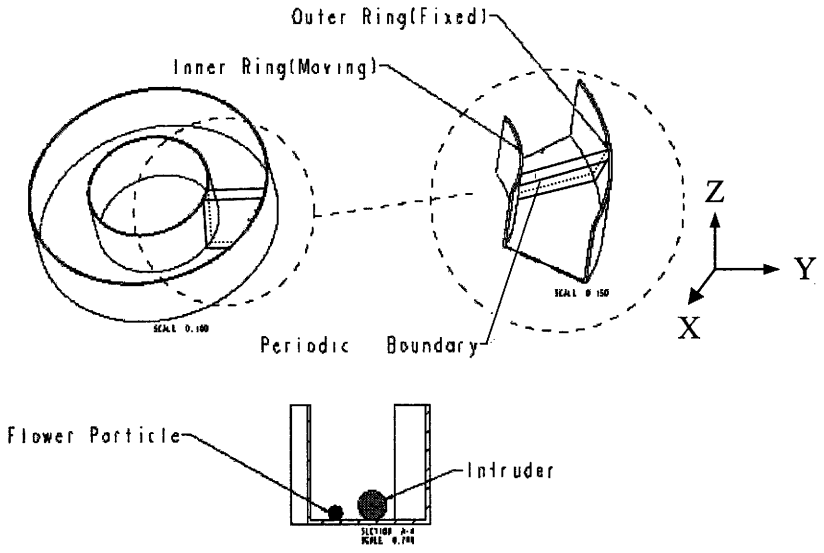

Figure 6.1 Diagram of simulation cell in gravitational field.

The gap between two bumpy walls is D =16cm wide, W = 16 cm thick (X direction) and is a height of H (=16cm) with spherical glass beads of diameter d =2 cm. Several seconds after initiation of the flow, the depth of the granular assembly experienced fluctuations between ½ to 1 cm as a consequence of Reynolds' dilatancy. A sufficient shear rates, a densely packed granular solid expands so that particle can flow.

The current study is principally focused on the segregation behavior of a single intruder particle differing in size from all the uniform particles that constitute the bulk material. In the simulation, the single intruder particle was assigned the bigger ratio compared with the regular flow particles. Thus, the intruder's mass is greater than the flow particles since it was given the same density. Initially, the intruder was placed on the floor of the computational cell. As will be shown, shearing caused it to follow an interesting trajectory that brought it to the surface. During the course of its motion, a vortex-like flow is present in the flow.

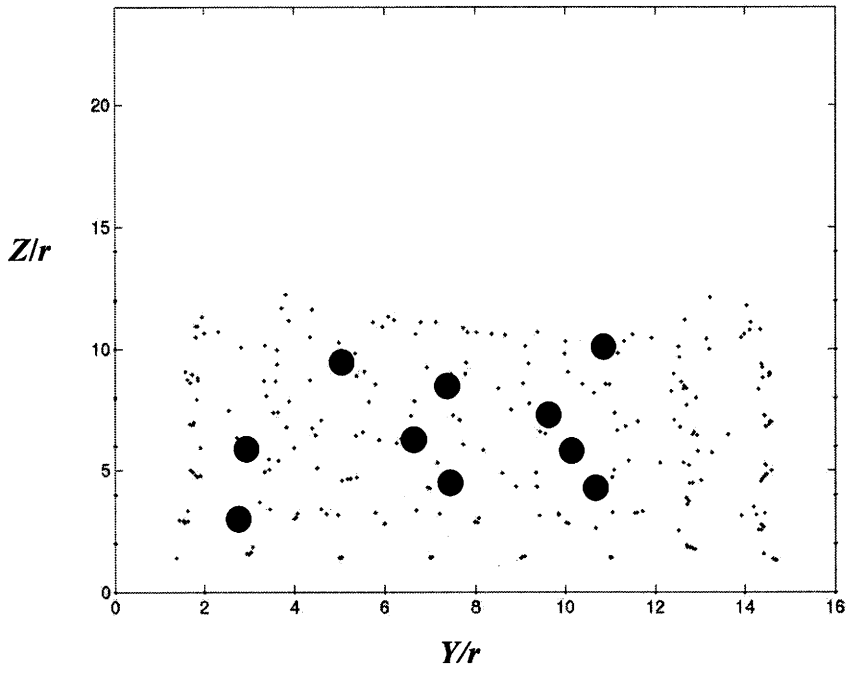

Figure 6.2a Initial distribution of the binary mixture with 10 larger intruders.

An important outcome of the study is that the large intruder particles undergo segregation that brings them to the surface where they remain upon continued shearing of the assembly. Figure 6.2a depicts of the locations of sphere centers projected onto the shearing plane, with ten large intruders exaggerated so that they can be easily seen. The configuration after 20 seconds of shearing at a rate U/D = 1/s in Figure 6.2b shows that all of the intruders are at the surface.

What is interesting is that while there is a velocity (and hence granular temperature) gradient across the cell, the large intruders migrate upward against gravity. So the prevailing motion is to the surface, although there is a secondary effect of the temperature gradient.

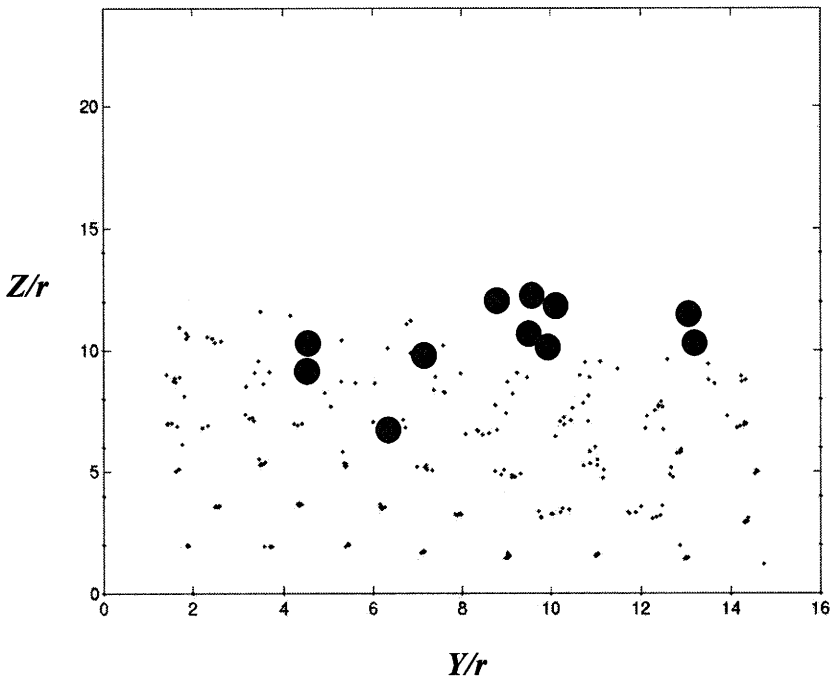

Figure 6.2b Snapshot taken at t = 20s showing a layer of large particles (ϕ = 2) on the flow surface. Shear rate (U/D) = 2 s^{-1}.

Recent experimental observations [24] and simulations [26] in binary systems, how demonstrated that the speed of migration to the surface depends significantly on the particle size ratio and shear rate. This dependency is also found in the simulations reported here. In order to demonstrate and quantify the effect of shear rate on migration, the flow is simplified by considering only a single intruder of ratio ϕ=2.0.

6.2 Migration of the Intruder Particle

Figure 6.3 displays the trajectory of the large intruder in the YZ plane, which is perpendicular to the shear direction. The velocity of the inner wall U is 32 cm/s which translates to a shear rate U/D = 2/s. After the first 5 seconds, flow particles tend to become aligned as can be seen from the projected sphere centers in the figure. The shear

induced by the moving inner wall produces velocity profiles along the coordinate directions that ultimately impinge on the movement of the intruder.

The migration of the intruder has a very clear trend where it steadily rises to the surface in a few seconds. During the entire process, its motion in the horizontal (Y direction) fluctuated only slightly, following the mean velocity field in the shear direction (X). After it reaching the top of the bed and getting free from the constraints of other flow particles, it remains on the top layer of the bed and is never re-entrained.

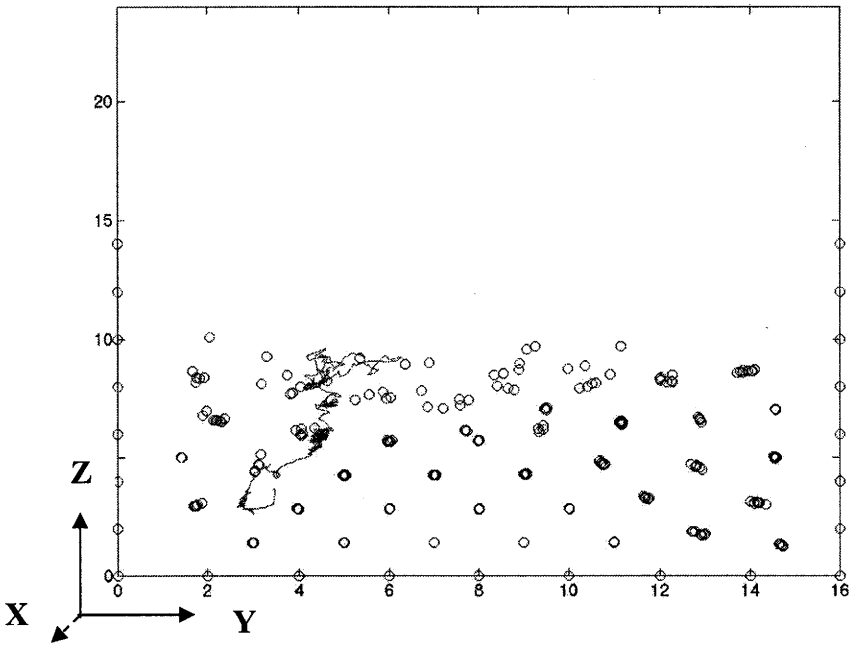

Figure 6.3 Trajectory of the intruder in the YZ plane. Gravity acts downward. (U=32 cm/s on the left wall, and the right wall is fixed; U/D = 2/s.

Figure 6.4 shows a comparison of simulation with the experimental results of Khosropour and Zirinsky [24] for the vertical displacement of the intruder particle whose diameter is twice that of the uniform flow spheres (ϕ = 2.0). Rotation frequencies f (Hz) reported in the experiments are converted to the velocities of the inner walls (radius R =

2.85 cm) chosen for the simulations. Table 6.1 lists the parameters and resulting shear rates ranging from 1 to 2.81 s^{-1}.

Table 6.1 Relation Between Rotation Frequency, Linear Velocity, and Shear Rate

Rotation Frequency f (*Hz*)	Linear Velocity $U = 2\pi Rf$ R=2.85cm (cm/s) R - the radius of inner ring	Shear rate $\dot{\varepsilon} = U / D$ (D= 16 cm)
0.89	15.929	1.0
1	17.898	1.12
1.6	28.637	1.79
2.1	37.586	2.35
2.5	45	2.81

The experiments indicate a faster rate of ascent when the frequency is higher, a trend that is also reproduced in the simulations. The intruder of the simulations reached the surface more quickly that what occurred in the experiments. The agreement with the physical data is not very good, which may be a consequence of the selection of particle properties and the fact the centrifugal forces were not included in the simulation. Another factor was the lack of information on the roughness of the walls and particle friction coefficient used in the experiments.

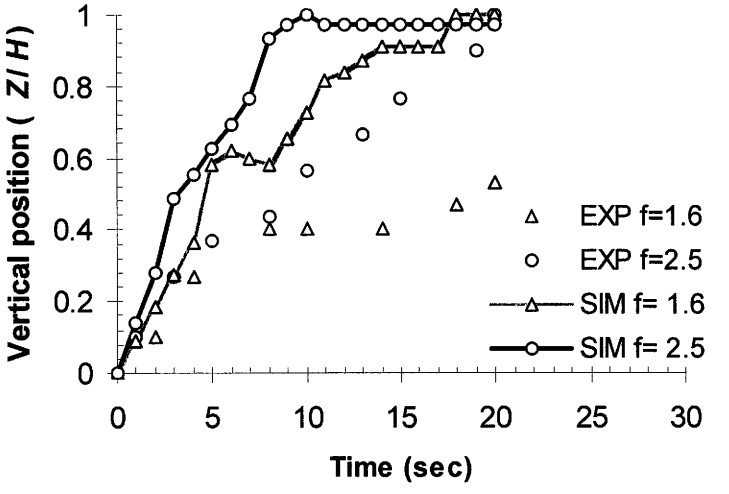

Figure 6.4 Evolution of normalized position Z/H at f = 1.6 and 2.5 from the simulations and experimental data [24].

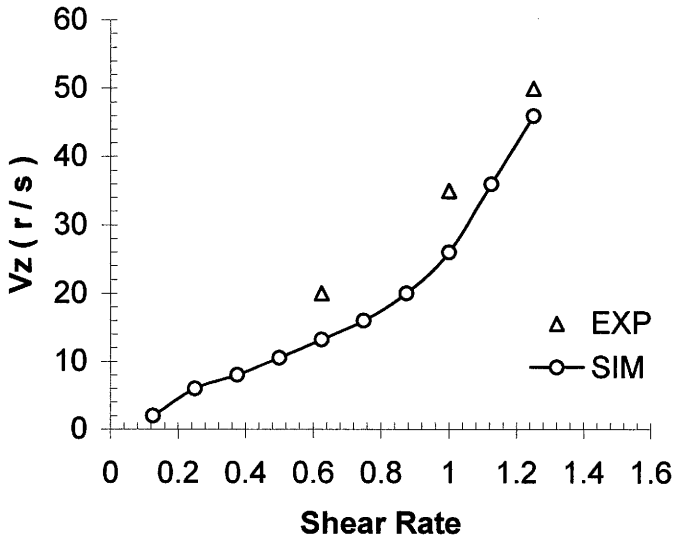

Figure 6.5 Average vertical speed V_z of the intruder (ϕ=2.0) versus shear rate U/D for the experiments [24] and simulation.

A comparison of the mean ascent speeds of the intruder with the experimental data [24] is shown in Figure 6.5. The mean values were obtained by dividing distances to the surface by the times required for the intruder to reach the surface. The agreement is actually quite good for the range of shear rates presented in the figure.

6.3 Vortex Pattern on Velocity Field

It is possible that bulk convection within the shear system is, in part, responsible for the intruder's behavior, as has been demonstrated in vertically vibrated granular beds [9], where the flow depended on vibration amplitude and acceleration. In the current study, a complex convective field in the time averaged, secondary velocity field was discovered as depicted in Figure 6.6. This field was obtained by subtracting the mean field velocity along the Y direction. Here the shear rate U/D = 1/s. The interesting pattern appears near the moving wall (on the right side of the figure).

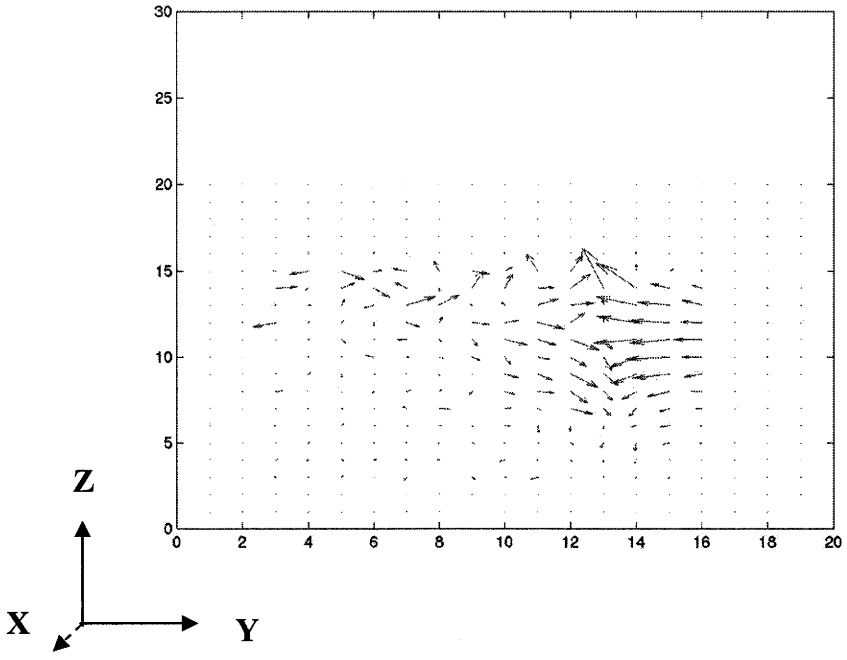

Figure 6.6 Secondary flow pattern on the velocity field of YZ plane (U/D = 1/s). In the image, the moving wall is on the right hand side.

CHAPTER 7

SUMMARY AND CONCLUSIONS

7.1 Research Summary

An investigation of a Couette granular flow in a zero gravity field has been carried out using discrete element simulations to model the behavior of intruders having different properties. The general features of this boundary driven flow were quantified through computations of fully-developed profiles of granular temperature, pressure, velocity and solids fraction. A principal finding in this investigation is the tendency of the intruder to move towards the colder (or less energetic) regions of the flow, away from the moving walls. This simulated trends reproduced the phenomenon observed by Bridgwater and Stephens [30] in their annular shear cell experiments. In contrast, a tracer particle (or typical flow particle) did not get trapped, but visited the entire accessible shear gap with a trajectory characteristic of persistent fractal Brownian motion. The time T_c required for the intruder to reach the surface decreased with size ratio ϕ as $T_c = T_0(U/H)e^{-k(\phi-1)}$ and it also appeared to scale with the shear rate as exemplified by the dependence of T_0 on U/H.

Computations of the component of the net force (also called "diffusion force") on the intruder in the direction perpendicular to the shear showed that it was directed away from the walls and towards the center. This result was substantiated by calculations indicating that the half of the intruder closest to the bumpy walls experienced more collisions (or contacts) on the average than its other half as it advanced to the center of the sheared region. Furthermore, the amplitudes of fluctuations in the net force and velocity depended on the size ratio. At a fixed bulk solids fraction, the root mean square

value of net force on an intruder increases with particle size ratio, while the RMS value of velocity has the reverse trend.

As the relative size of the intruder grew so that it became more massive, its velocity distribution became increasingly narrow and peaked, in qualitative agreement with the Maxwell-Boltzman distribution for molecular particles. The long time slope of the Y-component of the intruder's mean square displacement yielded its Y-diffusivity. As the relative size of the intruder increased, its motion became less diffusive.

A spectral analysis of a secondary velocity field (obtained by subtracting out the mean flow velocity profile) across the simulation cell revealed a pattern having a fixed wavelength, whose value depends on shear rate. A further examination of the field via wavelets supports this finding. It is conjectured that the intruder's trajectory is affected by the cyclic pattern in the secondary velocity. There was evidence that as the shear is made larger, the pattern becomes less pronounced and decays. This is probably due to the reduction in the effectiveness of the bumpy walls to induce flow across increasingly wider shear gaps.

Simulations were carried out to investigate a system in which gravity acts perpendicular to the direction of the shear, such as that used in the experiments reported by Khosropour and Zirinsky [33]. They found that all large (and more massive) particles ascended to the surface of the medium under the effects of the gravity field and boundary driven shearing. In the simulations, the geometry of the experimental system was approximated by subscribing a velocity U to the inner wall while keeping the outer wall fixed. Because the cell was planar (in contrast to the physical experiments), body forces produced by centrifugal acceleration were ignored. Computations obtained from the

simulation data revealed that a single large sphere rose up in the shearing medium at different speeds depending on the size ratio. In addition, a steady convection-like structure was found near the inner moving boundary, which is believed to play a role in driving the upward motion of the intruder.

7.2 Suggested Future Research Topics

The simulation work presented in this study provided several intuitive ideas and directions for further studies. These include:

(1) Examination of the role of wall roughness and boundary properties on the formation of convective patterns in the flow.

(2) A detailed parameter study to examine the affects of particle properties (i.e., friction coefficient and elasticity).

(3) Extend the study of the effects of intruder density over a wider range.

(4) Behavior of systems having continuous size distributions.

(5) Incorporation of the interstitial fluids (such as air) into simulation.

APPENDIX A

POST PROCESSING CODE IN MATLAB

Following section will attach some of the post processing programs which were compiled in MATLAB, where the output data from simulations has been investigated and plot.

A.1 Histogram

```
clear;
%-------------------------------------------------------------------------
%-------base on the data of /run/mass1-5
%-------Four chart will plot the Y, Histor(Y), Fy, Vy of intruder %----
%-------particle.
%-------------------------------------------------------------------------

%-------distribution bin No.---------------------------
Ndis=100;

%-------load input data section2------------------------
load /afs/cad/research/a/2/run/mass1/zzbig1;
load /afs/cad/research/a/2/run/mass1/zzforce1;
load /afs/cad/research/a/2/run/mass1/zzvel1;
Displace =zzbig1;
Force =zzforce1;
Vel =zzvel1;

%-------config simulation cell height & low limit ----------------
H=16;
%------same size,different mass-----------------------------------
limit=1.414;            %--Fi=1.0
%-----------------------------------------------------------------

%limit=2.06;            %--Fi=1.5
%limit=2.646;           %--Fi=2.0
%limit=3.742;           %--Fi=3.0
```

```
%-------transfer data to time, x,y, fx, fy, vx, vy----------------
t=Displace(:,1);
x=Displace(:,2);
y=(Displace(:,3)-limit)/(H-2*limit);      %normilized y coordination
z=Displace(:,4);

fx=Force(:,2);
fy=Force(:,3);
fz=Force(:,4);

vx=Vel(:,2);
vy=Vel(:,3);
vz=Vel(:,4);

%--------calculate RMS of Displace/Force/Velocity------------------
RMSy=0;
RMSfy=0;
RMSvy=0;
NNN=0;
for i=1:length(t)
      RMSy=RMSy+(y(i))^2;
      if abs(fy(i))>0          %----each collision
            RMSfy=RMSfy+(fy(i))^2;
            NNN=NNN+1;
      end
      RMSvy=RMSvy+(vy(i))^2;
end
RMSy=sqrt(RMSy/length(t));
RMSfy=sqrt(RMSfy/NNN);
RMSvy=sqrt(RMSvy/length(t));

%--------plot y location-------------------
subplot(2,2,1);
plot(t,y);
axis([0 200 0 1]);
hold on;
xlabel('times');
```

```
ylabel('Yposition');
str=sprintf('RMSy=%6.2f',RMSy);
title(str);

%--------plot y historgram--------------------
subplot(2,2,2);
hist(y,100);
xlabel('bins');
ylabel('Frequency');
axis([0 1 0 200]);
hold on;

%--------plot fy---------------------------------
subplot(2,2,3);
plot(t,fy);
hold on;
xlabel('times');
ylabel('Fy');
str=sprintf('RMSFy=%6.2f',RMSfy);
title(str);

%--------plot vy---------------------------------
subplot(2,2,4);
plot(t,vy);
hold on;
xlabel('times');
ylabel('Vy');
str=sprintf('RMSVy=%6.2f',RMSvy);
title(str);
histvy=hist(vy,Ndis);
maxvy=max(vy);
minvy=min(vy);

for i=1:Ndis
      histx(i)=minvy+(i/Ndis)*(maxvy-minvy);
end

save histvy.dat histvy -ascii;
```

```
save histx.dat histx -ascii;
```

A.2 Autocorrelation and FFT Analysis

```
%-------------------------------------------------------------------------
%-------addauto128.m                                                    -----
%-------use y-vel in each 10 seconds output file: p128z20---p128z150
%-------get the appended curve in 150 seconds                           -----
%-------get the autocoralation and FFT analysis                         -----
%-------output :  1.    autocoralation in 20-150 s                     -----
%-------          2.    FFT in 20-150s                                 -----
%-------------------------------------------------------------------------

%-------------section 1---------------------------------
%-------load input data section1------------------------
clear;

load /afs/cad/research/a/2/matlabcode/intruder/zexp18D/m128/p128z20;
P2=p128z20;
P=P2;
Plength=length(P);

load /afs/cad/research/a/2/matlabcode/intruder/zexp18D/m128/p128z30;
P3=p128z30;
for i=1:length(P3)
      P(Plength+i)=P3(i);
end
Plength=length(P);

load /afs/cad/research/a/2/matlabcode/intruder/zexp18D/m128/p128z40;
P4=p128z40;
for i=1:length(P4)
      P(Plength+i)=P4(i);
end
Plength=length(P);

load /afs/cad/research/a/2/matlabcode/intruder/zexp18D/m128/p128z50;
```

```
P5=p128z50;
for i=1:length(P5)
      P(Plength+i)=P5(i);
end
Plength=length(P);

load /afs/cad/research/a/2/matlabcode/intruder/zexp18D/m128/p128z60;
P6=p128z60;
for i=1:length(P6)
      P(Plength+i)=P6(i);
end
Plength=length(P);

load /afs/cad/research/a/2/matlabcode/intruder/zexp18D/m128/p128z70;
P7=p128z70;
for i=1:length(P7)
      P(Plength+i)=P7(i);
end
Plength=length(P);

load /afs/cad/research/a/2/matlabcode/intruder/zexp18D/m128/p128z80;
P8=p128z80;
for i=1:length(P8)
      P(Plength+i)=P8(i);
end
Plength=length(P);

load /afs/cad/research/a/2/matlabcode/intruder/zexp18D/m128/p128z90;
P9=p128z90;
for i=1:length(P9)
      P(Plength+i)=P9(i);
end
Plength=length(P);

load /afs/cad/research/a/2/matlabcode/intruder/zexp18D/m128/p128z100;
P10=p128z100;
for i=1:length(P10)
      P(Plength+i)=P10(i);
```

```
end
Plength=length(P);

load /afs/cad/research/a/2/matlabcode/intruder/zexp18D/m128/p128z110;
P11=p128z110;
for i=1:length(P11)
      P(Plength+i)=P11(i);
end
Plength=length(P);

load /afs/cad/research/a/2/matlabcode/intruder/zexp18D/m128/p128z120;
P12=p128z120;
for i=1:length(P12)
      P(Plength+i)=P12(i);
end
Plength=length(P);

load /afs/cad/research/a/2/matlabcode/intruder/zexp18D/m128/p128z130;
P13=p128z130;
for i=1:length(P13)
      P(Plength+i)=P13(i);
end
Plength=length(P);

load /afs/cad/research/a/2/matlabcode/intruder/zexp18D/m128/p128z140;
P14=p128z140;
for i=1:length(P14)
      P(Plength+i)=P14(i);
end
Plength=length(P);

load /afs/cad/research/a/2/matlabcode/intruder/zexp18D/m128/p128z150;
P15=p128z150;
for i=1:length(P15)
      P(Plength+i)=P15(i);
end
Plength=length(P);
```

```
a1=xcorr(P,P);
a1=fftshift(a1);
halflength=ceil(0.5*length(a1));
for i=1:halflength
      a(i)=a1(i);
end

subplot(2,1,1)
plot(P,'r');
hold on;
%  axis([0 150 0 20000]);hold on;
xlabel('Frames (0.5s)');
ylabel('Wavelength (x/D)');

%---------FFT analysis-----------------------/
subplot(2,1,2);
v= fft(P);
v(1)=[]
set (gca,'ytick',[],'xtick',[]);
n=length(v);
power =abs(v(1:ceil(n/2))).^2;
nyquist=1/2;
freq=(1:ceil(n/2))/(n/2)*nyquist;
period=1./freq;
plot(period,power);hold on;
axis([0  60 0 1.5*max(power)]);

index=find(power==max(power));
mainPeriodStr1=num2str(power(index));
mainPeriodStr2=num2str(period(index));
text(period(index)+0.2*period(index),power(index), ...
[' power=',mainPeriodStr1,'
period=',mainPeriodStr2],'EraseMode','none');
hold on;

ylabel('power');
xlabel('period ( D / cycle )');
%title('periodogram / Period')
```

A.3 Velocity Field in Depth Direction

```
%-------------------------------------------------------------------------
%---------checkvectionY.m                                                -----
%---------check the average Y-velocity in each zone along gap height
%---------input  :      zposition, zvel;                                  -----
%---------output : 1.   sum of all the Vy in each
%---------              Yzone(sumVyP/zone,sumVyN/zone)                    -----
%---------         2.   sum of the total No in each Y
%---------              zone(sumNoP/zone,sumNoN/zone)                     -----
%---------         3.   average Vel for each particle in each Y
%---------              zone(sumVyP/sumNoP,sumVyN/sumNoN))                -----
%-------------------------------------------------------------------------

clear;
load /afs/cad/research/a/2/data/exp18D/05/zposition;  %location file
load /afs/cad/research/a/2/data/exp18D/05/zvel;       %velocity file
PP=zposition;
VV=zvel;
framen=200;              %--end number of the frames
startframe=100;          %--start number of the frames
nu=484;                  %--Total number of the particles
bnu=192;                 %--total number of boundary particles
U=16;                    %--boundary velocity
checkzone=36;            %--special zone no. in radial(Y) dir need to be
check
zone=42;                 %--Total zone No
H=16;                    %--gap width
PI=3.1415;

K=0;
Rbdry=1.0;               %--the Ridus ratio of the boundary particle
Rflow=1.0;               %--the Ridus ratio of the flow particle
Rlimit=sqrt((Rbdry+Rflow)^2-2*Rbdry^2);

for j=1:zone+1
      sumVyP(j)=0;
      sumVyN(j)=0;
```

```
        sumNoP(j)=0;
        sumNoN(j)=0;
        zoneNumber(j)=j;
end

kk=1;
z = PP(:,4); y = PP(:,3); x=PP(:,2);            %--X,Y,Z coordination
vz = VV(:,4); vy =VV(:,3); vx=VV(:,2);          %--VX,VY,VZ velocity

for P = startframe:framen,     %--use 200 to reach the steady state
   zoneYNo=0;                  %--initilization
   index1=(P-1)*nu+2;          %--start index of flow particle except
                                  the intruder
   index2=index1+nu-bnu-1;     %--end index of flow particle
   X =x(index1:index2);
   Z =z(index1:index2);
   Y =y(index1:index2);
   VX = vx(index1:index2);
   VZ = vz(index1:index2);
   VY = vy(index1:index2);

   for k=1:length(Z)           %---find the Y zone No. for each particle
      zoneYNo=ceil(zone*(Y(k)-Rlimit)/(H-2*Rlimit))+1;
      for L=1:zone+1
            if (zoneYNo==L)    %--r=(checkzone/zone)*H
                  if VY(k)>0
                        sumVyP(L)=sumVyP(L)+VY(k);
                        sumNoP(L)=sumNoP(L)+1;
                  else
                        sumVyN(L)=sumVyN(L)+VY(k);
                        sumNoN(L)=sumNoN(L)+1;
%--spatial accumulate the Vx in each y zone
                  end
            end
      end
  end

end
```

```
%------plot section----------------------------
 subplot(3,1,1);
 plot(sumVyP,zoneNumber,'r');hold on;
 plot(abs(sumVyN),zoneNumber,'b');hold on;
 axis([0 1.5*max(sumVyP) 0 zone+5]);
 subplot(3,1,2);
 plot(sumNoP,zoneNumber,'r');hold on;
 plot(sumNoN,zoneNumber,'b');
 axis([0 1.5*max(sumNoP) 0 zone+5]);
 subplot(3,1,3);
 for i=1:zone+1
 aveP(i)=sumVyP(i)/sumNoP(i);
 aveN(i)=abs(sumVyN(i))/sumNoN(i);
 end
 plot(aveP,zoneNumber,'r');hold on;
 plot(aveN,zoneNumber,'b');
 axis([0 1.5*max(aveP) 0 zone+5]);
 hold off;
```

A.4 Wavelet Analysis

```
%---wave1.m--------
%---wavelet analysis with a1 to a5 and d1 to d5-----------
load /afs/cad/research/a/2/matlabcode/intruder/zexp18D/m128/p128z130;
s=p128z130;
w='db3';
[c,l]=wavedec(s,5,w);

for i=1:5
      A(i,:)=wrcoef('a',c,l,w,i);
      D(i,:)=wrcoef('d',c,l,w,i);
end

head=5;
```

```
tt=1+head:length(s)-head
subplot(6,2,1); plot(tt,s(tt),'r');
title('Orig. Signal & a1 to a5');
subplot(6,2,2);plot(tt, s(tt),'r');
title('Orig. Signal & d1 to d5');
for i=1:5,
      subplot(6,2,2*i+1); plot(tt,A(5-i+1,tt),'b');
      subplot(6,2,2*2+2); plot(tt,D(5-i+1,tt),'g');
end
```

A.5 2D Mean Packing Density

```
clear;
load /afs/cad/research/a/2/testdata/fmub/09/zposition;   %location file
load /afs/cad/research/a/2/testdata/fmub/09/zvel;        %velocity file
PP=zposition;
VV=zvel;
framen=395;              %total number of the frames
startframe=200;
nu=484;                  %Total number of the particles
bnu=192;                 %total number of boundary particles
U=36;                    %boundary velocity
zone=42;                 %Total zone No
H=16;                    %gap width
PI=3.1415;

K=0;
Rbdry=1.0;               %--the Ridus ratio of the boundary particle
Rflow=1.0;               %--the Ridus ratio of the flow particle
Rlimit=sqrt((Rbdry+Rflow)^2-2*Rbdry^2);

for i=1:zone+1
      sumVxy1(i)=0;
      sumVxy1No(i)=0;
      sumNoTotal(i)=0;
```

```
end

z = PP(:,4); y = PP(:,3); x=PP(:,2);            %--X,Y,Z coordination
vz = VV(:,4); vy =VV(:,3); vx=VV(:,2);          %--VX,VY,VZ velocity

for P = startframe:framen,          %use 200 to reach the steady state
   zoneYNo=0;                       %--initilization
   for i=1:zone+1
      sumVx(i)=0;
      sumNo(i)=0;
   end

   index1=(P-1)*nu+1;               %--start index of flow particle
   index2=index1+nu-bnu-1;          %--end index of flow particle
   X =x(index1:index2);
   Z =z(index1:index2);
   Y =y(index1:index2);
   VX = vx(index1:index2);
   VZ = vz(index1:index2);
   VY = vy(index1:index2);
   MaxZ=max(Z);

   for k=1:length(Z)          %---find the Y zone No. for each particle
      zoneYNo=ceil(zone*(Y(k)-Rlimit)/(H-2*Rlimit))+1;
      if  (zoneYNo<=zone+1)
                  sumVx(zoneYNo)=sumVx(zoneYNo)+VX(k);
%--spatial accumulate the Vx in each y zone
                  sumNo(zoneYNo)=sumNo(zoneYNo)+1;
%--spatial accumulate the total particle no. in each zone
      end
  end

   for i=1:zone+1
      if sumNo(i)>0
            sumNoTotal(i)=sumNoTotal(i)+sumNo(i);
%--time accumulation of particle center
            sumVxy(i)=sumVx(i)/sumNo(i);
%--average velocity of each particle in x within each y zone
```

```
            sumVxy1(i)=sumVxy1(i)+sumVxy(i);
%--time accumulation of Vx for each y zone
            sumVxy1No(i)=sumVxy1No(i)+1;
%--time accumulation of No.for each y zone
      else
            sumVxy(i)=0;
            sumVxy1(i)=sumVxy1(i)+sumVxy(i);
      end

  end

end

%------average value in time span-------------
for i=1:zone+1
      yindex(i)=i;
      sum1(i)=sumVxy1(i)/(U*sumVxy1No(i));
end

%------plot section-----------------------------
 subplot(3,1,1);
 plot(yindex,sum1,'ro');hold on;
 plot(yindex,sum1);
 axis([0 40 0 1]);
 subplot(3,1,2);
 plot(yindex,sumNoTotal/(framen-startframe));
 axis([0 40 0 30]);
 subplot(3,1,3);
 TotalVol=(H-Rlimit)*MaxZ*16/(zone+1);

%---total volumn of each zone
 for i=1:zone+1
      TotalballVol(i)=(3/4)*PI*(Rflow)^3*sumNoTotal(i);
%---Total volumn of all particles in each zone
      Rate(i)=TotalballVol(i)/(TotalVol*(framen-startframe));
 end

 plot(yindex,Rate);
```

```
axis([0 40 0 1]);
```

A.6 Mean Velocity Profile

```
clear;
load /afs/cad/research/a/2/testdata/fmub/09/zposition;   %location file
load /afs/cad/research/a/2/testdata/fmub/09/zvel;        %velocity file
PP=zposition;
VV=zvel;
framen=395;        %total number of the frames
nu=484;            %Total number of the particles

bnu=192;           %total number of boundary particles
U=36;              %boundary velocity
zone=40;           %Total zone No
H=16;              %gap width

K=0;
Rbdry=1.0;         %--the Ridus ratio of the boundary particle
Rflow=1.0;         %--the Ridus ratio of the flow particle
Rlimit=sqrt((Rbdry+Rflow)^2-2*Rbdry^2);

for i=1:zone+1
      sumVxy1(i)=0;
      sumVxy1No(i)=0;
end

z = PP(:,4); y = PP(:,3); x=PP(:,2);          %--X,Y,Z coordination
vz = VV(:,4); vy =VV(:,3); vx=VV(:,2);        %--VX,VY,VZ velocity

for P = 200:framen,          %use 200 to reach the steady state
   zoneYNo=0;                %--initilization
   for i=1:zone+1
      sumVx(i)=0;
      sumNo(i)=0;
   end
   index1=(P-1)*nu+1;        %--start index of flow particle
   index2=index1+nu-bnu-1;   %--end index of flow particle
   X =x(index1:index2);
```

```
   Z =z(index1:index2);
   Y =y(index1:index2);
   VX = vx(index1:index2);
   VZ = vz(index1:index2);
   VY = vy(index1:index2);

   for k=1:length(Z)          %---find the Y zone No. for each particle
      zoneYNo=ceil(zone*(Y(k)-Rlimit)/(H-2*Rlimit))+1;
      if  (zoneYNo<=zone+1)
                  sumVx(zoneYNo)=sumVx(zoneYNo)+VX(k);
%--spatial accumulate the Vx in each y zone
                  sumNo(zoneYNo)=sumNo(zoneYNo)+1;
%--spatial accumulate the total particle no. in each zone
      end
  end

   for i=1:zone+1
      if sumNo(i)>0
            sumVxy(i)=sumVx(i)/sumNo(i);
%--average velocity of each particle in x within each y zone
            sumVxy1(i)=sumVxy1(i)+sumVxy(i);
%--time accumulation of Vx for each y zone
            sumVxy1No(i)=sumVxy1No(i)+1;
%--time accumulation of No.for each y zone
      else
            sumVxy(i)=0;
            sumVxy1(i)=sumVxy1(i)+sumVxy(i);
      end
  end
end

%------average value in time span-------------
for i=1:zone+1
      yindex(i)=i;
      sum1(i)=sumVxy1(i)/(U*sumVxy1No(i));
end

%------plot section---------------------------
```

```
subplot(2,1,1);
plot(yindex,sum1,'ro');hold on;
plot(yindex,sum1);
axis([0 50 0 1]);
subplot(2,1,2);
plot(yindex,log(sum1));
axis([0 50 0 1]);
```

A.7 2D Plot of the Intruder Particle

```
%-------------------------------------------------------------------------
%------animation code to see the motion of the intruder paticle in
%------modified couette flow field with gravity and boundary at z=zero
%-------------------------------------------------------------------------
clear;
load /afs/cad/research/a/2/data/exp18D/10big/zposition;    %--load file
PP=zposition;
framen=400;              %--frames number
nu=484;                  %--Total particles number
big=1;                   %--index of the big particles number

No=PP(:,1);x=PP(:,2);y = PP(:,3); z = PP(:,4);    %---z-x coordination
 for P = 1:framen,
   index=(P-1)*nu;
   X1(P)=x(index+big);

   Z1(P)=z(index+big);   %--big particle Z coordination

   Y1(P)=y(index+big);   %--big particle Y coordination

   axis off

  end

for i=1:nu
      xx(i)=x((framen-1)*nu+i);
      yy(i)=y((framen-1)*nu+i);
      zz(i)=z((framen-1)*nu+i);
end
```

```
plot(yy,zz,'bO');hold on;
plot(Y1,Z1,'r');
axis ([0 16 0 24] );
axis on;
```

A.8 3D Animation of the Intruder Particle

```
%-------------------------------------------------------------------------
%------animation code to see the motion of the intruder paticle in
%------modified couette flow field with gravity and boundary at z=zero
%-------------------------------------------------------------------------
clear;
load /afs/cad/research/a/2/run/test2/zposition;       %load file
PP=zposition;
framen=1000;              %--frames number
nu=1768;                  %--Total particles number
big=1;                    %--index of the big particles number
No=PP(:,1);x=PP(:,2);y = PP(:,3); z = PP(:,4);        %z-x coordination

M=moviein(framen);
for P = 1:framen,
      %P=framen;
   index=(P-1)*nu;
   index1=P*nu;
   XX=x(index+big);
   YY=y(index+big);     %--big particle Y coordination
   ZZ=z(index+big);     %--big particle Z coordination

   XX1(P)=XX;
   YY1(P)=YY;           %--big particle Y coordination
   ZZ1(P)=-2;
   XX1(P+1)=x(index1+big);
   YY1(P+1)=y(index1+big);
   ZZ1(P+1)=-2;

   XX2(P)=16;
   YY2(P)=YY;           %--big particle Y coordination
   ZZ2(P)=ZZ;
   XX2(P+1)=16;
```

```
    YY2(P+1)=y(index1+big);
    ZZ2(P+1)=z(index1+big);

    XX3(P)=XX;
    YY3(P)=16;            %--big particle Y coordination
    ZZ3(P)=ZZ;
    XX3(P+1)=x(index1+big);
    YY3(P+1)=16;
    ZZ3(P+1)=z(index1+big);

    %--------draw the sphere--------
    view(-90,30);
    n=64;
    plot3(XX1,YY1,ZZ1,'r.');hold on;
    plot3(XX2,YY2,ZZ2,'r.');hold on;
    plot3(XX3,YY3,ZZ3,'r.');hold on;
    [xx,yy,zz]=sphere(n);
    shading interp;
    colormap(gray);
    axis([-2 16 -2 16 -2 16]);

    mesh(xx+XX,yy+YY,zz+ZZ);hold off;

    xlabel('X');
    ylabel('Y');
    zlabel('Z');
    grid on;
   M(:,P)=getframe;
   end
movie(M,1,20);
```

A.9 Contact Angle and Force

```
%-------------------------------------------------------------------------
%-------File name:    ffxy.m
%-------Author:              Jian Liu
%-------Advisor:             Dr. Anthony Rosato
%-------usage:        accumulate the collision force in x & y direction
%-------              for each contact around the intruder,
```

```
%-------              get the force distribution in upper and lower
%-------              surface of the intruder
%-------input file:   zposition has 4 colomns,t,x,y,z
%-------output file:    1. phi/dist
%                      2. theta/dist
%                      3. hist(phi)
%                      4. hist(theta)
%                      5. n-collision
%                      6. Tupper/Tlower
%-----------------------------------------------------------------------

%------------initialization of code-----------------------------------
clear;
H=16;                  %---height of the simulation cell
Zone=10;               %---zone number of the gap height
np=484;                %---Total number of the particles
startmm=1;             %--start time step 0.05s each
endmm=2000;            %---end time step
Rlarge=3.0;            %--the Ridus ratio of the large particle
Rsmall=1.0;            %--the Ridus ratio of the small particle
search=Rlarge+Rsmall;
Rlimit=sqrt((Rlarge+Rsmall)^2-2*Rsmall^2);
PI=3.1416;

for i=1:10             %--initialization of contact No. in high/lower
section.high(0--180),lower(180-360)
   Tupper(i)=0;
   Tlower(i)=0;
   p(i)=0;
   Tangle(i,1:4)=0;
   Displace(i,1:4)=0;
end
k=0;

%-------load input data from zposition -----------------------
load /afs/cad/research/a/2/data/exp18B/04/zposition;
%--each line has t, x, y, z-----four columns
for m=startmm:endmm
```

```
   Displace=zposition((m-1)*np+1:m*np,:);
   t=Displace(:,1);
   x=Displace(:,2);
   y=Displace(:,3);
   z=Displace(:,4);

   sum=0;
%-----------initial No. for n-collision=0 at the beginning of each time
%--------Sorting section-------------------
   for i=2:np
      dx=abs(x(i)-x(1));
      dy=abs(y(i)-y(1));
      dz=abs(z(i)-z(1));
      dist=sqrt(dx^2+dy^2+dz^2);

      x1=x(i)-x(1);
      y1=y(i)-y(1);
      z1=z(i)-z(1);

      if (dist<=search)
         sum=sum+1;
         zoneNo=ceil(Zone*(y(1)-Rlimit)/(H-2*Rlimit));
%------find the zone No. of this collision
%------cell(10*0.09)=1 is zone1, cell(10*0.99)=10 is zone10
%------------sorting algorithm for phi----------------------
         if z1>=0                          %----the upper half
            phi=180/PI*atan(sqrt(dx^2+dy^2)/dz);
         else                              %----the lower half
                  phi=180/PI*(3.14-atan(sqrt(dx^2+dy^2)/dz));
         end

%------------sorting algorithm for theta--------------------
         if (y1==0)                %------------on the x-axis
            if (x1>=0)
               Theta=0;
            else
               Theta=PI;
            end
```

```
        end

        if (x1==0)                    %-----------on the y-axis
           if (y1>=0)
              Theta=PI/2;
           else
              Theta=3*PI/2;
           end
        end
%-----------not on the axis---------------------------------
        if (x1>0) & (y1>0)
    %----No.1 phase
              theta=180/PI*atan(abs(dy/dx));
        else if (x1>0) & (y1<0)
    %----No.2 phase
                 theta=180/PI*(2*PI-atan(abs(dy/dx)));
             else if (x1<0) & (y1>0)
    %----No.3 phase
                    theta=180/PI*(PI-atan(abs(dy/dx)));
                  else
    %----No.4 phase
                    theta=180/PI*(PI+atan(abs(dy/dx)));
                  end
             end
        end

        k=k+1;
        Tangle(k,1)=dist;
        Tangle(k,2)=phi;
        Tangle(k,3)=theta;
        Tangle(k,4)=zoneNo;
%------save theta in each y zone of intruder particle-------------

    if (theta<180)                    %----belong to Tupper(zone)
                Tupper(zoneNo)=Tupper(zoneNo)+1;
    else                              %----belong to Tlower(zone)
                Tlower(zoneNo)=Tlower(zoneNo)+1;
    end
```

```
    end
  end

  if ((sum>0)&(sum<=12))
     p(sum)=p(sum)+1;       %----n-collsion in n zone
  end
end


%--------plot section----- ------------------------------------
for i=1:15
   pp(i)=180*i/15;
end

for i=1:30
   ppp(i)=360*i/30;
end

for i=1:10
   mm(i)=i;
end

%--------plot dist & phi-------------------
subplot(3,2,1);
plot(Tangle(:,2),Tangle(:,1),'.');
lo=search-0.02;
hi=search+0.02;
%axis([0 180 lo hi]);
hold on;
xlabel('phi');
ylabel('dist');

%--------plot dist & theta-------------------
subplot(3,2,2);
plot(Tangle(:,3),Tangle(:,1),'.');
lo=search-0.02;
hi=search+0.02;
%axis([0 360 lo hi]);
```

```
hold on;
xlabel('theta');
ylabel('dist');

%--------contact No. histogram of phi from 0-180-------------------
subplot(3,2,3);
T1=hist(Tangle(:,2),15)/length(Tangle);
plot(pp,T1,'bo');hold on;
plot(pp,T1,'r');hold on;
axis([0 180 0 1]);
%hist(Tangle(:,2),15);
xlabel('bins');
ylabel('frequency of phi');

%--------contact No. histogram of theta from 0-360------------------
subplot(3,2,4);
T2=hist(Tangle(:,3),30)/length(Tangle);
plot(ppp,T2,'bo');hold on;
plot(ppp,T2,'r');hold on;
axis([0 360 0 1]);
%-----------the above equal to hist(Tangle(:,3),30);---------------
xlabel('bins');
ylabel('frequency of theta');

%--------plot over all n-collision No.-----------------------------
subplot(3,2,5);
kk=0;
for i=1:10
   kk=kk+p(i);
end
plot(mm,p/kk,'r');hold on;
plot(mm,p/kk,'bo');
axis([0 10 0 1]);
xlabel('n-collision');
ylabel('contact frequency');

%--------plot distribution function T1/T2-----------------------
subplot(3,2,6);
```

```
plot(Tupper/length(Tangle),mm/10,'ro');hold on;
plot(Tupper/length(Tangle),mm/10,'r');hold on;
plot(Tlower/length(Tangle),mm/10,'bo');hold on;
plot(Tlower/length(Tangle),mm/10,'b');
xlabel('contact distribution (r-upper/b-lower)');
ylabel('Normalized gap height');
axis([0 1 0 1]);
```

APPENDIX B

ZONING INDEX SEARCH METHOD

The following flow chart described the searching algorithm for the closest neighbors around the tracer particle.

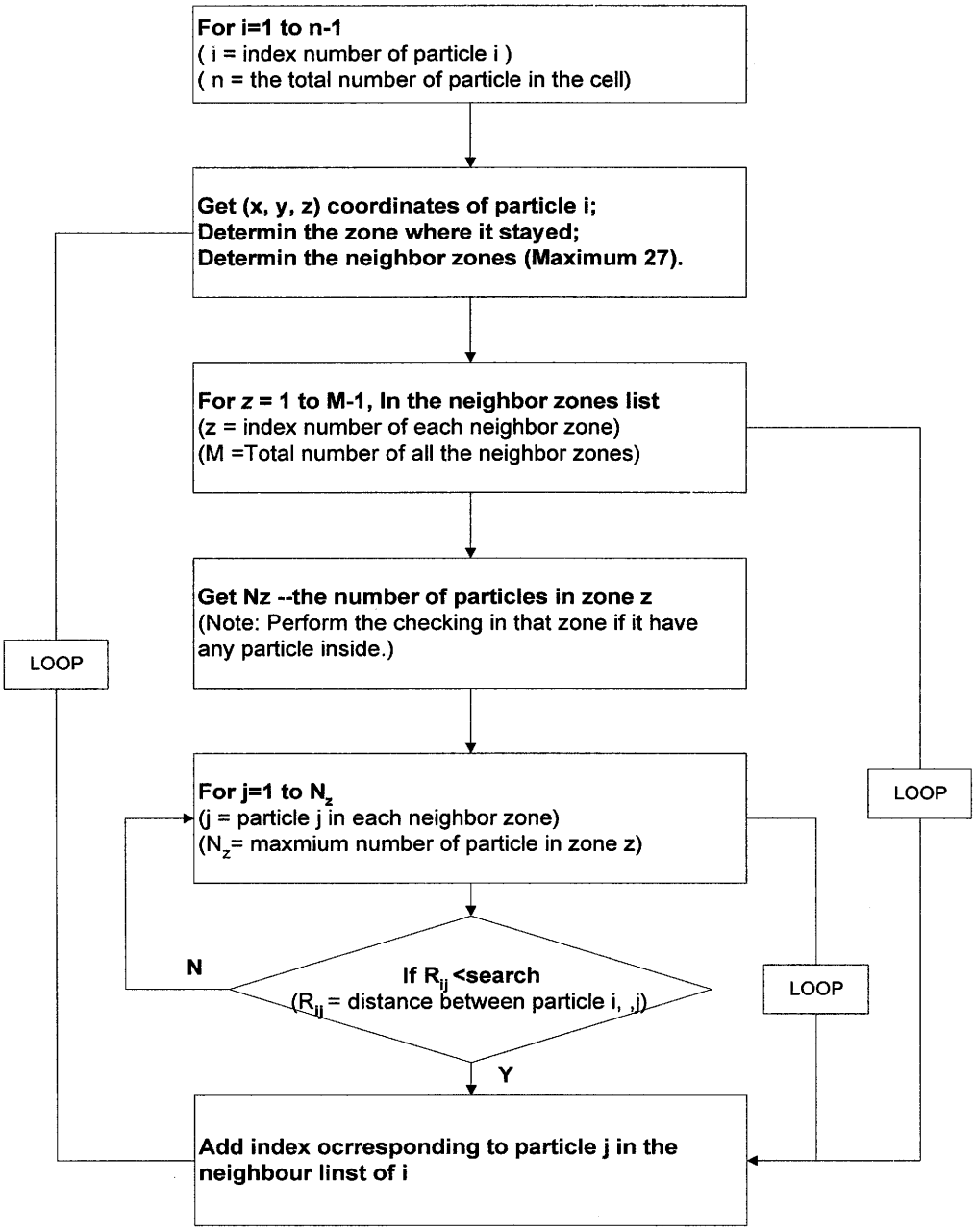

Figure B.1 Flow chart of the zoning index search method.

REFERENCES

1. R. A. Bagnold, "Experiments on a gravity-free dispersion of large solid spheres in a Newtonian fluid under shear," Proc. Roy. Soc. London **A 225**, 49 (1954).

2. S. B. Savage and M. Sayed, "Stresses developed by dry cohesionless granular materials sheared in an annular shear cell"," J. Fluid Mech. **142** (8), 391 (1984).

3. S. B. Savage and C. K. K. Lun, "Particle size segregation in inclined chute flow of dry cohesionless granular solids," J. Fluid Mech. **189**, 311-335 (1988).

4. D. M. Hanes and D. L. Inman, "Observations of rapidly flowing granular-fluid materials," J. Fluid Mech. **150** (6), 357 (1985).

5. D. M. Hanes, J. T. Jenkins, and M. W. Richman, "The thickness of steady plane shear flows of circular disks driven by identical boundaries," Journal of Applied Mechanics **110**, 969-974 (1988).

6. K. Craig, R. H. Buckholz, and G. Domoto, "An experimental study of the rapid flow of dry cohesionless metal powders," Trans. ASME J. Appl. Mech. **53** (7), 935 (1986).

7. K. Craig, R. H. Buckholz, and G. Domoto, "Effect of shear surface boundaries on stress for shearing flow of dry metal powders-An experimental study," Trans. ASME J. Tribol. **109** (8), 232 (1987).

8. J. T. Jenkins and S. B. Savage, "A theory for the rapid flow of identical, smooth, nearly elastic spherical particles," Journal of Fluid Mechanics **187** (130), 187-202 (1983).

9. M. W. Richman and C. S. Chou, "Boundary effects on granular shear flows of smooth disks," Math. Phys. **39**, 885 (1988).

10. M. W. Richman and R. E. Martin, "Unconfined granular materials thermalized by fluctuating horizontal surfaces," presented at the Proceedings of the 9th Conference on Engineering Mechanics, 1992 (unpublished).

11. C. S. Campbell and C. E. Brennen, "Computer simulation of granular shear flows," Journal of Fluid Mechanics **151**, 168-188 (1985).

12. C. S. Campbell, "Boundary interactions for two-dimensional granular flows. Part1. Flat boundaries, asymmetric stresses and couple stresses," J. Fluid Mech. **247**, 111-136 (1993).

13. M. Y. Louge, J. T. Jenkins, and M. A. Hopkins, "Computer simulations of rapid granular shear flows between parallel bumpy boundaries," Physics of Fluids A **2** (6), 1042-1044 (1990).

14. A. D. Rosato and H. J. Kim, "Particle dynamics calculations of wall stresses and slip velocities for granular Couette flow of smooth inelastic spheres," Continuum Mechanics and Thermodynamics **6** (1), 1-20 (1994).

15. O. R. Walton and R. L. Braun, "Stress calculations for assemblies of inelastic spheres in uniform shear," Acta Mechanica **63**, 73 (1986).

16. O. R. Walton and R. L. Braun, "Viscosity and temperature calculations for assemblies of inelastic, frictional disks," Journal of Rheology **30** (5), 949-980 (1986).

17. S. Ogawa, "Multitemperature theory of granular materials," presented at the U.S.-Japan Seminar on Continuum Mechanical and Statistical Approaches in the Mechanics of Granular Materials, Sendai, Japan, 1978 (unpublished).

18. S. B. Savage and D. J. Jeffrey, "The Stress Tensor in a Granular Flow at High Shear Rates.","," J. Fluid Mech. **110**, 255-272 (1981).

19. H. H. Shen and N. L. Ackermann, "Constitutive Relationship for Fluid-Solid Mixtures," J. Eng. Mech. Div. ASCE **108**, 748-768 (1982).

20. C. K. K. Lun, S. B. Savage, D. J. Jeffrey *et al.*, "Kinetic theories for granular flow: inelastic particles in Couette flow and slightly inelastic particles in a general flow field," Journal of Fluid Mechanics **140**, 223 (1984).

21. J. C. Williams, "The segregation of powders and granular materials," Fuel Soc. J. **14**, 29-34 (1963).

22. J. C. Williams, "The segregation of granules in vibrated beds," Powder Technology **1**, 134 (1967).

23. K. Ahmad and I. J. Smalley, "Observation of particle segregation in vibrated granular systems," Powder Technology **8**, 69-75 (1973).

24. C. F. Harwood, "Powder segregation due to vibration," Powder Technology **16**, 51-57 (1977).

25. T. Shinbrot and F. Muzzio, "Reverse buoyancy in shaken granular beds," Physical Review Letters **81** (20), 4365-4368 (1998).

26. A. P. J. Brew, H.-M. Ensner, C. A. Druelle *et al.*, "Reversing the Brazil-Nut Effect: Competition between Percolation and Condensation," Physical Review Letters **90** (1), 014302-1 (2003).

27. J. A. Drahun and J. Bridgewater, "The mechanism of free surface segregation," Powder Technology **36**, 39-53 (1983).

28. W. S. Foo and J. Bridgwater, "Particle migration," Powder Technology **36**, 271-273 (1983).

29. J. Bridgwater, W. S. Foo, and D. J. Stephens, "Particle mixing and segregation in failure zones: theory and experiment," Powder Technology **41**, 147-158 (1985).

30. D. J. Stephens and J. Bridgwater, "The mixing and segregation of cohesionless particulate materials. Part II. Microscopic mechanisms for particles differing in size," Powder Technology **21**, 29-44 (1978).

31. T. Takahashi, "Debris flow on prismatic channel," Journal of the Hydraulics division, ASCE **106**, 381-395 (1980).

32. T. R. H. Davies, "Debris flow surges - a laboratory investigation," Mitteilung No. 96 der Versuchsanstalk fur Wasserbau, Hydrologie, und Glaziology an des ETH **1-122** (1988).

33. R. Khosropour, J. Zirinsky, H. K. Pak *et al.*, "Convection and size segregation in Couette flow of granular material," Physical Review E **56** (4), 4467-4473 (1997).

34. J. T. Jenkins and M. W. Richman, "Boundary conditions for plane flows of smooth, nearly elastic, circular disks," J. Fluid Mech. **171**, 53 (1986).

35. J. T. Jenkins and F. Mancini, "Kinetic theory for binary mixtures of smooth, nearly elastic spheres," Phys. Fluids A **1** (12), 2050-2057 (1989).

36. M. Farrell, C. K. K. Lun, and S. B. Savage, "A Simple Kinetic Theory for Granular Flow of Binary Mixtures of Smooth, Inelastic, Spherical Particles," Acta Mechanica **63**, 45-60 (1986).

37. J. T. Willits and B. O. Arnarson, "Kinetic theory of a binary mixture of nearly elastic disks," Phy. of Fluids **11** (10), 3116-3122 (1999).

38. H. Van Beijeren and M. H. Ernst, ""The modified Enskog equation"," Physica (Amsterdam) **68**, 437 (1973).

39. C. K. K. Lun, "Granular dynamics of inelastic spheres in Couette flow," Phys. Fluids **8** (11), 2868-2883 (1996).

40. A. Karion and M. L. Hunt, "Wall stresses in granular couette flow of mono-sized particles and binary mixtures," Powder Technology **109**, 145-163 (2000).

41. C. Campbell and Y. Zhang, ""The interface between fluid like and solid like behavior in granular flows," Advances in Micromechanics of Granular materials. (1993) , 261-273 (1993).

42. A. D. Rosato, F. B. Prinz, K. J. Strandburg *et al.*, "Monte Carlo simulation of particulate matter segregation," Powder Technology **49**, 59-69 (1986).

43. A. D. Rosato, K. J. Strandburg, F. P. Prinz *et al.*, "Why the Brazil nuts are on top: size segregation of particulate matter by shaking," Physical Review Letters **58**, 1038-1041 (1997).

44. Y. Lan and A. D. Rosato, "Convection related phenomena in vibrated granular beds," Physics of Fluids **9** (12), 3615-3624 (1997).

45. T. Poschel and H. J. Herrmann, "Size segregation and convection," Europhysics Letters **29** (2), 123-128 (1995).

46. T. G. Drake and O. R. Walton, "Comparison of experimental and simulated grain flows," J. Appl. Mech. **62**, 131 (1995).

47. D. Hirshfeld and D. C. Rapaport, "Molecular dynamics studies of grain segregation in sheared flow," Physical review E **E** (2), 2012-2018 (1997).

48. J. Baxter, U. Tuzun, J. Burnell *et al.*, "Granular dynamics simulations of two dimensional heap formation," Phys. Rev. E **55**, 3546-3554 (1997).

49. J. Baxter, U. Tuzun, D. M. Heyes *et al.*, "Stratification in poured granular heaps," Nature **391**, 136 (1998).

50. Y. Taguchi, "New origin of convective motion: elastically induced convection in granular materials," Physical Review Letters **69**, 1367-1370 (1992).

51. B. N. Asmar, P. A. langston, A. J. matchett *et al.*, "Validation tests on a distinct element model of vibrating cohesive particle systems," Computers and Chemical Engineering **26**, 785-802 (2002).

52. J. Liu and A. Rosato, "Dynamic behavior of an intruder in a granular couette flow," Proceeding of 2002 Material Research Society Fall Meeting, Boston, MA. (2002).

53. M. Y. Louge, J. T. Jenkins, A. Reeves *et al.*, "Microgravity Segregation in Collisional Granular Shearing Flows," IUTAM Symposium "Segregation in Granular Flows", June, 1999, Cape May, NJ. (1999).

54. P. A. Cundall, Report AD/A - 001 602, U.S. Nat. Tech. Information Service, Springfield, VA. (1974).

55. D. Deserable and J. Martinez, "Using a cellular automaton for the simulation of flow of granular," Powders and Grains **93**, 345 (1993).

56. D. Bideau and A. Hansen, Disorder and granular media. North-Holland, Netherlands: Elsevier. (1993).

57. P. A. Langston, U. Tuzun, and D. M. Heyes, "Continuous potential discrete particle simulations of stress and velocity fields in hoppers: transition from fluid to granular flow.," Chemical Engineering Science **49**, 1259 (1994).

58. P. A. Langston, U. Tuzun, and D. M. Heyes, "Discrete element simulation of granular flow in 2D and 3D hoppers: dependence of discharge rate and wall stress on particle interactions," Chemical Engineering Science **50**, 967 (1995).

59. P. A. Langston, U. Tuzun, and D. M. Heyes, "Discrete element simulation of internal stress and flow fields in funnel flow hoppers," Powder Technology **85**, 153 (1995).

60. P. A. Langston, U. Tuzun, and D. M. Heyes, "Distinct element simulation of interstitial air effects in axially symmetric granular flows in hoppers," Chemical Engineering Science **51**, 873 (1996).

61. W. T. Ashurst and W. G. Hoover, "Argon shear viscosity via a Lennard-Jones potential with equilibrium and nonequilibrium molecular dynamics," Physical Review Letters **31**, 206-209 (1973).

62. O. R. Walton, "Numerical simulation of inelastic, frictional particle-particle interactions," in *Particulate Two-Phase Flow*, edited by M. C. Roco (Butterworths, Boston, 1992), pp. 884-911.

63. R. D. Mindlin and H. Deresiewicz, "Elastic spheres in contact under varying oblique forces," J. Appl. Mech. **20**, 327 (1953).

64. O. R. Walton, "Numerical simulation of inclined chute flows of monodisperse, inelastic, frictional spheres," presented at the Second U.S.-Japan Seminar on Micromechanics of Granular Materials, Potsdam, NY, 1991 (unpublished).

65. S. Mallat, "A theory for multiresolution signal decomposition: the wavelet representation," IEEE Pattern Anal. and Machine Intel. **11** (7), 674-693 (1989).

66. S. B. Savage and R. Dai, "Some aspects of bounded and unbounded shear flows of granular material," presented at the Advances in Micromechanics of Granular Materials, Potsdam, NY, 1991 (unpublished).

67. J. McElwaine and K. Nishimura, "Size segregation in snow avalanches: observations and experiments," presented at the IUTAM Symposium on Segregation in Granular Flows, Cape May, NJ, 2000 (unpublished).

68. S. B. Savage and K. Hutter, "The dynamics of avalanches of granular materials from initiation to run out. Part 1: theory," Acta Mech. **100**, 37 (1991).

69. S. B. Savage, "Numerical simulations of Couette flow of granular materials: spatio-temporal coherence and 1/f noise," in *Physics of Granular Media*, edited by J. Dodds and D. Bideau (Nova Scientific Publishers, New York, 1991), pp. 343-362.

70. D. J. Stephens and J. Bridgewater, "The mixing and segregation of cohesionless particulate materials. Part I. Failure zone formation," Powder Technology **21**, 17-28 (1978).

71. D. C. Hong and P. V. Quinn, "Reverse Brail Nut Problem: Competition between Percolation and Condensation," Physical Review Letters **86** (15), 3423-3426 (2001).

72. T. Shinbrot and F. J. Muzzio, "Reverse Buoyancy in Shaken Granular Beds," Physical Review Letters **81** (20), 4365-4368 (1998).

73. J. T. Jenkins and D. K. Yoon, "Segregation in Binary Mixtures under Gravity," Physical Review Letters **88** (19), 194301(1)-194301(3) (2002).